Title
Investigation of Alternative Fuels and Advanced Engine Technology: Improving Engine Efficiency and Reducing Emissions

Author
Rapp, Vi Hai

Publication Date
2011

Peer reviewed|Thesis/dissertation

Investigation of Alternative Fuels and Advanced Engine Technology: Improving Engine Efficiency and Reducing Emissions

By

Vi Hai Rapp

A dissertation submitted in partial satisfaction of the

requirements for the degree of

Doctor of Philosophy

in

Engineering – Mechanical Engineering

in the

Graduate Division

of the

University of California, Berkeley

Committee in charge:

Professor Robert W. Dibble, Chair
Professor Jyh-Yuan Chen
Professor Daniel M. Neumark

Fall 2011

Investigation of Alternative Fuels and Advanced Engine Technology:
Improving Engine Efficiency and Reducing Emissions

by

Vi Hai Rapp

Abstract

Investigation of Alternative Fuels and Advanced Engine Technology:

Improving Engine Efficiency and Reducing Emissions

by

Vi Hai Rapp

Doctor of Philosophy in Engineering – Mechanical Engineering

University of California, Berkeley

Professor Robert W. Dibble, Chair

The internal combustion engine has vastly improved over the past 100 years. With global warming and pollution being a rising concern, engineers are working towards improving efficiency and emissions of engines. The spark-ignited engine (or gasoline engine) offers improvement in emissions with a sacrifice in thermal efficiency. The compression ignition engine (Diesel engine) increases the thermal efficiency, due to operation at higher compression ratios, but emits high amounts of particulate matter and oxides of nitrogen (NO_x). Although improvements in fuel refinement have decreased the amount of engine pollutants, the output of pollutants for both spark-ignited and Diesel engines is still too great.

This dissertation explores two advanced engine concepts with alternative fuels for improving thermal efficiency and reducing emissions in automobiles. The first concept investigated is a spark-ignited internal combustion engine operating using hydrogen, oxygen, and argon. Basic engine theory predicts such an engine will see a considerable improvement in engine efficiency (theoretically ≈75%, and in practice ≈50% including heat transfer and friction losses) over standard engines. These gains in thermal efficiency are due to argon's monatomic structure, which yields a high specific heat ratio ($\gamma = 1.67$ compared to $\gamma < 1.4$ for air). The water produced by the combustion of hydrogen can be extracted in the exhaust by a condenser, allowing the recycling of nearly pure argon in a closed loop system. Therefore, argon re-fueling is not required.

Achieving efficiencies above 50% with a hydrogen-oxygen-argon engine, however, is difficult due to engine knock limiting spark advance. In an effort to obtain the highest efficiency of this engine concept, experiments were conducted using single and dual spark-ignition for high argon concentrations. Results showed dual spark-ignition slightly increased indicated thermal efficiency, but was still limited by engine-knock. A three-zone model showed that

argon as a working fluid increases in-cylinder temperatures, unburned gas temperatures, and laminar flame speed. The model suggests that specific heat ratio affects end gas temperatures more than increasing flame speed.

The second engine concept investigates variables and fuel trends for predicting ignition in homogenous charge compression ignition (HCCI) engines. Octane number, a metric for fuel performance in gasoline engines, and cetane number, a metric for fuel performance in Diesel engines, do not accurately predict fuel performance in HCCI engines. To develop a metric for predicting fuel performance in HCCI engines, correlations between ignition of fuels in an HCCI engine and varying engine parameters are investigated. A relationship between fuel chemistry and ignition in HCCI engines is also explored. Results show that previous methods for predicting ignition do not correlate well with experimental data and auto-ignition is highly sensitive to fuel chemistry.

A single-zone well-mixed-reactor model is used to investigate three different mechanisms for predicting auto-ignition in the HCCI engine. All three mechanisms accurately predicted the auto-ignition order of fuels containing isooctane and n-heptane, but did not predict auto-ignition of blends containing toluene and ethanol. Blends of toluene and n-heptane were further investigated using the model to identify potential problems with the toluene mechanisms. The model results showed increasing the amount of toluene linearly by volume did not result in a linear advance in auto-ignition.

Dedicated to my family and friends.
I would not have finished this dissertation without their love and support.

Table of Contents

List of Figures

List of Tables

Acknowledgements

This dissertation would not have been possible without the support and assistance of several people. First, I would like to thank my research advisor, Professor Robert W. Dibble for helping me improve both my writing and presentation skills. Next, I want to thank Professor Chen for his assistance with modeling my experiments and editing my research papers. Also, thank you for helping me gain a better understanding of combustion modeling by letting me attend your group meetings. Many thanks to Professor Carlos Fernandez-Pello for his sound advice and words of wisdom. I would not have found the my post-doctoral position without his encouragement. Thanks also to Professor Daniel Neumark for teaching me the importance of chemical kinetics and showing me that Fenimore's mechanism for prompt NO_x is spin forbidden.

I am forever indebted to Bill Cannella for reviewing my results each month, reviewing my research papers, and assisting me in completing my HCCI research. Many thanks to Nick Killingsworth and Dan Flowers for their support with the hydrogen-oxygen-argon engine research and for their support with all my research at UC Berkeley. I would also like to thank everyone in the combustion analysis laboratory for their help and support, especially Tyler Dillstrom, Andrew Van Blarigan, Andrew North, Katee Lask, Samveg Saxena, Martin Wissink, Hunter Mack, Greg Bogin, Wolfgang Hable, Phil Tschann, and Malte Broeckelmann.

I am eternally grateful to the staff in Hesse Hall, including Scott McCormick, Mike Neufer, Alex Jordan, and Pete Graham, for assisting me with my research and helping me keep the CFR running. I owe my deepest gratitude to Maryanne Peters for making sure I always had enough money to eat and for providing encouragement and support when I needed it most.

Thanks to Lawrence Livermore National Laboratory for their support in the Hydrogen research, the Department of Energy for funding the hydrogen-oxygen-argon engine research, and Chevron for their support in supplying fuel and the means to conduct the HCCI research.

Lastly, I would like to thank my family and friends. Thanks to my father and mother for all their love and support. Thank you also for encouraging me to continue my education and bringing me food when I needed it the most. Thanks to Alex for proof reading all of my work and putting up with my mood swings. Thanks to my brother, Ryan, for reminding me to "just dance" and to my Grandma for always believing in me. Many thanks to Jennifer Jacobsen for always reminding me I was on the right path and for listening when I needed to "geek-out." Thanks also to Asha Atwell for plucking me out of Utah and keeping me sane

these past five years. I am eternally grateful for all of your love, support, and assistance.

Curriculum Vitae

Vi Hai Rapp

Expertise

Combustion; Thermodynamics; Chemical Kinetics; Heat Transfer; Finite Element Analysis

Education

Ph.D. University of California-Berkeley, Mechanical Engineering December 2011
GPA 3.81
Major: Combustion Minors: Chemistry and Heat Transfer
Dissertation: Investigation of Alternative Fuels and Advanced Engine Technology: Improving Engine Efficiency and Reducing Emissions

M.S. University of Utah, Mechanical Engineering August 2005
GPA 3.94
Concentrations: Heat Transfer and Aerospace Propulsion
Thesis: Reinstrumentation and Validation of a Supersonic Wind Tunnel

B.S. University of Utah, Mechanical Engineering December 2003
GPA 3.88
Graduated Cum Laude

Research and Industry Experience

University of California-Berkeley, Berkeley, CA 2007-Present
Graduate Student Researcher

MOOG Aircraft Group, Salt Lake City, UT 2005-2007
Thermal and Stress Analysis Engineer

University of Utah, Salt Lake City, UT 2001-2005
Research Assistant

Teaching Experience

Dominican University of California, San Rafael, CA
General Physics Laboratory
Instructor
Fall 2011

Conceptual Physics Laboratory
Instructor
Fall 2011

University of California, Berkeley, Berkeley, CA

GSI Teaching and Resource Center
Discipline Cluster Workshop Leader
August 2010 and January 2011

Thermodynamics
Graduate Student Instructor
Spring 2010 (Professor: Van Carey)
Spring 2011 (Professor: Jyh-Yuan Chen)
Fall 2011 (Professor: Van Carey)

Mechanical Engineering Laboratory
Graduate Student Instructor
Spring 2008 (Professor: Jyh-Yuan Chen)
Fall 2008 (Professor: Robert Dibble)
Fall 2009 (Professor: Tony M. Keaveny)

Santa Clara University, Santa Clara, CA

Vehicle Technology
Guest Lecturer
January 2010

University of Utah, Salt Lake City, UT

Fluid Mechanics
Teaching Assistant
Spring 2004 (Professor: Joseph Klewicki)

Aerodynamics
Teaching Assistant
Spring 2004 (Professor: Patrick McMurtry)

Heat Transfer
Teaching Assistant
Fall 2004 (Professor: Kuan Chen)

Publications

Rapp, V.H., Cannella, W., Dillstrom, V.T., Chen, J.-Y., and Dibble, R.W., "Effects of Fuel Properties on Autoignition in HCCI Engines," Western States Section of the Combustion Institute, October 2011.

Chin, G.T., Chen, J.-Y., Rapp, V.H., and Dibble, R.W., "A Reduced DME Chemistry for a Wide Range of Combustion: Opposed-Jet Flames, Premixed flames, and HCCI," Journal of Combustion, 2011

DeFilippo, A., Saxena, S., Rapp, V.H., Dibble, R.W., Chen, J-Y, Ikeda, Y., and Nishiyama A., "Extending the lean operation limits of a gasoline engine using a microwave-assisted sparkplug,"SAE 2011-01-0820

Killingsworth, N.J., Rapp, V.H., Flowers, D.L., Aceves, S.M., Chen, J.-Y., and Dibble, R.W., "Increased Efficiency in SI Engine with Air Replaced by Oxygen in Argon Mixture,"Proceedings of the Combustion Institute, In Press, Corrected Proof, Available online 20 September 2010, ISSN 1540-7489, DOI: 10.1016/j.proci.2010.07.035

Saxena, S., Rapp, V.H., Chen, J-Y., and Dibble, R.W., "A Numerical Study of Ultra-high Efficiency Combustion of a Hydrogen-Oxygen-Argon Mixture in HCCI engines,"Western States Section of the Combustion Institute, March 2009

Killingsworth, N.J., Rapp, V.H., Flowers, D.L., Aceves, S.M., Chen, J.-Y., and Dibble, R.W., "Characteristics of Knock in Hydrogen-Oxygen-Argon SI engine, Western States Section of the Combustion Institute, March 2009

Rapp, V.H., Killingsworth, N.J., Aceves, S.A., Chen, J.-Y., and Dibble, R.W., "Investigation of a High Efficiency, Zero Emissions H2-O2-Ar Internal Combustion Engine, Proceedings of the Australian Combustion Symposium, December 2009

Rapp,V.H., Killingsworth, N.J., Aceves, S.A., Chen, J.-Y., and Dibble, R.W., "Investigation of Knock Prevention in High Efficiency, Zero Emissions H2-O2-Ar Internal Combustion, Western States Section of the Combustion Institute, November 2009

Rapp, V.H., Roemer, R., A Thermodynamic-Physiological Description of the Allometric Relationship between Resting Metabolism and Body Mass, Proceedings of the National Conference on Undergraduate Research (NCUR), March 13-15, 2003

Rapp, V.H., Jacobsen, J., Lawson, M., Parker, A., and Chen, K., "Design, Construction and Testing of a Desktop Supersonic Wind Tunnel," American Journal of Undergraduate Research, 4, No. 2, 2005

Publications in Review

Rapp, V.H., DeFilippo, A., Saxena, S., Chen, J.-Y., Dibble, R.W., Nishiyama A., Moon, A., and Ikeda, Y., "Extending lean operating limit of engines burning methane using a microwave-assisted spark plug ," Biomass & Bioenergy submitted July 2011.

Presentations

Presented paper titled "Effects of Fuel Properties on Autoignition in HCCI Engines" at the WSS/CI Fall meeting in Riverside, California (2011).

Presented paper Modeling of emissions from HCCI Engines using a Consistent 3-Zone Model with Applications to Validation of Reduced Chemistry, by G. Chin and J.-Y. Chen at the 33rd International Combustion Symposium in Beijing, China (August 2010).

Presented research on high efficiency H2-O2-Ar internal combustion engine at the Australia Combustion Symposium in Brisbane, Australia (December 2009).

Presented research on high efficiency H2-O2-Ar internal combustion engine at the WSS/CI Fall meeting in Irvine, California (2009).

Presented thermal and stress results to various customers while working for MOOG Aircraft Group (2006).

Presented senior design project at an American Institute of Aeronautics and Astronautics (AIAA) student conference at UCLA (2004).

Presented undergraduate research on the allometric relationship between resting metabolism and body mass of animals at the National Conference of Undergraduate Research (NCUR) (2003) and presented the same research at a Utah Government Research Awareness Program to encourage the senator of Utah to invest more tax money into graduate research (2001).

Grants, Fellowships, and Scholarships

Block Grant Fellowship	Summer 2011
Anselmo John Macchi Fellowship Fund in Engineering	Summer 2009
Chevron Fellowship	2007-2008
Campbell Fellowship	2004-2005
American Society of Mechanical Engineers Scholarship	2003
Society of Women Engineers Scholarship	2003
Arel Barrier Scholarship	2002
C.M. Collins Scholarship	2001

Honors and Awards

Acceptance to the Summer Institute for Preparing Future Faculty	Summer 2011
Acceptance to the Princeton-CEFRC Summer Program on Combustion	Summer 2010

Outstanding Graduate Student Instructor Award, UC Berkeley, Department of Mechanical Engineering 2009-2010

Community Service

Students for Environmental Energy Development (SEED) Aug. 2010 – Dec. 2010
Volunteer Teacher for 4th and 5th grade

Cal Cycling (UC Berkeley Cycling Team) 2009-2011
Sponsorships Chair and Womens Mountain Team Captain

Skills and Qualifications

Programming Languages: C, Matlab, Mathcad, Maple, Tcl, HTML

Computational Tools: ANSYS, Fluent, Cantera, LabView, Pro/ENGINEER, Solid Works, Unigraphics, Sinda/G, LaTex, Microsoft Office

Operating Systems: Windows, Mac OS X, Red Hat Linux

Technical Skills: Proficient using a manual lathe and milling machine and operating internal combustion engines.

Languages: Japanese at an intermediate level

Affiliations/Memberships

Tau Beta Pi Honorary Society

Pi Tau Sigma Honorary Society

American Society of Mechanical Engineers

Society of Women Engineers

Society of Automotive Engineers

Chapter 1

Introduction

Increasing concern with global warming, pollution, and oil prices have pushed development of alternative fuels and advanced engine technology that improve efficiency and reduce emissions. For example, development and advancement of electric, hybrid, and alternative fuel vehicles are entering the market, competing with petroleum burning vehicles. This dissertation specifically investigates two advanced engine, alternative fuel concepts: a hydrogen-oxygen-argon (H_2-O_2-Ar) internal combustion (IC) engine and a homogenous charge compression ignition (HCCI) engine.

1.1 Background and Related Work

1.1.1 Hydrogen Internal Combustion Engines

In 1807, Swiss inventor Franois Isaac de Rivaz invented the first internal combustion engine and operated it using a mixture of hydrogen and oxygen [Guarnieri, 2011]. Over a century later, the first advancements for using hydrogen as a transportation fuel were made when Rudolf Erren filed the first patent for internal combustion engines using hydrogen as a fuel [Erren, 1939].

At the time of this dissertation, hydrogen has re-emerged as an alternative fuel for spark ignited (SI) internal combustion (IC) engines because of its higher flame propagation speed, wider ignition limits and lower ignition energy, when compared to hydrocarbon-based fuels [Verhelst *et al.*, 2007]. These properties allow hydrogen engines to run un-throttled, improving part load efficiency [White *et al.*, 2006]. Hydrogen, when burned in an IC engine, is generally considered to be a low-polluting fuel, due to its lack of carbon, and emissions such as soot, carbon-monoxide (CO) and carbon-dioxide (CO_2) are nearly eliminated. Oxides of nitrogen (NO_x) stand as the only emissions. Aside from being low polluting, hydrogen depletion is nearly impossible since it is abundant in various forms [Das, 1991; Gupta, 2006]. Hydrogen fuel also offers a solution for environmental and market demands since minimal design changes are required for existing IC engines [Gupta, 2006; Natkin *et al.*, 2002; Tang *et al.*, 2002]. Hydrogen fuel cells, an alternative to hydrogen fueled IC engines, allow for high efficiency and no carbon-based emissions; however, the cost of implementing

and creating fuel cells prevents fuel cells from being a highly marketable product.

Common problems associated with hydrogen IC engines are production of NO_x and low efficiency, since air contains 21% oxygen and 79% nitrogen [Smith, 1994; Verhelst and Sierens, 2007]. A typical IC engine operating on hydrogen achieves a maximum thermal efficiency around 30%. Using the indicated thermal efficiency for an ideal Otto cycle, written as a function of the engine's compression ratio (CR) and the specific heat ratio (γ) of in-cylinder gas [Heywood, 1988],

$$\eta_i = 1 - \frac{1}{CR^{(\gamma-1)}} \tag{1.1}$$

the maximum efficiency that can be achieved, assuming a compression ratio of 10 (typical compression ratio for an SI engine) and air as the in-cylinder gas, is about 60%. One method of controlling NO_x and improving efficiency consists of replacing nitrogen from the air with a monatomic gas such as argon. Noble gases, such as argon (1% of the Earth's atmosphere) and helium, are nonreactive and have only one mode of energy storage, translational motion, resulting in a high specific heat ratio ($\gamma = 1.67$ compared to $\gamma < 1.4$ for air). Recalculating the indicated efficiency using a noble gas instead of nitrogen and a compression ratio of 10 yields a maximum indicated thermal efficiency of 75% (eqn 1.1).

Improvement in thermal efficiency inspired a patent by Laumann et al. [Laumann *et al.*, 1978] that proposes a design for a hydrogen-oxygen-argon (H_2- O_2-Ar) IC engine. In this engine concept, water produced by combustion is condensed out of the system while argon is recycled in a closed loop system, preventing argon depletion. De Boer and Hulet [deBoer and Hulet, 1980] tested the feasibility of a hydrogen-oxygen-noble gas (argon) engine using a single cylinder, spark ignited Co-operative Fuel Research (CFR) engine. Varying the compression ratio between 5 and 12, they found that higher concentrations of argon produce higher indicated efficiencies but engine-knock limited spark advance, and in turn limited the maximum obtainable efficiency. Toyota [Mitani *et al.*, 2008; Kuroki *et al.*, 2010] also designed and tested a compact engine operating on H_2- O_2-Ar for commercial use. They achieved an indicated thermal efficiency of 54% and created a system that recycled argon and condensed water produced by combustion. However, knock and pre-ignition limited the maximum operating compression ratio.

One method of avoiding engine-knock is using a compression ignition engine. Ikegami et al. [Ikegami *et al.*, 1982] used a direct injection compression ignition engine to avoid engine-knock and take advantage of the thermodynamic properties of noble gases. Although, they achieved indicated thermal efficiencies close to 50% using compression ratios between 10 and 16, the amount of hydrogen injected at higher compression ratios was limited by the injection pressure of their system (76.5 bar). A major obstacle for achieving higher indicated thermal efficiencies in direct injection compression ignition engines is that hydrogen has high diffusivity and low viscosity, making it difficult to inject at higher pressures [Welch *et al.*, 2008]. Challenges faced with developing an injection system that can inject hydrogen at high pressures, prevents further development using H_2-O_2-Ar in compression ignition engines. Therefore, spark ignited engines are still considered ideal

for commercialized vehicles, since knock and pre-ignition can be prevented with delayed ignition [Kuroki *et al.*, 2010]. Chen et al. [Chen *et al.*, 2003b] further investigated auto-ignition delay times of hydrogen-oxygen-argon mixtures in compression ignition engines using a rapid compression machine. This section of the dissertation focuses on validating high efficiencies predicted operating a hydrogen-oxygen-argon engine and investigates methods for knock prevention.

1.1.2 HCCI Engines

HCCI engines are considered one of the most promising internal combustion engine concepts for the future because they offer the potential of high efficiencies and low nitrogen oxide and low soot emissions compared to conventional internal combustion engines [Zhao *et al.*, 2003]. HCCI engines are often considered a cross between a spark ignited (SI) engine and a Diesel engine. Similar to spark ignited (SI) engines, a homogenous air-fuel mixture charge is used for combustion, but like Diesel engines, a high compression ratio is used to auto-ignite the air-fuel mixture, which leads to higher thermal efficiencies [Killingsworth, 2007; Bogin, 2008; Souder, 2004].

In the early twentieth century, Carl Weiss and August Mietz developed the first HCCI-like combustion engine, called the hot-bulb engine [Erlandsson, 2002]. The hot-bulb engine offered a simple and durable design that had brake thermal efficiencies comparable to contemporary Diesel engines. The first published work on a gasoline-fueled HCCI engine was written by Onishi et al. [Onishi *et al.*, 1979] in 1979. The two-stroke gasoline engine, using a process dubbed Active Thermo-Atmosphere Combustion (ATAC) by the authors, increased fuel economy and decreased exhaust emissions at part-throttle operation. They also found that the ATAC engine was limited by insufficient combustion temperatures at low loads and knocking combustion at high loads. Similar work done by Noguchi et al. [Noguchi *et al.*, 1979], titled Toyota-Soken (TS) combustion, found heat rejection to the chamber walls and cycle-to-cycle variation important factors during the gas exchange process. In 1983, Najt and Foster [Najt and Foster, 1983] achieved compression ignition homogenous charge (CIHC) combustion in a four-stroke gasoline engine. Using the same engine as Najt and Foster, Thring [Thring, 1989] studied the effects of exhaust gas recirculation, intake temperature, and compression ratio; he was also the first to use the acronym HCCI [Thring, 1989]. Seven years after Thring, the first research burning Diesel fuel in an HCCI engine appeared [Ryan and Callahan, 1996; Gray and Ryan, 1997] and led to research testing other fuels, such as alcohols [Oakley *et al.*, 2001], hydrogen [Shudo and Ono, 2002], natural gas [Christensen *et al.*, 1997; Hiltner *et al.*, 2000; Olsson *et al.*, 2002; Flowers *et al.*, 2001a; Stanglmaier *et al.*, 2001], propane[Au *et al.*, 2001; Flowers *et al.*, 2001b], and many fuel blends with additives [Eng *et al.*, 2003; Yao *et al.*, 2009].

A few challenges associated with HCCI engine implementation are the limited operating range, controlling ignition timing, after-treatment of unburned hydrocarbon (THC) and carbon monoxide (CO) emissions, and predicting fuel performance [Yao *et al.*, 2009]. Because HCCI engines are capable of combusting a variety of fuels, the type of fuel significantly impacts engine design and control strategies [Christensen *et al.*, 1999; Yao *et al.*, 2009]. Epping et al. [Epping *et al.*, 2002] found that a fuel must have high volatility in order to easily form a homogenous charge and fuels with single-stage ignition are less sensitive to changes in load and speed. Most research efforts have focused on

gasoline or Diesel fuel for transportation HCCI engines and HCCI/SI hybrid technology [Dec, 2009; Zhang *et al.*, 2009; Zhu and Schock, 2010].

Predicting ignition and performance of fuels has proven to be challenging as autoignition in HCCI engines does not correlate well with research octane number (RON), motor octane number (MON), or the standard octane number, $(RON + MON)/2$ [Andrae *et al.*, 2008; Yao *et al.*, 2009; Anderson *et al.*, 2010]. Kalghatgi et al. [Kalghatgi, 2005] suggested the use of an octane index (different from octane number), which is determined using the RON, MON, and a constant (K factor), to predict autoignition in HCCI engines. However, the K factor varies with engine operating conditions and is engine specific, rendering the octane index impractical for use as a standardized method. Liu et al. [Liu *et al.*, 2008; Liu *et al.*, 2009] found that autoignition correlated well with the octane index (OI) for hydrocarbon fuel blends but did not correlate well with blends including ethanol. Their research also showed that the effects of fuel on the combustion process were strongly dependent upon the operating conditions [Liu *et al.*, 2008].

Research has also been conducted for studying additives that inhibit or promote the heat release process of auto-ignition in HCCI engines [Leppard, 1990; Westbrook *et al.*, 1991; Shibata *et al.*, 2005]. Shibata et al. [Shibata and Urushihara, 2007; Shibata and Urushihara, 2009] took their research a step further and developed an HCCI Index, which predicts ignition of fuel, using the fuel composition and MON or RON. More details on how additives affected fuel performance can be found in [Yao *et al.*, 2009]. Overall, previous research suggests that the best test fuel is gasoline based of medium octane and that ignition timing and reaction rates can be controlled by optimizing fuel composition [Yao *et al.*, 2009]. The focus of this dissertation, with respect to HCCI engines, is improving the accuracy for predicting auto-ignition and proposing a more representative number system for measuring and predicting fuel performance in HCCI engines.

1.2 Dissertation Overview

This section provides a brief description of the contents of this dissertation. As stated in the introduction, this dissertation focuses on two advanced engine concepts: a hydrogen-oxygen-argon (H_2-O_2-Ar) internal combustion (IC) engine and a homogenous charge compression ignition (HCCI) engine. Each chapter is organized by concept and, if applicable, common materials are discussed at the beginning of each chapter.

In Chapter 2, a background of the theory and calculations used for determining results in this dissertation are provided. Fuel chemistry for both engine concepts is outlined and variables for characterizing combustion in SI and HCCI engines are described.

In Chapter 3, the experimental engine and instrumentation used to test each advanced engine concept is described, including modifications made to the stock engine. Both concepts used the same engine, but had different experimental setups, which is described in the corresponding subsections. The use of variable compression ratio to prevent knock and control combustion timing is

demonstrated. Objectives and experimental design for the H_2-O_2-Ar internal combustion engine and the HCCI engine are described.

In Chapter 4, high efficiencies associated with operating a hydrogen-oxygen-argon SI engine are demonstrated for different argon concentrations. Efficiency limitations caused by engine knock are investigated. A three-zone model is used to explore solutions for reducing knock limitations and compare effects of specific heat ratio and flame speed on thermal efficiency.

In Chapter 5 existing methods for predicting auto-ignition (octane number, cetane number, and octane index) are tested in an HCCI engine. HCCI Indexes developed by Shibata and Urushihara [Shibata and Urushihara, 2007; Shibata and Urushihara, 2009] are also tested for predicting auto-ignition in an HCCI engine. Effectiveness of these methods are demonstrated. New trends and variables for use in a future index are also provided. A single-zone well-mixed-reactor (WMR) model is used for predicting experimental results and explaining fuel chemistry behavior.

In Chapter 6 an uncertainty analysis is provided for measured values and calculated variables.

In Chapter 7, a summary of the results and main conclusions is presented. Recommendations and future lines of research are also suggested.

1.3 Dissertation Contributions

This dissertation investigates two advanced engine concepts, using experimental and numerical techniques, to provide solutions for improving efficiency and reducing emissions of IC engines. A few key contributions to the scientific community are summarized below.

1. Application of the novel hydrogen-oxygen-argon engine: unlike previous research, high argon concentrations were tested for achieving high efficiencies using single and dual spark ignition. Although knock limited the maximum efficiency obtained, a better understanding of the knock limitation is provided.

2. Numerical modeling of the hydrogen-oxygen-argon engine: A multi-zone model was used to identify causes and solutions to knock limitations in the hydrogen-oxygen-argon engine. New correlations for curve-fitting flame speeds for hydrogen-oxygen-argon is provided.

3. Variables for a new, standardized HCCI number: Previous methods are shown to be inaccurate for predicting auto-ignition of all fuel blends in HCCI engines. This dissertation offers variables and trends, not previous published, that could be used in a future, standardized HCCI number or for further developing the existing HCCI Index. This dissertation explores twenty-four different fuels varying from reference fuels to gasoline blends. It also identifies pitfalls of the existing HCCI Index and offers suggestions for improvement. Fuel chemistry

is also explored to gain a better understanding of how different variables affect auto-ignition.

4. Single-zone WMR model for HCCI: A single-zone WMR model was used to predict experimental trends shown by the HCCI engine. Three different mechanisms were compared for predicting auto-ignition. Also, problems associated with auto-ignition of toluene blends are identified. The single-zone WMR model was also modified to account for blow-by. A fourth mechanism was used to explain experimental trends in the heat release data.

Chapter 2

Theory

2.1 Internal Combustion Engine Fundamentals

2.1.1 Homogeneous Charge Spark-Ignited (HCSI) Engines

HCSI engines, also known as gasoline engines or SI engines, commonly operate on a four-stroke cycle. During the first stroke, the intake stroke, a mixture of air and fuel is drawn into the cylinder as the piston moves downward. For the second stroke, the air-fuel mixture is compressed as the piston moves upward. Near the maximum height of the cylinder, top dead center (TDC), a spark triggers ignition, causing a premixed flame to propagate towards the piston, consuming the unburned air-fuel mixture. The force exerted on the piston from combustion results in the third stroke, the power stroke, which pushes the piston downward. During the last stroke, exhaust from combustion is pushed out of the cylinder as the piston moves upward once again. Because the fuel and air are premixed, rich pockets of fuel are reduced and thus particulate matter (PM) emissions are low. Details and images showing operation of a four-stroke spark-ignited engine can be found in Heywood and Stone[Heywood, 1988; Stone, 1999].

Challenges associated with HCSI engines include production of nitrogen-oxides (NO_x) and engine-knock. Production of NO_x is due to high peak combustion temperatures from running at stoichiometric conditions. After the spark plug has ignited the air-fuel mixture, a flame propagates through the cylinder, producing hot burned gases exceeding 1700K, resulting in the breakdown of N_2 in the air and the formation of NO_x [Warnatz *et al.*, 2006]. Engine-knock in HCSI engines limits the thermal efficiency and the compression ratio. Details outlining how engine knock occurs in HCSI engines and why it limits thermal efficiency and compression ratio can be found in Chapter 2.2.2.

2.1.2 Direct Injection Compression Ignited (DICI) Engines

In DICI engines, commonly known as Diesel engines, only air is drawn into the cylinder during the intake stroke. The air is then compressed, reaching temperatures and pressures that exceed

the ignition point of the fuel. High compression ratios are used to achieve an air temperature and pressure exceeding the ignition point of the fuel, which leads to increased thermal efficiencies. Late into the compression stroke, fuel is injected into the cylinder. After a delay period of a few crank angle degrees (CAD), spontaneous ignition occurs in portions of the already mixed fuel and air, resulting in the power stroke. After the power stroke, the piston moves upward again, pushing exhaust gases out of the cylinder [Heywood, 1988].

Unlike HCSI engines, the fuel-air mixture in DICI engines is heterogeneous and has rich pockets of fuel leading to high PM emissions. Also, ignition of DICI engines is controlled by fuel injection timing, not a spark plug. However, like HCSI engines, DICI engines produce high temperature, non-premixed flames from autoignition and result in high amounts of NO_x [Heywood, 1988; Stone, 1999].

2.1.3 Homogeneous Charge Compression Ignition (HCCI) Engines

As mentioned previously in the introduction, HCCI engines are often considered a cross between a spark ignited (SI) engine and a Diesel engine. Similar to HCSI engines, a homogenous air-fuel mixture is drawn into the cylinder during the intake stroke. But like DICI engines, a high compression ratio, rather than a spark, is used to autoignite the air-fuel mixture, leading to DICI-like thermal efficiencies. HCCI engines also offer low NO_x emissions due to low peak in-cylinder temperatures from combusting diluted air-fuel (lean) mixtures. Because the air and fuel are premixed, like HCSI engines, PM emissions is also low [Killingsworth, 2007; Bogin, 2008; Souder, 2004].

In HCCI engines, ignition is controlled by chemical kinetics. Ignition timing is extremely dependent on the temperature and pressure history of the air-fuel mixture, making the start of combustion difficult to control. Because the chemical kinetics process is fuel composition dependent, predicting ignition is also challenging [Dec, 2009; Yao *et al.*, 2009].

2.2 Engine Performance Parameters

2.2.1 Equivalence Ratio and Normalized Air-Fuel Ratio

The equivalence ratio is defined as

$$\phi = \frac{m_{fuel}/m_{ox}}{(m_{fuel}/m_{ox})_{st}}, \tag{2.1}$$

where m_{fuel}/m_{ox} is the measured ratio of mass of fuel to mass of oxidizer and $(m_{fuel}/m_{ox})_{st}$ is the stoichiometric ratio of mass of fuel to mass of oxidizer. In this dissertation, the normalized air-fuel ratio,λ, defined as $1/\phi$ is used and is determined using several methods.

One method for determining λ assumes that the mass flow rate of the air and fuel can be measured. Using these values, λ can be found by

$$\lambda = \frac{AFR}{AFR_{st}}, \tag{2.2}$$

where AFR is the measured air to fuel ratio and AFR_{st} is the stoichiometric air to fuel ratio of the fuel [Heywood, 1988; Stone, 1999].

Another method for determining λ, using the measured emissions, is

$$\lambda = 1 + \left(\frac{n_C}{n_C + \frac{n_H}{4} - \frac{n_O}{2}} \right) \frac{[O_2]}{[CO_2]}, \tag{2.3}$$

where n_C is the number of carbon atoms in the fuel, n_H is the number of hydrogen atoms in the fuel, n_O is the number of oxygen atoms in the fuel, $[O_2]$ is the percent oxygen measured in the emissions, and $[CO_2]$ is the percent carbon-dioxide measured in the emissions.

White [White, 2003] proposes another method for computing λ using.

$$\lambda = \frac{[CO_2] + \left[\frac{CO}{2}\right] + [O_2] + \left[\frac{NO}{2}\right] + \left(\left(\frac{H_{CV}}{4} \times \frac{3.5}{3.5 + [CO]/[CO_2]} \right) - \frac{O_{CV}}{2} \right) \times ([CO_2] + [CO])}{\left(1 + \frac{H_{CV}}{4} - \frac{O_{CV}}{2}\right) \times ([CO_2] + [CO] + (C_{factor} \times [HC]))}, \tag{2.4}$$

where $[xx]$ is the gas concentration in percent volume, H_{CV} is the atomic ratio of hydrogen to carbon in the fuel, O_{CV} is the atomic ratio of oxygen to carbon in the fuel, and C_{factor} is the number of carbon atoms in each of the hydrocarbon molecules being measured (i.e. Hexane - 6, Propane = 3, Methane = 1, etc.)[White, 2003].

Spindt [Spindt, 1965] proposes another method for computing λ with exhaust emissions:

$$\lambda = F_b \left[11.492 F_c \left(\frac{1 + R/2 + Q}{1 + R} \right) + \left(\frac{120 F_h}{2.5 + R} \right) \right]. \tag{2.5}$$

F_b, R, and Q can be determined by

$$F_b = \frac{P_{CO} + P_{CO_2}}{P_{CO} + P_{CO_2} + P_{CH}},$$

$$R = \frac{P_{CO}}{P_{CO2}}, \text{ and}$$

$$Q = \frac{P_{O_2}}{P_{CO_2}}.$$

F_c and F_h represent the mass fraction of carbon and hydrogen, respectively, in a hydrocarbon fuel. P_{xx} represents the percent of the compound measured from an exhaust analyzer. P_{CH} is the

percent carbon in hydrocarbons on a per carbon basis. Spindt's [Spindt, 1965] equation can be modified to include oxygenated fuels yielding,

$$\lambda = F_b \left[11.492 F_c \left(\frac{1 + R/2 + Q}{1 + R} \right) + \left(\frac{120 F_h}{2.5 + R} \right) - \left(\frac{4.31 F_o}{F_b} \right) \right], \tag{2.6}$$

where F_o is the fraction of oxygen in the fuel.

Heywood [Heywood, 1988] also uses a modified version of Spindt's [Spindt, 1965] equation, assuming the fuel is comprised of carbon and hydrogen only,

$$\lambda = 4.773 \left(\frac{M_{air}}{M_f} \right) \frac{(CO_2) + (CO)/2 + (H_2O)/2 + (NO)/2 + (NO_2) + (O_2)}{(HC) + (CO) + (CO_2)}, \tag{2.7}$$

where (xx) are molar concentrations in percent, $M_{air} = 28.96$, and $M_f = 12.01 + 1.008y$ where y is the H/C ratio of the fuel, *(HC)* is molar percent unburned hydrocarbons as C_1, and

$$(H_2O) = 0.5y \frac{(CO_2) + (CO)}{(CO)/[K(CO_2)] + 1}.$$

K is a constant and commonly has a value of 3.5 or 3.8 [Heywood, 1988].

2.2.2 Autoignition and Engine Knock

Autoignition, often called a self-explosion, is defined as the rapid combustion reaction of an air-fuel mixture that is not initiated by an external ignition source, such as a spark or flame. Two types of explosions are often used to describe autoignition: thermal explosions and chain-branching explosions. Thermal explosions occur when the energy released by the reaction, usually in the form of heat, is larger than the heat lost to the surroundings, increasing the temperature of the air-fuel mixture and rapidly accelerating the reaction rates. Chain-branching explosions occur when propagating reactions are chain-branching reactions (two reactive radicals are produced for each radical consumed), resulting in a rapid increase in radicals leading to an increase in reaction rates. In many situations, autoignition can occur from a combined thermal and chain-branching explosion [Heywood, 1988].

In SI engines, autoignition commonly occurs as a thermal explosion and leads to engine-knock. As the flame moves through the engine cylinder, the unburned gas ahead of the flame front (end-gas) is compressed by the expanding burnt gas, causing it to increase in temperature and pressure until the flame consumes it. If the temperature and pressure of the end-gas increases too much before being consumed by the flame, autoignition of the end-gas can occur. Autoignition of the end-gas can result in a rapid release of the chemical energy of the end-gas, which can in turn create high amplitude pressure waves inside the cylinder. This phenomenon is often referred to as knock or engine-knock. Knock can cause severe engine damage due to increased mechanical and thermal stress. The tendency of an engine to knock depends on the properties of the fuel,

the engine design, the equivalence ratio (ϕ), and the engine speed [Verhelst and Wallner, 2009; Heywood, 1988].

One method of predicting knock is observing the temperature rise during compression. Assuming isentropic compression, the temperature rise can be estimated using,

$$T_2 = T_1(CR)^{\gamma-1}, \tag{2.8}$$

where T_1 is the absolute initial temperature and T_2 is the absolute final temperature [EERE, 2001]. In equation 2.8, the compression ratio is limited by the autoignition temperature, represented by T_2. Using a compression ratio that results in a T_2 exceeding the autoignition temperature of the fuel leads to engine knock.

2.2.3 Work, Power, and Mean Effective Pressures

The indicated work per cycle is obtained by computing the area enclosed by the engine P-V diagram curve [Heywood, 1988; Lancaster *et al.*, 1975].

$$W_i = \oint p dV, \tag{2.9}$$

where p is the pressure and V is the volume. Using the trapezoidal method of integration, the indicated work can be approximated by,

$$W_i = \sum_{i}^{N-1} \Delta V_i \frac{p_{i+1} + p_i}{2}, \tag{2.10}$$

where N is the number of divisions [Heywood, 1988]. Knowing geometrical properties of the engine, the volume can be determined at each crank angle degree using

$$V = V_c + \frac{\pi B^2}{4}(l + a - a\cos\theta - (l^2 - a^2\sin^2\theta)^{\frac{1}{2}}), \tag{2.11}$$

where V_c is the clearance volume, B is the bore, l is the connecting rod length, and a is crank radius [Heywood, 1988].

Knowing the indicated work, the indicated power per cycle can be found by,

$$P_i = \frac{W_i RPM}{n_R}, \tag{2.12}$$

where n_R is the number of crank revolutions for each power stroke per cylinder and RPM is the engine speed. For a four-stroke engine $n_r = 2$ and for a two-stroke engine $n_R = 1$.

Although work and power are useful for determining the performance of the engine, they are

dependent on the size of the engine. A useful means of comparing an engine's ability to do work, regardless of engine size is using the indicated mean effective pressure (IMEP), which is defined as

$$\text{IMEP} = \frac{W_i}{V_{swept}}, \tag{2.13}$$

where V_{swept} is the swept (displacement) volume [Heywood, 1988]. The coefficient of variation (COV) in IMEP is also a useful tool as it defines the cyclic variability in indicated work per cycle:

$$\text{COV}_{IMEP} = \frac{\sigma_{IMEP}}{x_{IMEP}} \times 100, \tag{2.14}$$

where σ_{IMEP} is the standard deviation in IMEP and x_{IMEP} is the mean IMEP. As COV_{IMEP} increases, engine operation becomes unstable, leading to partial burn cycles and misfires [Heywood, 1988].

2.2.4 Heat Release and CA50

From the first law of thermodynamics, the net heat release per crank angle degree ($dQ/d\theta$) can be defined as,

$$\frac{dQ}{d\theta} = \frac{\gamma}{\gamma - 1} p \frac{dV}{d\theta} + \frac{1}{\gamma - 1} V \frac{dp}{d\theta}, \tag{2.15}$$

where γ is the heat ratio C_p/C_v [Stone, 1999]. Because pressure is measured discretely, numerically differentiating the pressure will amplify the signal noise. To avoid differentiating the pressure, 2.15 can be rewritten using $\frac{d(pV)}{d\theta} = p\frac{dV}{d\theta} + V\frac{dp}{d\theta}$ [Killingsworth, 2007],

$$\frac{dQ}{d\theta} = \frac{1}{\gamma - 1} \frac{d(pV)}{d\theta} + p \frac{dV}{d\theta}. \tag{2.16}$$

Using equation 2.16, Q can be computed as a finite sum instead of a continuous integral [Killingsworth, 2007]

$$Q_i = \frac{1}{\gamma - 1}[p_i V_i - p_0 V_0] + \sum_{j=0}^{i} p_j (\Delta V)_j. \tag{2.17}$$

In this dissertation, ignition timing of HCCI engines is determined using CA50, or the crank angle degree when half of the net heat has been released. Using equation 2.15, CA50 is defined as the crank angle position $\theta_{Q_{50\%}}$ where,

$$Q_{50\%} = \frac{1}{2}(Q_{max} - Q_{min}). \tag{2.18}$$

Figure 2.1 demonstrates graphically how CA50 is determined.

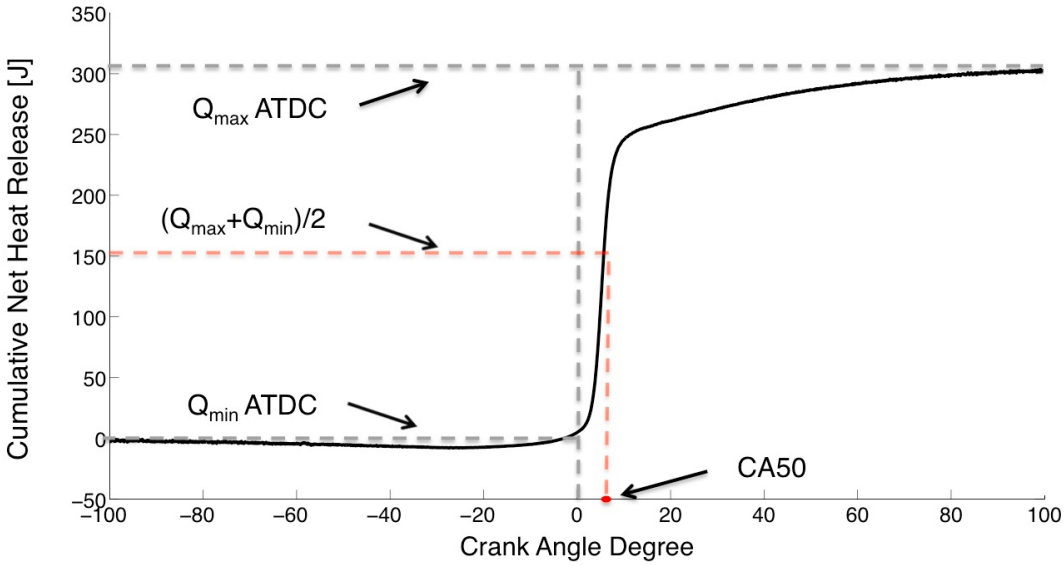

Figure 2.1: Graphical definition of CA50. ATDC is after top dead center

2.2.5 Efficiencies

Thermal efficiency is defined as ratio of work out divided by heat in,

$$\eta_{th} = \frac{W_{out}}{Q_{in}}. \tag{2.19}$$

For an ideal spark ignited engine, equation 2.19 can be rewritten as equation 1.1. In this dissertation, indicated thermal efficiency is obtained by,

$$\eta_{th,i} = \frac{W_{i,out}}{m_f Q_{LHV}}, \tag{2.20}$$

where m_f is the mass of the fuel and Q_{LHV} is the lower heating value of the fuel.

Combustion efficiency is determined using,

$$\eta_{comb} = \frac{Q_{max}}{m_f Q_{LHV}}, \tag{2.21}$$

where Q_{max} is the maximum heat release of the fuel and is obtained using equation 2.17.

2.3 Fuel Chemistry

2.3.1 Hydrogen Combustion

Hydrogen is an ideal fuel for IC engines from the aspect that it offers a high autoignition temperature (858 K) and lower ignition energy (0.02 mJ) [EERE, 2001]. Because hydrogen has a higher autoignition temperature and flame velocity, compared to gasoline, hydrogen-air mixtures do not tend to knock under stoichiometric conditions, except when the compression ratio is very high [EERE, 2001; White *et al.*, 2006; Verhelst and Wallner, 2009]. Unless a stoichiometric hydrogen-oxygen mixture is ignited by an external source, no reactions occur below 400°C. Temperatures exceeding 600°C lead to autoignition of the hydrogen-oxygen mixture at all pressures [Heywood, 1988]. Autoignition of hydrogen-oxygen mixtures is initiated by $H_2 + M \rightarrow \dot{H} + \dot{H} + M$ and followed by three radical-producing, chain-sequence reactions:

$$\begin{aligned} \dot{H} + O_2 &= \dot{O} + \dot{OH} \\ \dot{O} + H_2 &= \dot{H} + \dot{OH} \\ H_2 + \dot{OH} &= H_2O + \dot{H} \end{aligned}$$

The first two reactions are chain-branching, while the third reaction completes the chain sequence [Heywood, 1988]. These reactions lead to high concentrations of radicals and eventually to autoignition of a hydrogen-oxygen mixture. The stoichiometric equation for hydrogen combustion in air is represented by the following reaction:

$$H_2 + \frac{1}{2}(O_2 + 3.76N_2) \rightarrow H_2O + 1.88N_2.$$

However, peak temperatures during combustion often lead to dissociation of N_2, leading to production of NO_x [EERE, 2001].

2.3.2 Hydrocarbon Fuel Combustion

Autoignition of basic hydrocarbon (RH) fuels can be described by an oxidation process from Semenov [Heywood, 1988]:

$$\begin{aligned} RH + O_2 &\longrightarrow \dot{R} + H\dot{O}_2 && \text{(R1)} \\ \dot{R} + O_2 &\longrightarrow R\dot{O}_2 && \text{(R2)} \\ \dot{R} + O_2 &\longrightarrow \text{olefin} + H\dot{O}_2 && \text{(R3)} \\ R\dot{O}_2 + RH &\longrightarrow ROOH + \dot{R} && \text{(R4)} \\ R\dot{O}_2 &\longrightarrow R'CHO + R"O && \text{(R5)} \\ H\dot{O}_2 + RH &\longrightarrow H_2O_2 + \dot{R} && \text{(R6)} \\ ROOH &\longrightarrow \dot{RO} + \dot{OH} && \text{(R7)} \\ R'CHO + O_2 &\longrightarrow R'\dot{C}O + H\dot{O}_2 && \text{(R8)} \\ R\dot{O}_2 &\longrightarrow \text{destruction} && \text{(R9)} \end{aligned}$$

The chain initiation reaction is represented by the reaction (R1). Chain propagating reactions are represented by reactions (R2) - (R6). Degenerate branching reactions are reactions (R7) and (R8). Reaction (R9) is the chain termination reaction. Molecules with a dot are active radicals and ones with primes represent free bonds on the organic radical R.

2.3.3 Low Temperature Combustion

HCCI engines commonly operate in a lower temperature regime than SI engines and fuel chemistry can greatly affect when autoignition occurs [Liu *et al.*, 2009]. Aside from fuel behavior, achieving autoignition for high octane number fuels in HCCI engines can be challenging because a high compression ratio, high intake temperature, or boosted intake pressure is required.

Augotignition of the fuel in HCCI engines often occurs in two stages, a low temperature combustion regime and a high temperature combustion regime. At high temperatures, alkyl radicals often decompose into a smaller alkyl radical and a small olefin [Zhao, 2007]. For example, at high temperatures, n-heptane (C_7H_{16}) may decompose by the following reactions:

$$\begin{aligned} C_7H_{16} + \dot{OH} &\rightarrow C_7\dot{H}_{15} + H_2O \\ C_7\dot{H}_{15} &\rightarrow C_3\dot{H}_7 + C_4H_8 \end{aligned}$$

However, at temperature below 1000K, alkyl radicals mostly react with molecular oxygen in the following manner [Zhao, 2007; Warnatz *et al.*, 2006]:

$$\begin{aligned} RH + \dot{OH} &\rightarrow \dot{R} + H_2O \quad \text{(R10)} \\ \dot{R} + O_2 &\leftrightarrow R\dot{O}_2 \quad \text{(R11)} \end{aligned}$$

The second reaction is the key to initiating low temperature combustion. The forward direction of the reaction has almost no activation barrier and is influenced by concentrations of R and molecular oxygen. It is also leads to the production of RO_2, which initiates the main chain branching reaction pathway of low temperature combustion. Because the amount of chemical species is constantly changing in this reaction, the forward reaction rate depends more on pressure than the reverse. The reverse reaction has a high activation energy barrier, making it more temperature dependent. When temperatures increase to the point where the reverse reaction dominates, extinguishing production of RO_2 and low temperature chain branching, the rate of combustion decreases significantly. Full details of the reactions involved in low temperature combustion can be found in chapter 17 of Zhao [Zhao, 2007].

Transition between low temperature combustion and high temperature combustion can often be visualized by plotting the heat release rate during combustion. As shown in Figure 2.2, low temperature combustion appears as low temperature heat release (LTHR) followed by a high temperature heat release (HTHR) from the high temperature combustion. Understanding how LTHR and HTHR affect ignition is one method being explored for predicting autoignition in HCCI engines [Liu *et al.*, 2009].

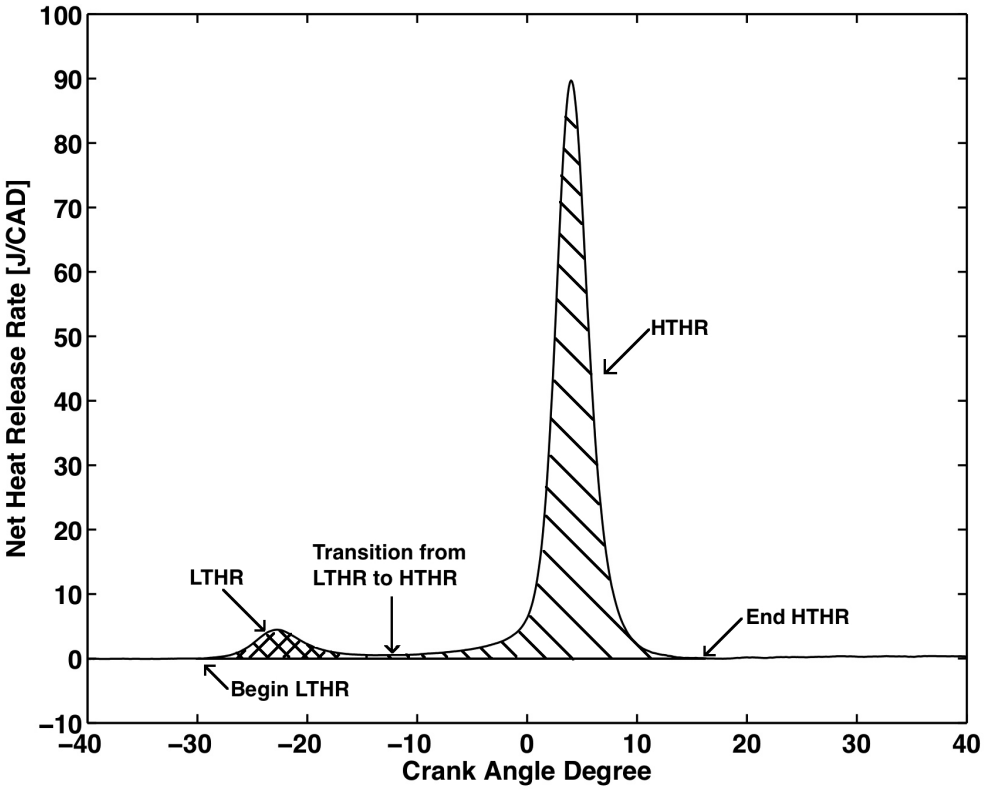

Figure 2.2: Low temperature heat release (LTHR) from low temperature combustion and high temperature heat release (HTHR) from high temperature combustion.

Chapter 3

Experimental Apparatus

All experiments were conducted using a single cylinder, port fuel injected, variable compression ratio, Waukesha Cooperative Fuel Research (CFR) F-4 engine, shown in figure 3.1. This engine was originally designed to test octane numbers of aviation fuels [ASTM Standard D909-07, 2007], but has been modified in the current work to operate both as an SI engine and an HCCI engine. Engine specifications can be found in table 3.1. Common instrumentation for both advanced engine concepts, H_2-O_2-Ar and HCCI, is described in the next section. Following the common instrumentation section, the experimental setup specific to each engine concept is described and an experimental design is provided.

Table 3.1: Engine Specifications

Displacement	0.616 L
Bore	3.26 in
Stroke	4.5 in
Crank radius	Stroke/2 =2.25 in
Connecting Rod Length	10.0 in
Compression Ratio	4 - 17.5
Piston Material	Aluminum
Number of Piston Rings	3 compression, 2 oil (5 total)
Camshaft Overlap	30 deg

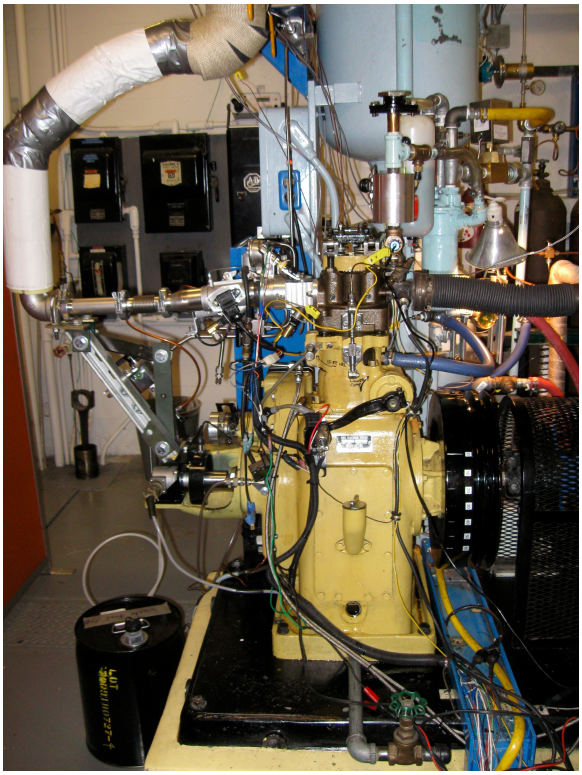

Figure 3.1: Cooperative Fuel Research Engine at UC Berkeley

3.1 Common Instrumentation

In-cylinder pressure was measured using a 6052B Kistler piezoelectric pressure transducer in conjunction with a 5044A Kistler charge amplifier. Intake pressure was measured using a 4045A5 Kistler piezoresistive pressure transducer in conjunction with a 4643 Kistler amplifier module. Sampling of in-cylinder and intake pressures was hardware timed using an optical encoder, and recorded every 0.1 crank angle (CA) degree. A dynamometer, directly coupled to the engine crankshaft, was used for motoring and absorbing power during combustion. Specifications can be found in table 3.2. An ABB variable speed frequency drive controlled the dynamometer and in turn controlled the engine speed. A Motec M4 ECU (Engine Control Unit) controlled spark timing (when applicable), injection timing, and injection pulse width. Details regarding the cooling system can be found in Appendix B. A five-gas Horiba Analyzer was used to measure concentrations of carbon monoxide (CO), unburned hydrocarbons (THC), nitrogen oxides (NO_x), and molecular oxygen (O_2). Details of the emissions gas analyzer can be found in Appendix D.

Table 3.2: Dynamometer Specifications

Type	HDM 365
Max No-Load RPM	1800 RPM
Max Power Delivered	25 HP at 1750 RPM
Max Power Absorbed	27 HP at 1855 RPM
Full Load Current Delivered	40 Amp
In Rush Current	170 Amp (at full voltage)
Manufacturer	Harnischfeger Corp., Milwaukee Wis. USA

3.2 H_2-O_2-Ar Operation

3.2.1 Experimental Setup

The CFR engine was operated as a spark ignited engine using a cold-type, iridium spark plug (Bosch R0 685). Three bottles of high-pressure gas cylinders, one containing pure argon, the second with a mixture of oxygen and argon, and the third with pure hydrogen, were used to supply desired gas-mixtures to the engine. Pure oxygen could be blended with argon independently, but for safety reasons we use premixed oxygen and argon, which was then blended with argon for higher dilutions. Flow rates of compressed argon and argon-oxygen were determined using calibrated sonic orifices. Software controlled electronic pressure regulators set the flow rates by adjusting the gas pressure upstream of the sonic orifices.

Hydrogen was injected using a Quantum gaseous fuel injector at a pressure of 40 psi. The mass of hydrogen injected was measured using a mass flow sensor (Alicat M Series Mass Flow Meter) and was verified using a Horiba five-gas emissions analyzer [Natkin *et al.*, 2002]. When operating at stoichiometric conditions, $\lambda = 1$, a wide band lambda sensor was primarily used.

All experiments were conducted without throttling the engine at constant intake pressure of 0.98 bar. The engine was pre-heated by burning hydrogen-air, bringing the coolant temperature to 75C, which conserved argon. This temperature was maintained for the recorded tests using a closed-loop controller. The crankcase was purged with nitrogen, preventing accidental explosion of any hydrogen that might have blown by the rings.

Initially, when running the engine on hydrogen-air mixtures, significant problems with back-flash (ignition of the fuel before the intake valve closes) occurred. It was found that the back-flash occurred because of residual charge in the spark plug wire created from the previous cycle's ignition [Kondo *et al.*, 1997]. Back-flash problems ceased after the spark plug wires in our system were modified as described by Kondo et al. [Kondo *et al.*, 1997].

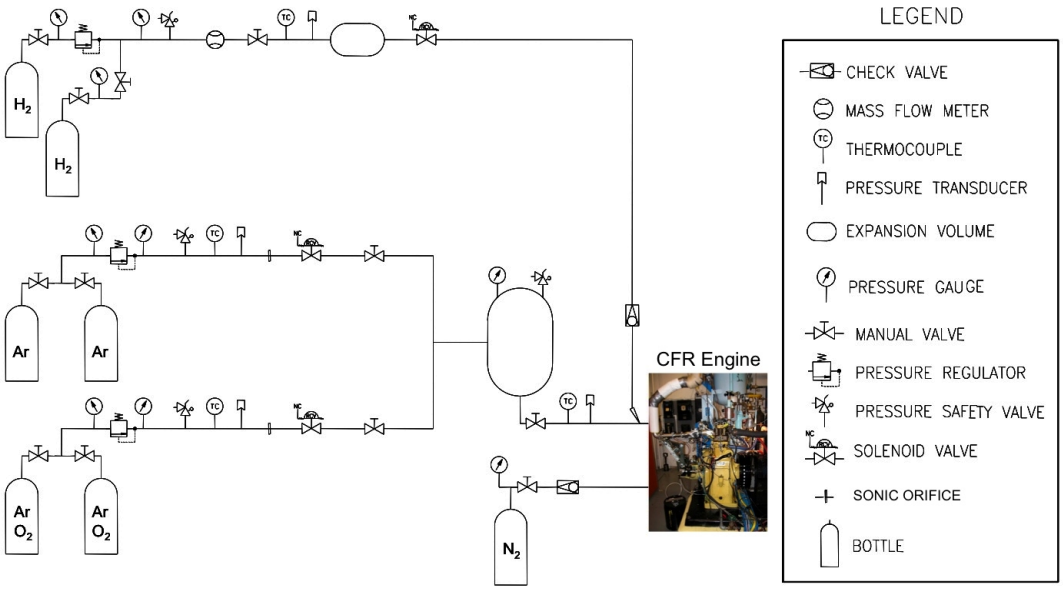

Figure 3.2: Experimental Configuration

3.2.2 Experimental Design

Previous experiments showed that high argon concentrations resulted in the highest efficiency in a H_2-O_2-Ar engine [deBoer and Hulet, 1980]. Therefore, spark timing sweeps, using both single and dual spark ignition, were conducted for high argon concentration blends shown in Table 3.3. Reported spark timings produced the maximum brake torque (minimum ignition advance for best torque [Stone, 1999]) and, when operating dual spark ignition, spark plugs ignited simultaneously. The compression ratio was varied from 4.5 to 7, in half compression ratio increments, for each blend. Engine specifications and operating conditions can be found in table 3.5. Fuel pressure in the hydrogen line was held at 40 psig and the crankcase was purged with nitrogen, preventing accidental explosion of any hydrogen in air that may blow by the rings into the crankcase.

Experiments were also conducted using hydrogen-air for comparison with H_2-O_2-Ar experiments. An equivalence ratio of 0.24 was chosen for hydrogen-air operation because the mass fraction of hydrogen in the air mixture matches the mass fraction of H_2-O_2-Ar mixtures with 86% argon. The compression ratio was varied from 6 to 17 and spark timing was swept at each compression ratio to achieve maximum brake torque. For each set-point 400 thermodynamic cycles (each cycle with 720 CAD) of in-cylinder pressure data were collected.

Table 3.3: Fuel-Oxidizer-Ar Mixture Concentrations by Volume

	H_2	O_2	Ar
Blend 1	10.67%	5.33%	84%
Blend 2	9.33%	4.67%	86%
Blend 3	8.0%	4.0%	88%

Table 3.4: Engine Specifications for H_2-O_2-Ar

Engine Speed	900 RPM
Coolant Temperature	75° C ± 1° C
Intake Pressure	0.98 bar
Intake Temperature	23°C± 1° C

3.3 HCCI Operation

3.3.1 Experimental Setup

Details regarding the fueling and intake system can be found in Appendix B. Intake air-flow was determined using a sonic orifice. Details regarding the orifice can be found in Appendix C. A five-gas Horiba analyzer (Appendix D) was used to measure emissions shown in Appendix E. Equivalence ratio was calculated using four different methods, described in Chapter 2.2.1 (specifically, equations 2.3, 2.4, 2.6, and 2.7), and the emissions data. The best method for calculating equivalence ratio was determined by matching the wide-band lambda sensor measurements and the calculated equivalence ratios at stoichiometric conditions. Comparing Equations 2.3-2.7 to the wide band lambda sensor, the best fit for equivalence ratio was equation 2.3. Therefore, for all equivalence ratio estimates, equation 2.3 was used to estimate equivalence ratio. Fuel injector pressure was kept constant at 40psi and fuel flow was determined using a Motec ECU.

3.3.2 Experimental Design

Before collecting data for each experiment, the engine was pre-heated until coolant temperature reached 80°C and combustion became steady. Engine specifications and operating conditions can be found in Table 3.5. These conditions were chosen to isolate fuel characteristics that could be used to create an HCCI index. The intake temperature of 151°C, and engine speed of 600 RPM were chosen to operate the widest range of fuels in the HCCI engine. For each experiment, equivalence ratio was held constant and ϕ=0.33 (λ=3.0) using equation 2.3. Compression ratio was varied to find the limits of stable HCCI for each fuel. The highest compression ratio for each fuel was determined when the in-cylinder pressure exceeded 50 bar (the maximum allowable pressure inside the cylinder) or the ringing intensity became too great [Eng, 2002]. The lowest compression ratio was determined when HCCI operation became unstable. For each compression ratio sweep, 300 thermodynamic cycles (each cycle with 720 CAD) of in-cylinder pressure data were collected

along with emissions. Overall, twenty-four different fuels were tested and one fuel was tested with variable intake temperature.

Table 3.5: Engine Specifications for HCCI Operation

Engine Speed	600 RPM
Coolant Temperature	80° C ± 1° C
Intake Pressure	1.035 bar
Intake Temperature	150°C± 1° C
Equivalence Ratio (ϕ)	0.33

Table 3.6 contains the reference fuel blend compositions (by volume percent), RON, and MON. For most of the reference fuels, the RON and MON values were measured or calculated. The RON and MON values for TRF70 were estimated using a linear-by-volume blending equation, developed for fuel blends containing toluene, isooctane, and n-heptane, created by Morgan et al. [Morgan *et al.*, 2010]. The linear-by-volume blending equation was verified by comparing calculated and measured RON and MON for S70. E-PRF70 RON and MON values were estimated using the blending RON and MON values from Anderson et al. [Anderson *et al.*, 2010].

Table 3.6: Reference Fuel Blend Compositions by Volume Percent with RON and MON

Fuel Name	% Isooctane	% n-heptane	% Toluene	% Ethanol	RON	MON
PRF 60	60	40	0	0	60	60
PRF 70	70	30	0	0	70	70
PRF 75	75	25	0	0	75	75
PRF 85	85	15	0	0	85	85
PRF 88	88	12	0	0	88	88
TRF 70*	0	46	54	0	70.5	63.5
S 70	64	31	5	0	70.5	69.6
E-PRF 70$^+$	64	31	0	5	70.5	68.6
n-heptane	0	100	0	0	0	0

*RON and MON were calculated using method described by Morgan et al [Morgan *et al.*, 2010].
$^+$RON and MON were calculated using bRON and bMON values from [Anderson *et al.*, 2010].
RON and MON of remaining fuels were assumed.

Two different base gasolines were provided by Chevron, labeled Gas and Gas2 respectively. RON and MON for the base gasoline fuels can be found in Table 3.7. The base gasoline fuels were blended with different additives, such as N-heptane, Ethanol, different naphthenes, and different aromatics. The gasoline fuel blends tested are listed in Table 3.8 along with the type of additive, the RON, and the MON. The exact composition of the gasoline blends was unknown, except by Chevron. Additional experiments for PRF70 were conducted at intake temperatures of 69°C and

115°C and compression ratio was varied to achieve the same CA50 and equivalence ratio.

Table 3.7: Base Gasoline Fuels with RON and MON

Fuel Name	RON	MON
Gas	87	80
Gas2	70	65

Table 3.8: Gasoline Fuel Blends with Specified Additives, RON, and MON

Fuel Name	Additive	RON	MON
GasB1	N-heptane	70^{+}	65^{+}
GasB2	Ethanol	93^{*}	84^{*}
GasB3	Ethanol	90^{*}	82^{*}
GasB4	Aromatic 1	91^{*}	82^{*}
GasB5	Naphthene 2	90^{+}	N/A
GasB6	Naphthene 3	88^{+}	82^{+}
GasB7	Naphthene 4	87^{+}	81^{+}
GasB8	Naphthene 1	86^{+}	79^{+}
GasB9	Aromatic 2	91^{+}	82^{+}
GasB10	Aromatic 3	93^{+}	83^{+}
Gas2B1	N-heptane	60^{*}	55^{*}
Gas2B2	Ethanol	78^{*}	68^{*}
Gas2B3	Naphthene 1	N/A	N/A

"N/A" implies the RON and/or MON values were not available.

*RON and/or MON were estimated.

$^{+}$RON and/or MON were provided by Chevron.

Chapter 4

Hydrogen-Oxygen-Argon Engine

The objective of this project is to experimentally demonstrate the predicted increase in efficiency by operating a hydrogen-oxygen-argon (H_2-O_2-Ar) engine. In this chapter, experimental results operating this engine are presented using dual and single spark ignition for argon concentrations of 84% (Blend 1), 86% (Blend 2), and 88% (Blend 3). For each concentration of argon, stoichiometric fuel-oxygen mixtures were used, as described in table 3.3. Results using a three-zone model to compare the effects of specific heat ratio and flame speed on thermal efficiency are also presented.

4.1 Experimental Results and Discussion

4.1.1 Effects of Single Spark Ignition

Shown in figure 4.1 is the dependence of the indicated thermal efficiency, η_i, on spark timing at compression ratios of 4.5 and 5.5. For all Blends at a compression ratio of 4.5, the indicated thermal efficiency increases, peaks, and then decreases as spark timing is advanced [Heywood, 1988; Stone, 1999]. However, at a compression ratio of 5.5, a maximum indicated thermal efficiency, similar to figure 4.1(a), was not observed due to knock limiting the spark advance. In the following results, the maximum brake torque spark timing is associated with the peak indicated thermal efficiency.

At a compression ratio of 4.5, Blend 3 required the most advance spark timing (-63°ATDC), as shown in figure 4.2, to achieve maximum brake torque. Because Blend 3 has the least amount of hydrogen, the spark timing is the most advanced and has the lowest peak pressure. Also, higher concentrations of argon require more advanced spark timing due to reduced flame speeds. After determining the spark timing associated with the maximum break torque, changes in thermal efficiency with compression ratio were investigated.

Shown in figure 4.3, the indicated thermal efficiency peaks at a compression ratio of 5.5 for all Blends. Previous studies, in which thermal efficiency was calculated using a dynamometer,

predicted a peak at a compression ratio of 7 for similar concentrations of argon [deBoer and Hulet, 1980]. However, spark timing and percentage of knocking cycles could attribute to differences between these results.

From figure 4.4, it can be seen that the highest indicated mean effective pressure (IMEP) occurs between compression ratios of 5 and 5.5. The maximum IMEP, 4.3 bar, occurs with Blend 1 at a compression ratio of 5.5, which agrees with previous results [deBoer and Hulet, 1980]. Also, IMEP increases as concentration of argon decreases. An increase in IMEP with a decrease in argon concentration is due to the increase in hydrogen and oxygen, which leads to knock. As expected, IMEP does not vary with compression ratio because it is a function of equivalence ratio, which is constant.

Shown in figure 4.5, IMEP does not vary significantly with spark timing. At a compression ratio of 5.5, IMEP is nearly constant; this is true for all compression ratios tested. Blend 1 produces the lowest indicated thermal efficiency and the highest IMEP. Blend 2, produces the highest indicated efficiency of 45%. Experiments performed at compression ratios greater than 6 experienced intense knocking which limited spark advance. Therefore, very late spark timing was required to avoid knock. Trends in IMEP for other compression ratios showed similar results.

4.1.2 Effects of Dual Spark Ignition

A second spark plug was added to the engine to reduce end gas residence time and reduce knock. When operating under dual spark ignition, engine knocking still limited spark advance for all compression ratios. Stable operation of the engine at compression ratio of 7 was unsuccessful due to the intensity of knock therefore, results are only shown for compression ratio of 4.5 to 6.5. Although knock limited spark advance, the indicated thermal efficiency improved slightly when compared to single spark ignition, but still did not exceed 50%.

Figure 4.6, shows indicated thermal efficiency, using dual spark ignition, does not peak like single spark ignition. Instead, indicated thermal efficiency monotonically increases with compression ratio. This suggests that a maximum indicated thermal efficiency could occur near a compression ratio of 7, as shown by deBoer and Hulet [deBoer and Hulet, 1980]. For dual spark ignition, knock limits the spark advance, which in turn limits the maximum efficiency. However, the dual spark does slightly increase the maximum efficiency ($\approx$45% for single spark and $\approx$46% for dual spark). At higher concentrations of argon, dual spark produces higher indicated thermal efficiency at all compression ratios. The most significant improvement in indicated thermal efficiency occurred using Blend 3, shown in figure 4.7.

The pressure trace inside the cylinder for each Blend, using dual spark ignition, at a compression ratio of 6.5 is shown in figure 4.8. Like figure 4.2, the pressure trace was generated using the most advanced spark timing obtainable under the operating conditions (6°ATDC for Blend 1, 1°ATDC for Blend 2, and -6°ATDC for Blend 3).

Figure 4.9 shows that advancing the spark timing increases indicated thermal efficiency. For

higher concentrations of argon, using dual spark ignition, flame speeds are reduced and require an advance in spark timing, much like single spark ignition. However, spark timing for dual spark ignition is more delayed than single spark ignition at the same operating conditions because two flame fronts are approaching each other, increasing the potential of knock.

Shown in figure 4.10, the maximum IMEP for dual spark ignition is 4.0 bar, slightly lower than the maximum IMEP for single spark ignition, 4.3 bar. Blend 1 yields the lowest indicated thermal efficiency and the highest IMEP, which agrees with results from single spark ignition. Unlike single spark ignition, Blend 3 produces the highest indicated thermal efficiency, agreeing with deBoer and Hulet [deBoer and Hulet, 1980]. Blend 3 also produces the lowest IMEP, as expected. Trends in IMEP at other compression ratios produce similar results.

4.2 Understanding Knock Limitations

For a given engine, operation using H_2-O_2-Ar, compared to hydrogen-air, increases the tendency to knock due to the thermodynamic properties of argon. Argon is a monatomic gas and has a lower heat capacity and a higher heat capacity ratio compared to air. This results in higher efficiencies, but causes the end-gas to heat up more rapidly during the combustion processes, increasing the likelihood for engine knock.

The ideal Otto Cycle efficiency, shown in equation 1.1 can also be used to display the tendency for knock to occur at high temperatures inside the cylinder. Assuming isentropic compression with constant specific heat ratio from bottom dead center (BDC), the beginning of the compression process, to top dead center (TDC), just before the combustion event [Heywood, 1988], compression ratio can be written in terms of temperature, much like equation 2.8,

$$\frac{T_{TDC}}{T_{BDC}} = \left(\frac{V_{BDC}}{V_{TDC}}\right)^{\gamma-1}. \tag{4.1}$$

where T_{TDC} is the temperature of the in-cylinder gas at TDC corresponding to the motored (without chemical reactions) temperature, T_{BDC} is the temperature of the gas at BDC, and V_{TDC} and V_{BDC} are the cylinder volumes at TDC and BDC, respectively. Substituting equation 4.1 into equation 1.1 yields a relationship between thermal efficiency for an ideal Otto cycle and in-cylinder temperature,

$$\eta_i = 1 - \frac{T_{BDC}}{T_{TDC}}. \tag{4.2}$$

Looking at equation 4.2, similar efficiencies were expected for combusting Blend 2 of H_2-O_2-Ar and ϕ=0.24 of hydrogen-air engine. However, efficiencies of hydrogen-air at phi=0.24 were much lower, η_i=35%, and hydrogen-air was not as prone to engine-knock. Increasing the efficiency requires either decreasing T_{BDC} or increasing T_{TDC}. Since the end gas temperature is proportional to the motored temperature of the gas at TDC, T_{TDC} is representative of the knock propensity of the engine and limits how much the compression ratio or specific heat ratio can be increased. As a

result, the limitation in T_{TDC} limits the engines efficiency. Although compression ratio or specific heat ratio can increase indicated efficiency, they also increase the possibility of knock. This concept and solutions to preventing knock are investigated using a three-zone model, described in the next section.

4.3 Modeling Hydrogen Combustion

A three-zone model, consisting of a burned zone, unburned zone, and crevices, is used to model combustion in the CFR engine. Because the CFR engine is port fuel injected, the air and fuel are assumed to be perfectly mixed. During the compression stroke, the combustible mixture flows into the crevices. The gas pressure is assumed uniform in all zones such that the mass exchange rate between the zones can be solved simultaneously with energy and species equations [Jensen and Schramm, 2000; Chin and Chen, 2011].

The combustion process is divided into two stages. The first stage is the ignition and initiation of the three zones in combustion space. The second stage is the propagation of the flame front. After a small nucleus of the fuel-air mixture has combusted, the combustion chamber is subdivided into two zones. Following spark ignition, there is a delay period that is modeled empirically [Al-Baghadadi, 2006]. Once combustion has commenced, the mean burned gas front is approximated by a sphere centered on the spark plug location.

The burning rate is modeled as the product of the spherical burning area and the turbulent burning rate [Heywood, 1988]. Heat transfer between the gases in all three zones and the cylinder walls at a rate proportional to the chamber surface area wetted by the gases is modeled using the Woschni correlation [Woschni, 1967]. During the expansion stroke, unburned gases stored in the crevices flow back into the combustion chamber accounting for unburned fuel produced in the experiment. Intake and exhaust flows are modeled using measured valve lifts. The mass flows through the intake and exhaust valves are modeled with a discharge coefficient, C_d, of 0.6. The effect of residual burned gas from previous cycles is included by running the model through eight complete cycles.

4.3.1 Laminar and Turbulent Flame Speed Correlations

The laminar flame speed is fitted to the correlation proposed by Knop et al. [Knop *et al.*, 2008].

$$S_L = S_L^0 \left(\frac{T}{T_0}\right)^{\alpha} \left(\frac{p}{p_0}\right)^{\beta} (1 - 0.87EGR) \text{ (m/s)}, \tag{4.3}$$

where T is the temperature of the unburned (or fresh) gases, T_0 is the reference temperature, p is the local pressure, p_0 is the reference pressure, EGR is the amount of exhaust gas recirculation, and S_L^0, α, and β are fuel-dependent correlation factors.

Fitting the computed flame speeds for Blend 2 (argon concentrations of 86% balanced by a stoichiometric mixture of hydrogen and oxygen), gives correlation factors of,

$$S_L^0 = 8.19 \text{ (m/s) for } \phi=1, \tag{4.4}$$

$$\alpha = 4.42 - 1.23\left(\frac{T}{T_0}\right)^2, \tag{4.5}$$

$$\beta = a - b\left(\frac{p}{p_0}\right)^c, \text{ where} \tag{4.6}$$

$$a = -0.127\left(\frac{T}{T_0}\right)^3 + 0.296\left(\frac{T}{T_0}\right)^2 + 1.13\left(\frac{T}{T_0}\right) - 2.72, \tag{4.7}$$

$$b = 0.121\left(\frac{T}{T_0}\right)^2 - 0.55\left(\frac{T}{T_0}\right) + 0.503, \text{ and} \tag{4.8}$$

$$c = 0.6. \tag{4.9}$$

The turbulent burning rate is computed as [Heywood, 1988]

$$\frac{dm_b}{dt} = \rho_u A_f S_T, \tag{4.10}$$

where m_b is the mass of burned mixture, S_T is the turbulent flame speed, ρ_u is the unburned density and and A_f is the flame surface area.

An empirical model is used for the turbulent flame speed,

$$S_T = S_L f \frac{\rho_u/\rho_b}{(\rho_u/\rho_b - 1)Y_{mb} + 1}, \tag{4.11}$$

where S_L is the laminar flame speed given by equation 4.3, f is the turbulent enhancement factor ($f = 1 + 0.0018 * RPM$), Y_{mb} is the mass fraction of burned mixture, ρ_b is the density of burned mixture.

4.3.2 Model Results and Discussion

Figure 4.11 shows that, when matching motored temperatures at TDC, the three-zone model correlates well with Blend 2 H_2-O_2-Ar data and hydrogen-air. A hydrogen-air mixture of ϕ=0.38, CR=16, and ST=-38°ATDC was chosen to match Blend 2 H_2-O_2-Ar adiabatic flame temperatures.

Methods for reducing knock in the H_2-O_2-Ar engine while maintaining high efficiencies are explored by comparing effects of flame speed and heat capacity on engine-knock (specifically temperature of the unburned gases). To study effects of flame speed on engine-knock, the flame speed H_2-O_2-Ar at two compression ratios, hydrogen-air, and hydrogen air with five times its normal

flame speed are compared. Figure 4.12 shows that using argon as the working fluid results in a rapid increase in laminar flame speed, even more than increasing the flame speed of hydrogen-air five times. This rapid increase in flame speed results in engine-knock.

Comparing the average temperature at BDC, it can be seen from figure 4.13 that the average temperature at BDC are much higher for H_2-O_2-Ar mixtures than hydrogen-air mixtures. Even increasing the flame speed five times of the hydrogen-air mixture did not result in as high of temperatures as H_2-O_2-Ar mixtures.

Figure 4.14 compares unburned gas temperatures. H_2-O_2-Ar at compression ratio of 7 and a spark timing of -8.5° ATDC shows unburned gas temperatures exceeding 1100 K and a pressure rise rate greater than 10 bar (where knock occurs in experimental data). Overall, the unburned gas temperatures of H_2-O_2-Ar mixtures increases much more rapidly than hydrogen-air mixtures. Results also show that increasing laminar flame speed of H2-air five times did not increase unburned gas temperatures as much as increasing the specific heat ratio. This suggests that specific heat ratio of the working fluid contributes more to engine-knock than flame speed.

Although H_2-O_2-Ar mixtures have faster flame speeds and higher unburned gas temperatures than hydrogen-air mixtures, the in-cylinder pressure for the hydrogen-air mixtures is much higher due to operation at higher compression ratios (see figure 4.15. However, H_2-O_2-Ar at a compression ratio of 7 has almost as high of a peak pressure as hydrogen-air at a compression ratio of 16. The increase in peak pressure of H_2-O_2-Ar at a compression ratio of 7 is a result of engine-knock.

4.4 Summary

Overall, these experiments showed that a high thermal efficiency can be obtained by operating an H_2-O_2-Ar, however efficiency above 50% was not achieved due to persistent engine knock at higher compression ratios. Stable operation of the engine for the highest concentration of argon (88%) and compression ratio of 7 was unsuccessful due to the intensity of knock. Knock also limited the progression of spark timing advance and as a result, limited the maximum obtainable thermal efficiency.

Adding a second spark plug slightly increased the indicated efficiency but greatly retarded the spark timing when compared to using a single spark plug. Knock limited the spark advancement for both single and dual spark ignition. The maximum indicated thermal efficiencies achieved using a single and dual spark ignition were about 45% and 46% respectively, which is reasonable for operation at slow engine speeds. Although the dual spark ignition improved efficiency by 1%, the unburned air-fuel mixture between the two approaching flame fronts still auto-ignited.

The three-zone model showed that argon as a working fluid increases in-cylinder temperatures, unburned gas temperatures, and laminar flame speed. When compared to hydrogen-air operating at a higher compression ratio and an increased flame speed, H_2-O_2-Ar still showed higher unburned gas temperatures and BDC temperatures. These results suggest that specific heat ratio affects end

gas temperatures more than increasing flame speed. Therefore, using other noble gases, such as helium, will yield similar knocking limitations. This model accurately represents experimental data and can assist in identifying when engine knock may occur.

Another effect that should be considered in the model is heat transfer rates in the boundary layer close to the wall. The reduced temperatures of hydrogen-air mixtures could be caused by operating at higher compression ratios and in turn pushing a larger portion of the mixture in the boundary layer near the wall, resulting in higher heat transfer rates [Smith, 1994].

Regardless of problems with knock, operation of the H_2-O_2-Ar engine produced higher thermal efficiency than hydrogen-air engines operating under similar conditions [Das, 1991; Verhelst and Sierens, 2007; deBoer and Hulet, 1980]. Possible solutions for reducing the tendency to knock are delaying second spark plug [Migita *et al.*, 2007], using a plasma spark plug [Ikeda *et al.*, 2007a; Ikeda *et al.*, 2007b; Kaneko *et al.*, 2008], cooling the top of the cylinder head since it has the largest surface area, or using a H_2-O_2-Ar diesel engine. If the knock limitation can be overcome by using one of the previously mentioned techniques, then thermal efficiencies of η_i=50% or higher may be attainable.

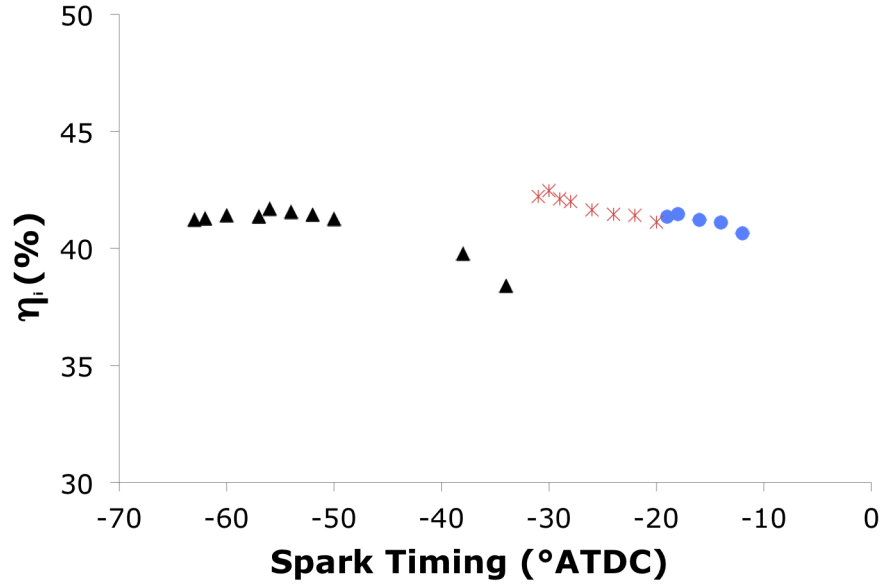

(a) Compression Ratio = 4.5

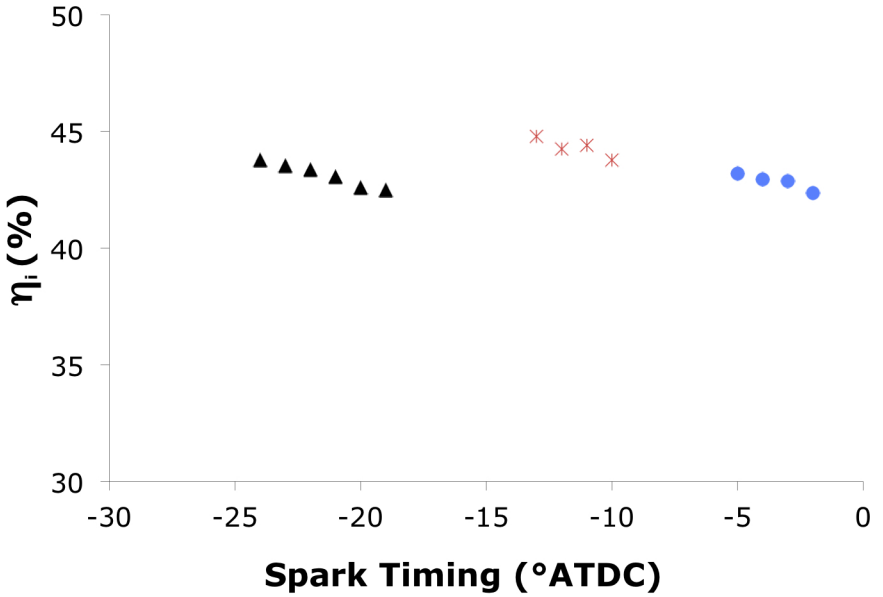

(b) Compression Ratio = 5.5

Figure 4.1: Blend 1 (84% Ar, blue circles), Blend 2 (86% Ar,red stars), and Blend 3 (88% Ar,black triangles). At a compression ratio of 4.5 (a), all blends show a peak indicated thermal efficiency when spark timing is advanced. Increasing the compression ratio to 5.5 (b) did not result in a peak indicated thermal efficiency because knock limited the spark advance.

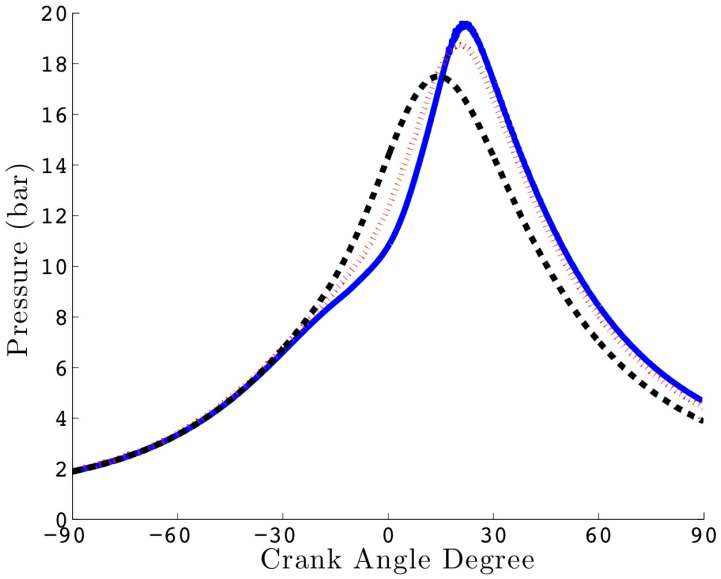

Figure 4.2: In-cylinder pressure trace at compression ratio of 4.5 using single spark ignition for Blend 1(84% Ar, solid blue line), Blend 2 (86% Ar, dotted red line), and Blend 3 (88% Ar, dashed black line) at spark timings of -19°ATDC, -31°ATDC, and -63°ATDC, respectively.

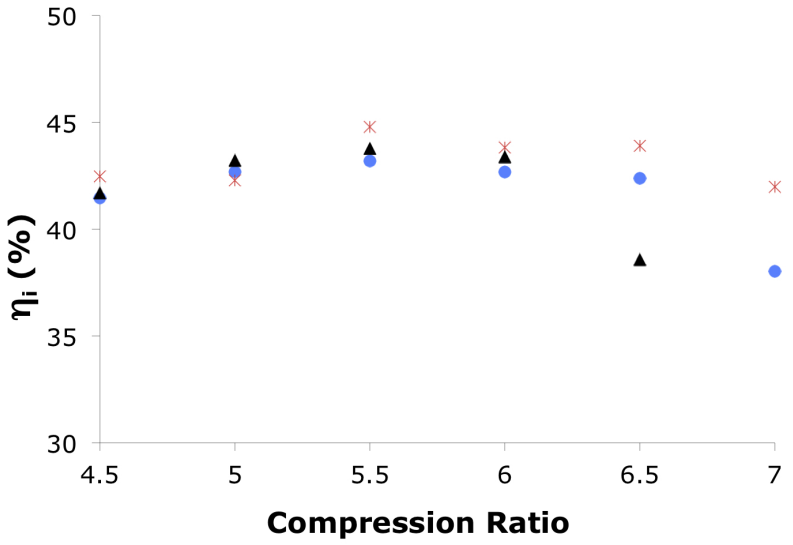

Figure 4.3: Blend 1 (84% Ar, blue circles), Blend 2 (86% Ar, red stars), and Blend 3 (88% Ar, black triangles). The peak thermal efficiency occurs at a compression ratio of 5.5.

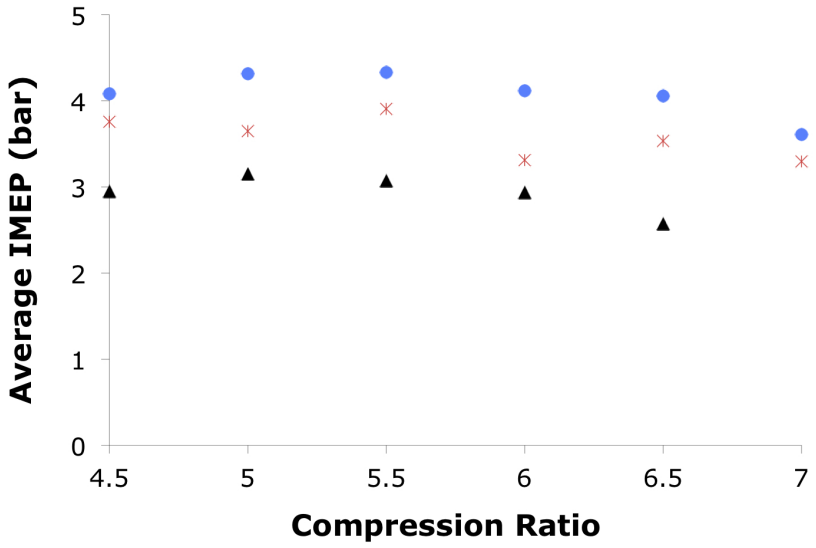

Figure 4.4: Blend 1 (84% Ar, blue circles), Blend 2 (86% Ar, red stars), and Blend 3 (88% Ar, black triangles). IMEP is independent of compression ratio and decreases with increasing concentrations of argon.

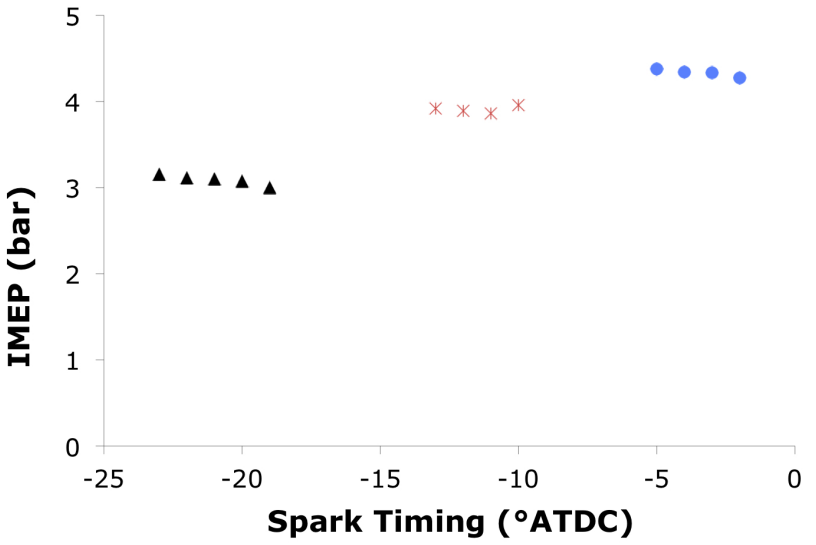

Figure 4.5: Blend 1 (84% Ar, blue circles), Blend 2 (86% Ar, red stars), and Blend 3 (88% Ar, black triangles) at compression ratio = 5.5. IMEP is independent of spark timing.

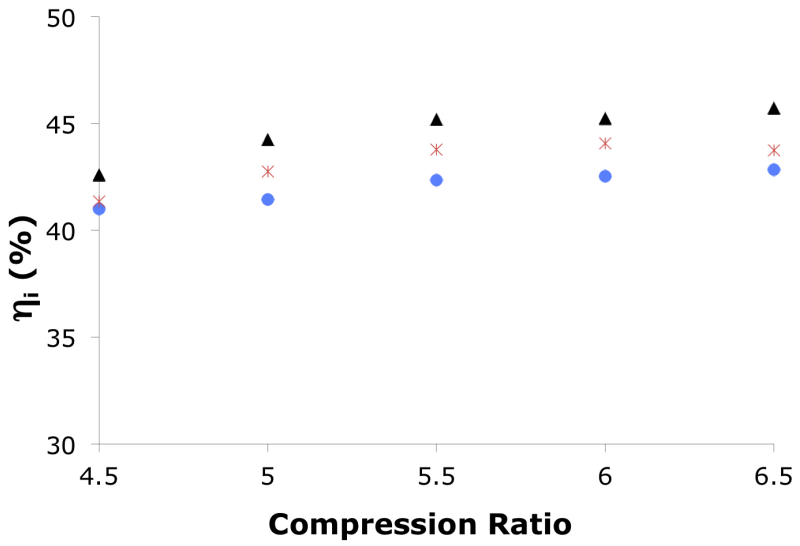

Figure 4.6: Blend 1 (84% Ar, blue circles), Blend 2 (86% Ar, red stars), and Blend 3 (88% Ar, black triangles) for dual spark ignition. The peak thermal efficiency obtained occurred at a compression ratio of 5.5.

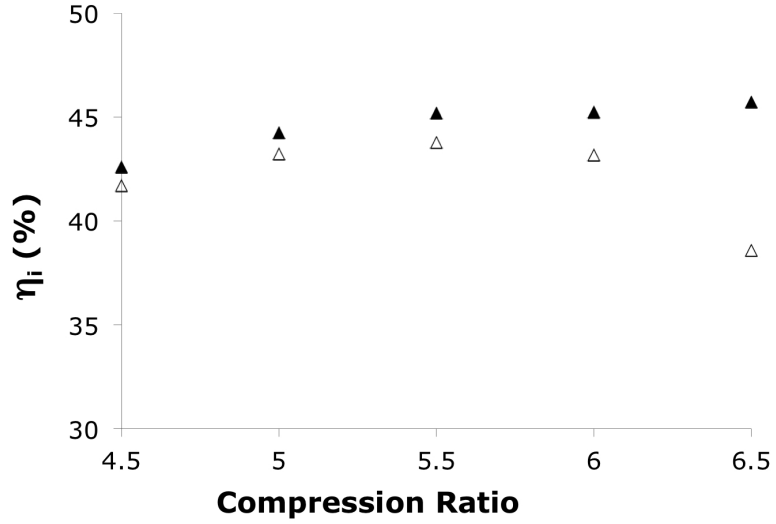

Figure 4.7: Blend 3, 88% Ar, for single (black hollow triangles) and dual (black filled triangles) spark ignition at a spark timing of -6°ATDC. Dual spark ignition had more complete combustion yielding higher indicated thermal efficiencies, but knock limited spark advance.

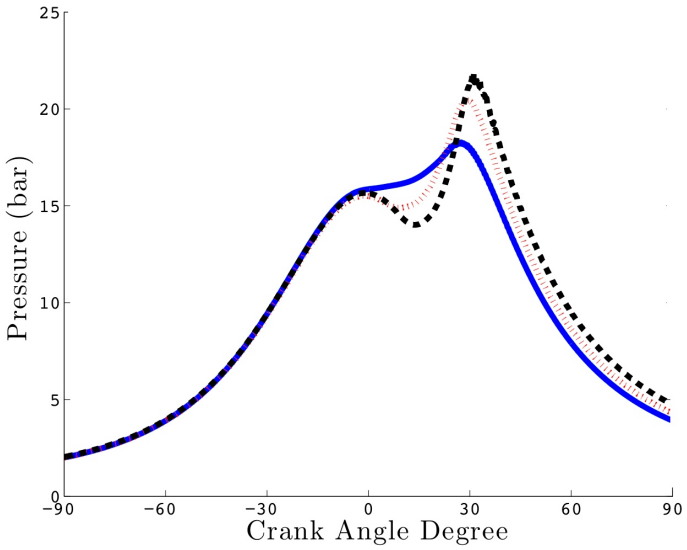

Figure 4.8: Cylinder pressure trace at compression ratio = 6.5 using dual spark ignition for Blend 1 (84% Ar, solid blue line), Blend 2 (86% Ar, dotted red line), and Blend 3 (88% Ar, dashed black line) at spark timings of -6°ATDC, 1°ATDC, and 6°ATDC, respectively.

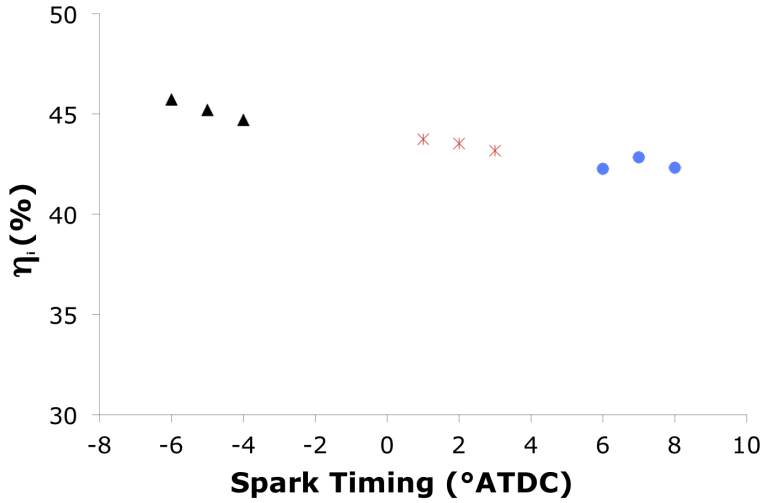

Figure 4.9: Indicated thermal efficiency vs. spark timing using dual spark ignition for Blend 1 (84% Ar, blue circles), Blend 2 (86% Ar, red stars), and Blend 3 (88% Ar, black triangles) at compression ratio = 6.5. Indicated thermal efficiency increases as spark timing is advanced.

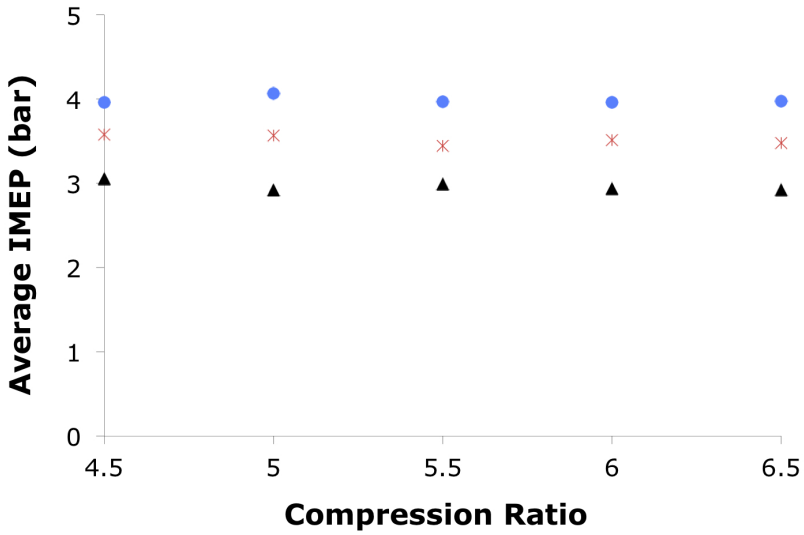

Figure 4.10: IMEP vs. compression ratio using dual spark ignition for Blend 1 (84% Ar, blue circles), Blend 2 (86% Ar, red stars), and Blend 3 (88% Ar, black triangles). For dual spark ignition, IMEP is independent of compression ratio and decreases with increasing argon concentrations.

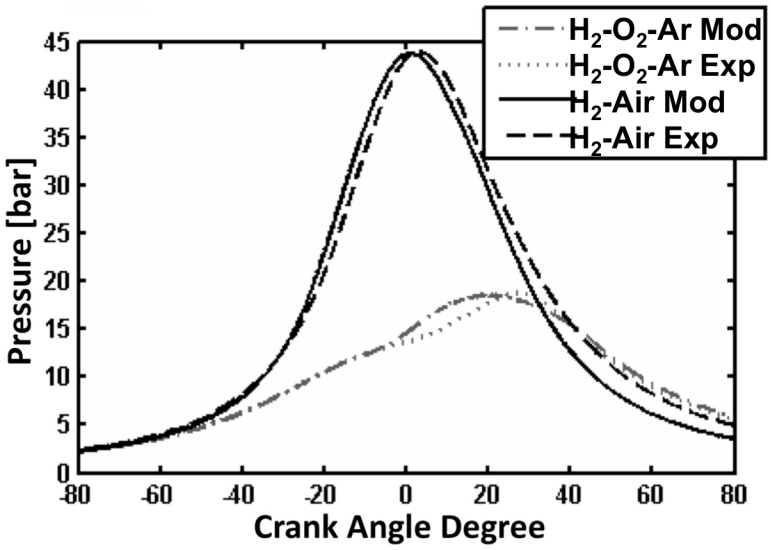

Figure 4.11: In-cylinder pressure predicted by the model matched experimental data for Blend 2 of H_2-O_2-Ar and hydrogen-air at ϕ=0.24.

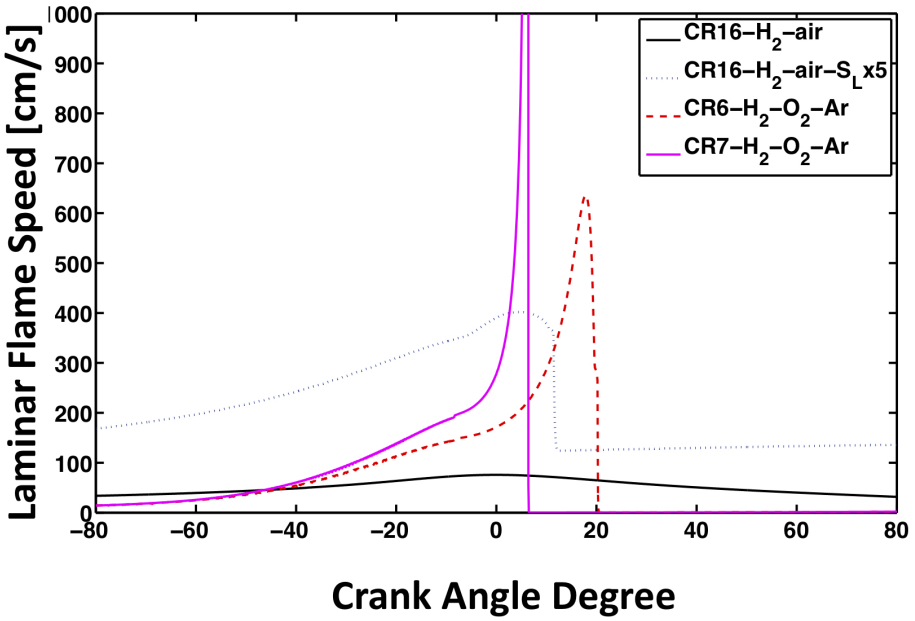

Figure 4.12: Laminar flame speed, S_L of H_2-O_2-Ar mixtures are much faster than hydrogen-air mixtures with five times the flame speed

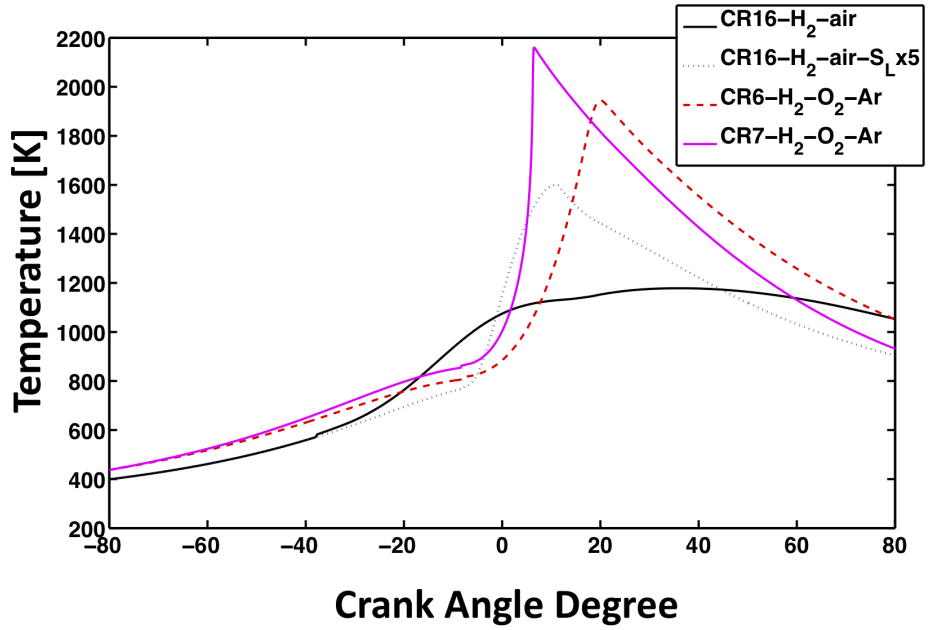

Figure 4.13: Average temperatures at BDC are higher for H_2-O_2-Ar than hydrogen-air

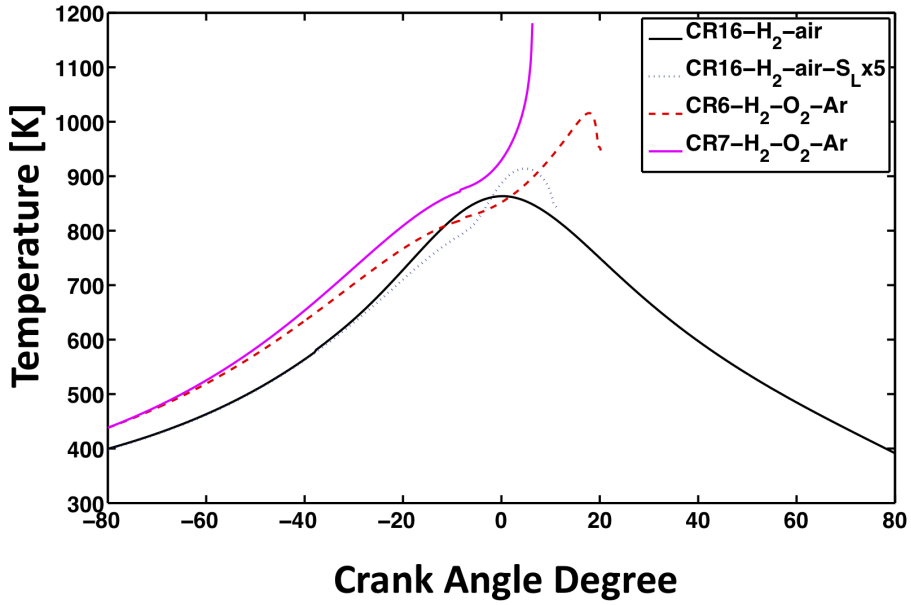

Figure 4.14: Unburned gas temperature of H_2-O_2-Ar mixtures are much higher than hydrogen-air mixtures with five times the flame speed.

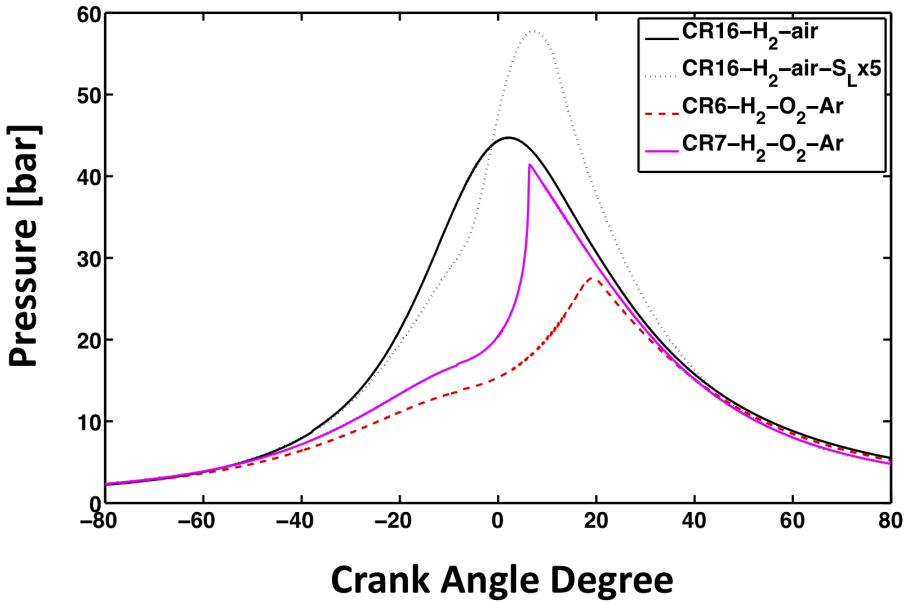

Figure 4.15: In-cylinder pressure of a hydrogen-air mixture with five times its normal flame speed

Chapter 5

Characterizing HCCI Fuels

The purpose of this project is to determine variables for predicting ignition and characterizing fuel performance in HCCI engines. Using these parameters, techniques for creating a standardized HCCI Number, similar to octane number and cetane number, is investigated. In this chapter, previous methods for predicting auto-ignition are described, correlations between existing methods and ignition in HCCI engines, using experimental results, are investigated, and effects of varying parameters on HCCI ignition, using experimental results, are presented. Results using a three-zone model to further understand the relationship between fuel chemistry and ignition in HCCI engines are also provided.

5.1 Existing Methods for Predicting Auto-ignition

5.1.1 Octane Number

In spark-ignited (HCSI) engines , the octane number is used to determine the anti-knock qualities of a fuel. In the United States, the octane number is the average number from two standardized tests, the research octane number (RON) and the motor octane number (MON) [ASTM Standard D2699-11, 2011; ASTM D2700-11, 2011]. RON characterizes the fuel's knocking resistance at wide open throttle conditions and low speeds, while MON characterizes the fuel's knocking resistance at wide open throttle and high speeds, simulating anti-knock qualities under load. Both RON and MON test are conducted using a Cooperative Fuel Research (CFR F1/F2) engine, with variable compression ratio, fitted with a knock meter for measuring knock intensity. Primary reference fuels (PRF), mixtures of n-heptane (RON=MON=0) and isooctane (RON=MON=100), are used to create calibration curves of changes in knock intensity with compression ratio. These calibration curves are used to calculate the RON and MON of fuels [ASTM Standard D2699-11, 2011; ASTM D2700-11, 2011] and the octane number, or Anti-Knock Index (AKI) is calculated by,

$$ON = \frac{RON + MON}{2}. \tag{5.1}$$

The octane number shown in equation 5.1 is the value labeled on gasoline pumps in the united states.

5.1.2 Cetane Number

In Diesel (DICI) engines, fuels should be more prone to auto-ignition and are typically less volatile than fuels designed for spark-ignited engines. Combustion quality of fuels for Diesel engines is determined by the cetane number. Two methods are commonly used to determine a fuel's cetane number. The first method involves a Diesel CFR engine (CFR F5) and reference fuels consisting of normal cetane (n-hexadecane with cetane number=100), and heptamethylnonane (assigned cetane number of 15). The cetane number is given by,

$$CN = x + 0.15(100 - x), \tag{5.2}$$

where x is the precent volume of normal cetane [ASTM Standard D613-10a, 2010]. The second method for measuring cetane number is using an ignition quality tester (IQT) [ASTM D6890-11, 2011]. This method determines the derived cetane number (DCN),

$$DCN = 83.99(ID - 1.512)^{-0.658} + 3.547, \tag{5.3}$$

where ID is the ignition delay (in ms) measured from the start of ignition to the point of significant heat release and is the average of 32 firings. This method provides better repeatability for determining cetane number, but has best accuracy for an ignition delay range of 3.3 - 6.4 ms.

According to Kalghatgi [Kalghatgi, 2005], the relationship between cetane number and RON, assuming n-heptane has a cetane number of 54.6, is,

$$CN = 54.6 - 0.42RON. \tag{5.4}$$

5.1.3 Octane Index

Using a linear regression, Kalghatgi [Zhao *et al.*, 2003] developed an octane index accounting for temperature and pressure variation in the engine to better characterize knocking behavior of practical fuels. The octane index is defined as,

$$OI = (1 - K)RON + (K)MON, \tag{5.5}$$

where K is a constant dependent on the engines operating conditions and can be determined by,

$$\begin{aligned} K &= 0.0426(T_{comp,15bar}) - 35.2 \text{ if } T_{comp,15bar} > 825\text{K and} && (5.6)\\ &= 0.0056(T_{comp,15bar}) - 4.68 \text{ if } T_{comp,15bar} < 825\text{K}, && (5.7) \end{aligned}$$

where $T_{comp,15bar}$ is the in-cylinder temperature, in kelvin, when the in-cylinder pressure, during compression, reaches 15 bar. For HCCI operation, $T_{comp,15bar}$ is typically below 825K [Shibata and

Urushihara, 2007]. For the UC Berkeley CFR engine, $T_{comp,15bar}$ is estimated to be 780K, which yields a K factor of -0.312.

Kalghatgi [Kalghatgi, 2005; Zhao *et al.*, 2003] used a similar technique to derive a relationship between OI and CA50,

$$\begin{aligned} CA50 &= aRON + bMON + c \qquad (5.8) \\ &\quad \text{or in terms of } OI \text{ and } K \\ &= c + (a+b)OI \qquad (5.9) \end{aligned}$$

However, use of the Octane Index is limited because the constant K is engine specific, meaning for each engine and each operating condition, a new K must be calculated. Therefore, an alternative method may be more suitable for use as a standard when predicting auto-ignition in HCCI engines.

5.1.4 HCCI Index

Shibata and Urushihara [Shibata and Urushihara, 2007], took Kalghatgi's work a step further and developed several indexing systems for predicting ignition in HCCI engines using fuel composition and MON. They define an absolute HCCI index as follows,

$$\text{HCCI Index (abs)} = mMON + a(nP) + b(iP) + c(O) + d(A) + e(OX) + Y, \qquad (5.10)$$

where (nP) is the precent n-paraffins by volume, (iP) is the precent iso-paraffins by volume, (O) is the precent olefins and cycloalkanes by volume, (A) is the precent aromatics by volume, (OX) is the precent oxygenates by volume, and m, a, b, c, d, e, and Y are temperature dependent constants shown in table 5.1 [Shibata and Urushihara, 2007].

They also propose a relative HCCI index based on MON, which is similar to equation 5.10 but recalculates table 5.1 such that m=1 and Y=0. His relative index is,

$$\text{HCCI Index (relative)} = MON + \alpha(nP) + \beta(iP) + \gamma(O) + \delta(A) + \epsilon(OX), \qquad (5.11)$$

where α, β, γ, δ, and ϵ are temperature dependent constants found in table 5.2.

Because many oil refineries use RON measurements instead of MON, they also created a RON based HCCI index [Shibata and Urushihara, 2007; Shibata and Urushihara, 2009],

$$\text{HCCI Index (abs)} = rRON + a'(nP) + b'(iP) + c'(O) + d'(A) + e'(OX) + Y', \qquad (5.12)$$

where r, a', b',c',d', e', and Y' are temperature dependent constants shown in table 5.3.

Table 5.1: Coefficient values for Shibata and Urushihara's absolute HCCI index using MON at $T_{comp,15bar}$ = 780K [Shibata and Urushihara, 2007].

m	0.763
a	-0.356
b	-0.315
c	-0.185
d	-0.193
e (for Ethanol)	0.062
Y	-36.43

Table 5.2: Coefficient values for Shibata and Urushihara's relative HCCI index using MON at $T_{comp,15bar}$ = 780K [Shibata and Urushihara, 2007].

α	-0.487
β	-0.380
γ	-0.246
δ	-0.222
ϵ (for Ethanol)	0.049

5.2 Experimental Results and Discussion of Existing Methods for Predicting Auto-ignition

For the following experiments, a variable compression ratio, single cylinder cooperative fuel research (CFR) engine, described in chapter 3, operating as an HCCI engine was used for studying the development of an HCCI index. This engine is an ideal standardized test engine because of its robust design and variable compression ratio [Dec, 2009; García *et al.*, 2009]. Previous research [Liu *et al.*, 2009] also suggests that engines operating with a higher intake temperatures and lower RPM will auto-ignite a wider range (low and high octane number) of fuels. In addition, differences between auto-ignition characteristics are more visible at atmospheric intake pressures than boosted intake pressures [Liu *et al.*, 2008; Yao *et al.*, 2009]. Therefore, most experiments were conducted at 600 RPM with an intake temperature of 150°C and an intake pressure of 1.035 bar.

5.2.1 CA50, Octane Number, and Cetane Number

Plots of CA50 against compression ratio were generated to compare ignition timing of each fuel. These plots were also created with the intention of resembling RON and MON calibration curves. Figure 5.1 shows an almost linear relationship between CA50 and compression ratio and suggest fuels with ignitions sensitive to changes in compression ratio will have steeper slopes. Autoignition of fuels, however, does not correspond to their RON, MON, or octane number (ON). This is demonstrated in figure 5.1, where the six fuels all have a RON of 70 (ON≈70) but auto-ignite at

Table 5.3: Coefficient values for Shibata and Urushihara's and absolute HCCI index using RON at $T_{comp,15bar}$ = 780K [Shibata and Urushihara, 2007].

r	0.523
a'	-0.244
b'	-0.187
c'	-0.176
d'	-0.109
e' (for Ethanol)	-0.054
Y'	-32.109

different compression ratios.

Investigating the relationship between octane number and CA50 further, Figure 5.2 shows the fuels with a RON of 70 (or RON 70 fuels) plotted with other primary reference fuels (PRF) having lower and higher RON and ON. The results show most of the RON 70 fuels (PRF70, S70, TRF70, and GasB1) are bracketed by PRF60 and PRF75. However, E-PRF70 and Gas2 are bracketed by PRF75 and PRF85. Therefore, octane number alone may not be sufficient for characterizing HCCI fuels and primary reference fuels are not a suitable choice for reference fuels in a HCCI index.

Similar to previous research [Yao *et al.*, 2009], experimental results show that cetane number alone is not sufficient for predicting auto-ignition in HCCI engines. Figure 5.3 shows PRF70 and GasB1 with the same ignition starting compression ratio, but PRF70 has a higher cetane number than GasB1, suggesting PRF70 should auto-ignite first. Also, cetane number predicts that TRF70 and GasB1 should have similar auto-ignition points, but the experiments show TRF70 needing a higher compression ratio for auto-ignition.

5.2.2 CA50 and Octane Index

Using a single-zone model, discussed later, and matching it to experimental, motoring pressure traces, the in-cylinder temperature during compression at an in-cylinder pressure of 15 bar ($T_{comp,15bar}$) was estimated to be 780K. Putting $T_{comp,15bar}$=780K into equation 5.7 yields a K factor of -0.312 for the UC Berkeley CFR engine at 600 RPM and an intake temperature of 150°C.

Figure 5.4 shows an almost linear trend between the compression ratio at the onset of stable HCCI operation and the octane index. However, like octane number, the octane index is not sufficient for predicting auto-ignition of fuels with the similar octane index values in HCCI engines. For example, the octane index suggests that S70, E-PRF70, and Gas2 should auto-ignite at the same compression ratio, but the experimental results show that E-PRF70 and Gas2 require higher compression ratios.

The results in figure 5.4 show that the octane index does not predict auto-ignition of fuels containing ethanol, agreeing with previous research [Yao *et al.*, 2009]. These results also suggest

that the octane index may not predict auto-ignition of fuels containing toluene.

5.2.3 CA50 and HCCI Index

The relative HCCI index created by Shibata and Urushihara [Shibata and Urushihara, 2007] was calculated using equation 5.11 for fuels with known composition and MON. This information was provided by Chevron, since the exact composition was unknown to the author. Estimates of MON and RON were made for GasB1, GasB5, and GasB8 when calculating HCCI Index values. Figure 5.5 shows almost a linear correlation between the compression ratio at the onset of stable HCCI operation and PRF fuels. However, like the octane index, the HCCI index does not accurately predict ignition of fuels containing ethanol, toluene, or other aromatics.

Figure 5.6 shows no correlation between the relative HCCI index and the compression ratio at the onset of stable HCCI operation for gasoline fuels with different pure compounds added (additives). The HCCI index assumes that all aromatics will behave similarly when added to a fuel. Based on a lower relative HCCI index value, GasB4 should ignite before GasB9, however, the experimental results in figure 5.6 show GasB4 requiring one full compression ratio higher than Gas B9 to auto-ignite.

The HCCI index does not include the amount of naphthenes (because of permutations and combinations rule in statistic analysis) [Shibata and Urushihara, 2007], which also results in some error. GasB6 and GasB7 contain two different naphthenes and the experiments showed that the same compression ratio was required to auto-ignite the fuels, but the HCCI index predicted Gas B7 should auto-ignite slightly before GasB6.

Figure 5.7 shows the relative HCCI index for all the fuels with known composition and known MON. The correlation between relative HCCI index and the compression ratio at the onset of stable operation is almost linear ($R^2 = 0.79$), but the HCCI index still has trouble with accurately predicting auto-ignition of fuels containing ethanol or different aromatics.

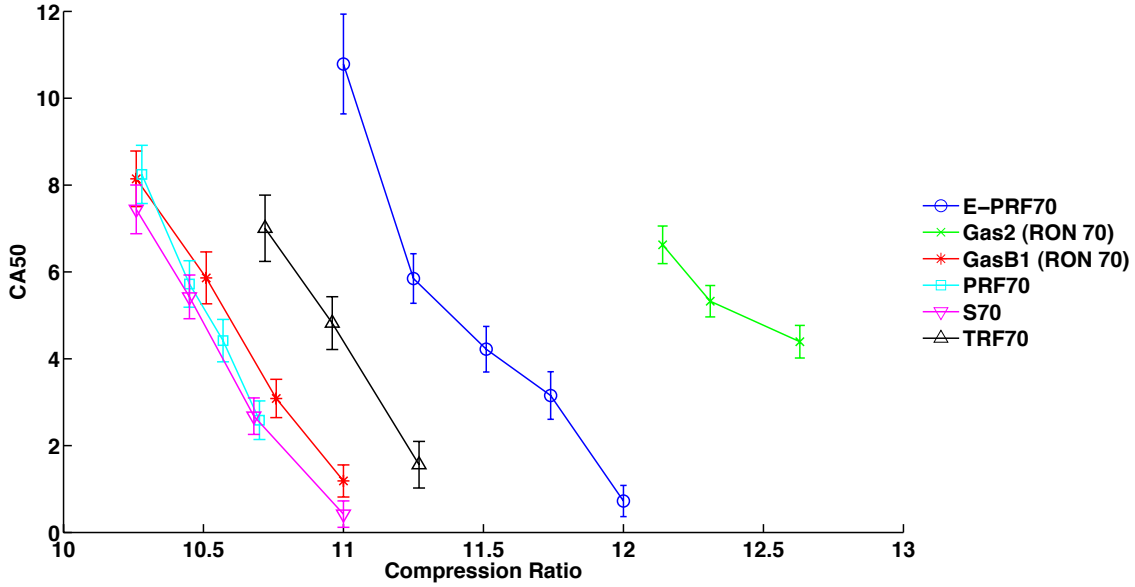

Figure 5.1: Fuels with a RON of 70 require different compression ratios for auto-ignition in HCCI engines.

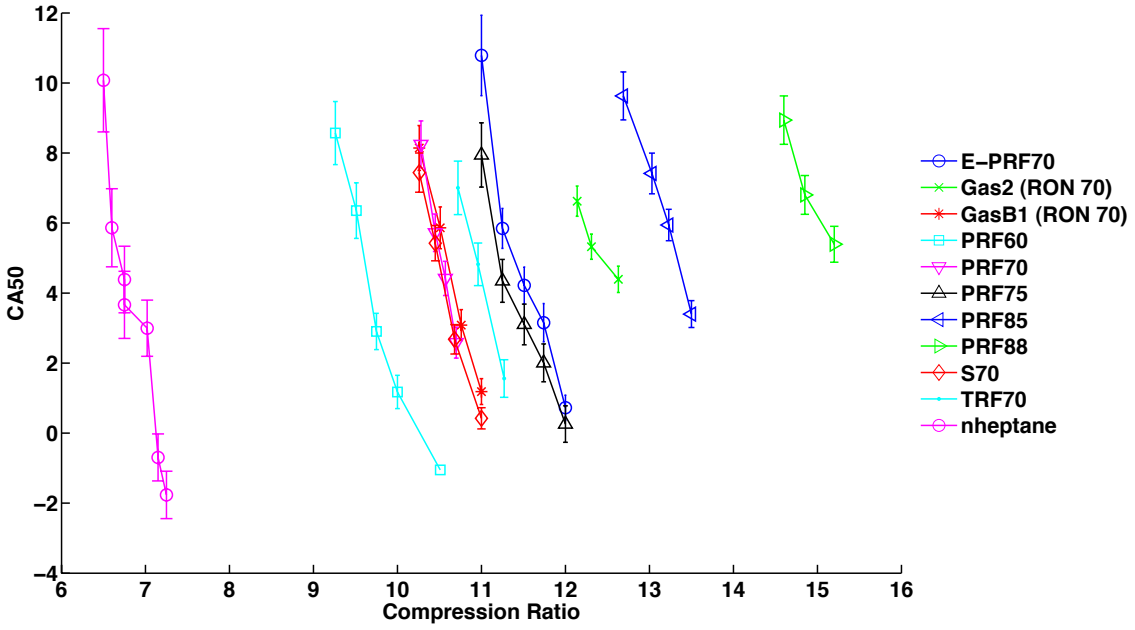

Figure 5.2: Octane number does not accurately predict ignition of fuels in HCCI engines.

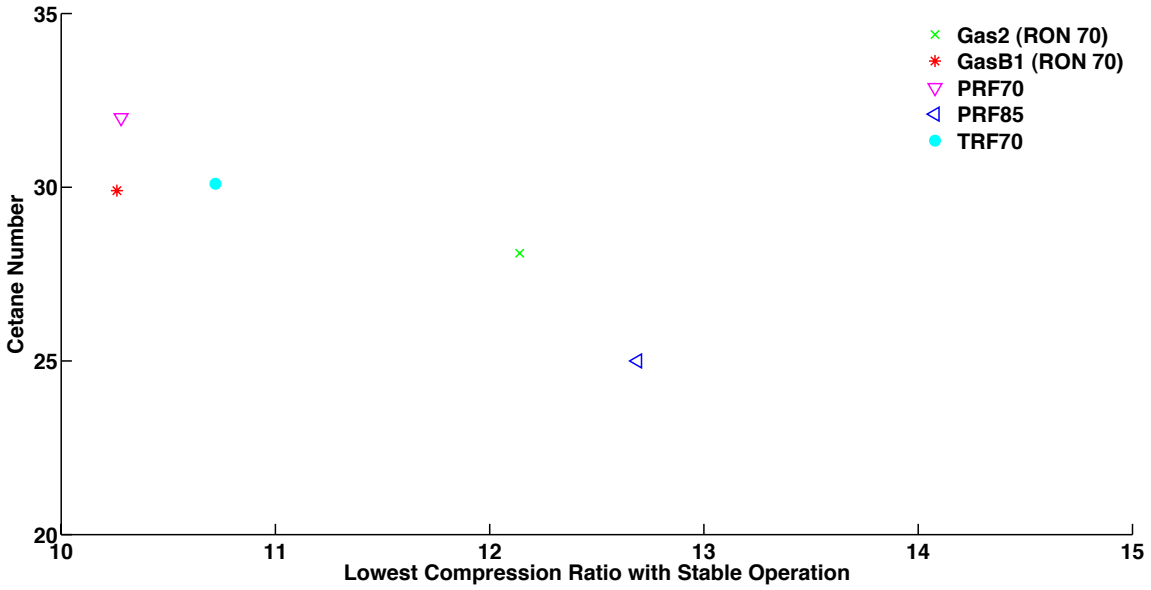

Figure 5.3: Cetane number does not accurately predict ignition of fuels in HCCI engines

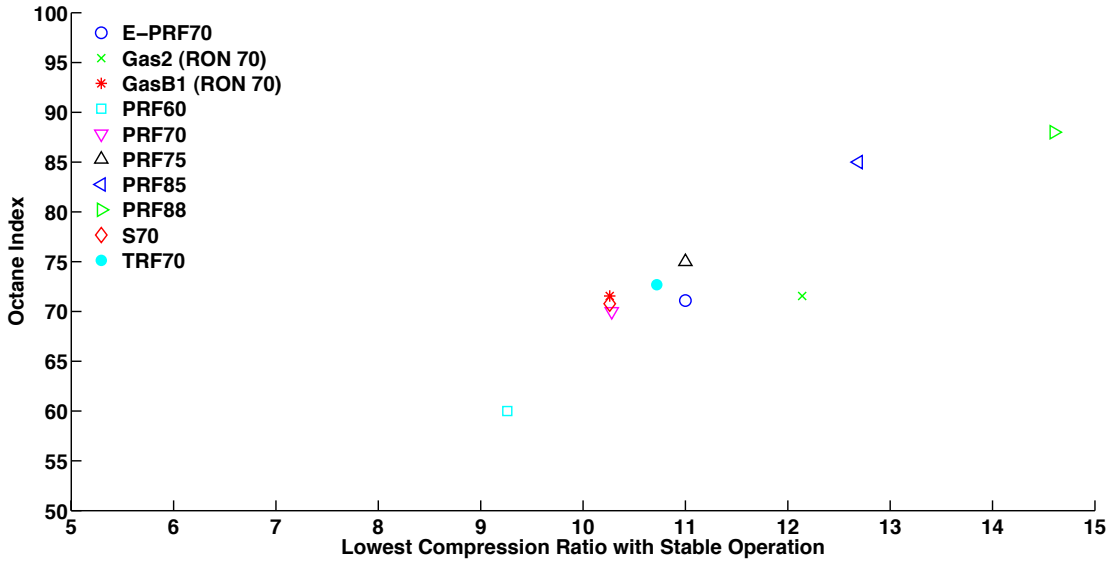

Figure 5.4: Octane index shows an almost linear trend with compression ratio for PRF blends. However, the octane index not accurately predict auto-ignition of fuels containing ethanol, toluene, or a gasoline blendstock.

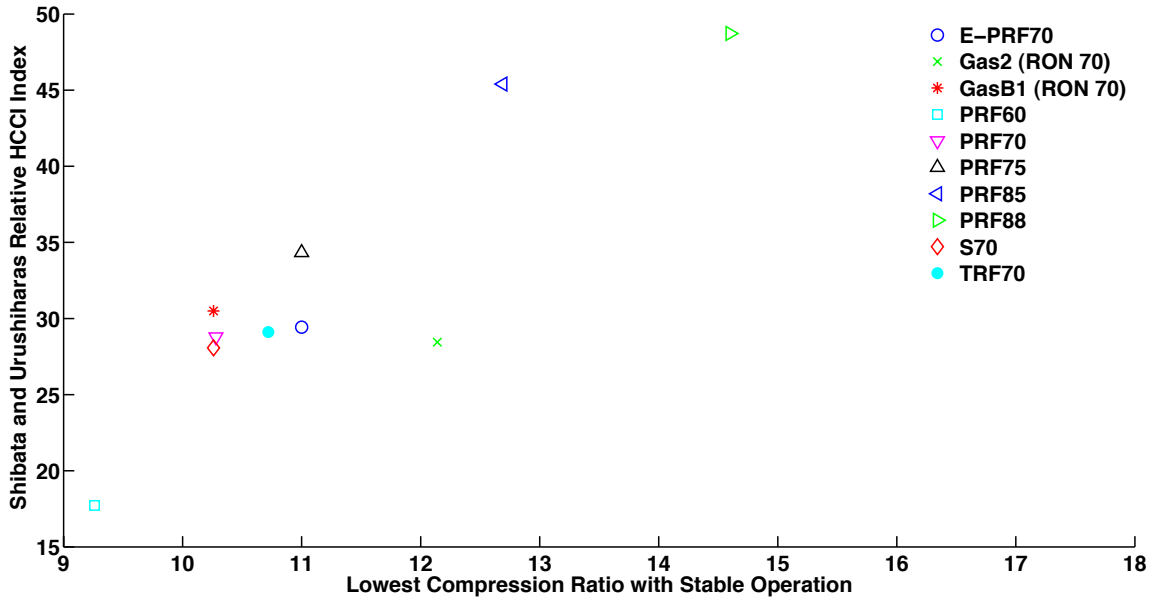

Figure 5.5: HCCI index correlates well with PRF fuels but does not accurately predict ignition of fuels containing ethanol, toluene, or gasoline blendstocks.

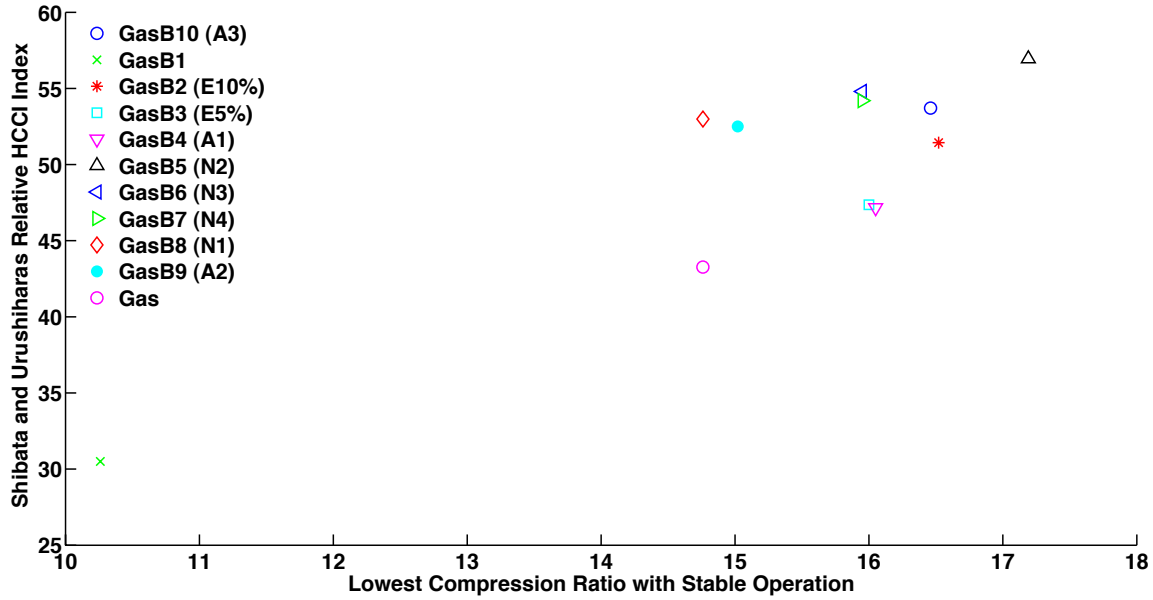

Figure 5.6: HCCI index does not accurately predict ignition for gasoline blendstocks with different aromatic compounds.

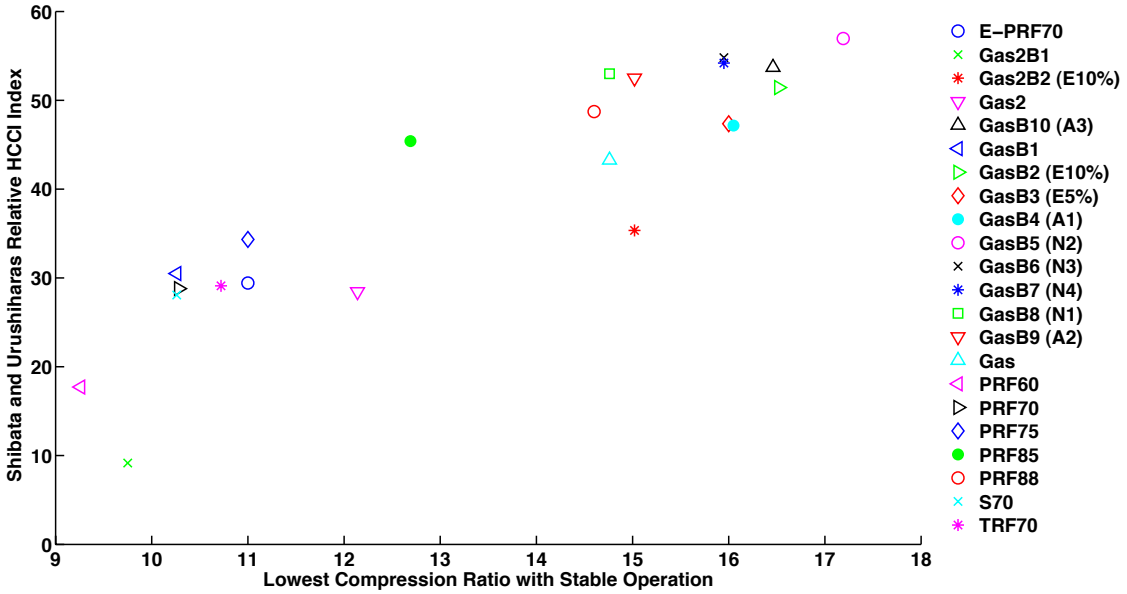

Figure 5.7: HCCI index is almost linear with the compression ratio for the PRF's at the onset of stable operation ($R^2 = 0.79$), but still has trouble predicting ignition of fuels with ethanol and different aromatics.

5.3 Experimental Results and Discussion of Other Trends Affecting Auto-Ignition

Correlations between CA50 and compression ratio are almost linear, suggesting fuels with auto-ignitions sensitive to changes in compression ratio will have steeper slopes, As shown in figure 5.8. A closer view fuels grouped together are shown in figures 5.9 and 5.10. Similar to a calibration curve for octane testing, fuels with similar auto-ignition characteristics are grouped together. Shown in figure 5.11, PRF70 and S70 are grouped together and have similar auto-ignition characteristics. Although PRF70 and S70 have similar RON, MON, and octane numbers (≈70), auto-ignition characteristics do not always correspond to the fuel's RON, MON, or octane number, as shown by TRF 70 and E-PRF70 in figure 5.11. Also, primary reference fuels are not suitable for predicting auto-ignition of fuels from commercial refinery blendstocks in HCCI engines (see figures 5.9 and 5.10). Therefore, new, more appropriate reference fuels need to be identified and a second parameter, aside from the relationship between CA50 and compression ratio, may be required for predicting and characterizing auto-ignition in HCCI engines.

5.3.1 Identifying Reference Fuels

Figure 5.12 shows the effect of different additives on two base fuels. Fuels with the same color and symbol have the same additive. The black squares are the original fuel. GasB2 and Gas2B2

are Gas and Gas2, respectively, blended with the same amount of ethanol by volume. From these results, addition of ethanol has a larger effect on auto-ignition for Gas2 than Gas. A possible explanation is Gas2 shows low temperature heat release and Gas shows little to no low temperature heat release, suggesting ethanol is a low temperature heat release inhibitor, as shown by previous research [Shibata *et al.*, 2005; Yao *et al.*, 2009].

GasB8 and Gas2B3 have the same naphthene added by volume to Gas and Gas2, respectively. It can be seen from figure 5.12 that this naphthene advanced ignition of Gas but delayed ignition of Gas2. Adding n-heptane to Gas and Gas2 (GasB1 and Gas2B1, respectively), however, delayed ignition of Gas more than Gas2. Because different additives affect each fuel differently, identifying one set of reference fuels could be difficult. Although using the trend between CA50 and compression ratio provides some information on predicting auto-ignition in HCCI engines, creating an standard HCCI number, like octane number, may require two parameters.

5.3.2 Relationships between Heat Release and Auto-ignition

A second parameter for predicting auto-ignition in HCCI engines could be the relationship between low temperature heat release and high temperature heat release, as suggested by Kalghatgi et al. and Shibata el al. [Kalghatgi, 2005; Shibata and Urushihara, 2007].

Correlations between auto-ignition and heat release were first investigated by normalizing the low temperature heat release (LTHR) by the high temperature heat release (HTHR) of each fuel. Figure 5.13 shows the ratio of LTHR to HTHR remaining almost constant with CA50. N-heptane has the largest ratio of LTHR to HTHR and almost all the octane 70 fuels are grouped together, except the commercial gasoline blend, Gas2. Another interesting result is almost all the octane 70 fuels are bracketed by PRF60 and PRF 75, again except Gas2. Also, PRF85 and PRF88 have very similar LTHR to HTHR ratios. Most of the fuels requiring higher compression ratios for auto-ignition and stable operation exhibited no visible low temperature heat release, resulting in a LTHR to HTHR ratio of zero.

Similar to CA50, the ratio of LTHR to HTHR remains almost constant with changes in compression ratio, as shown in Figure 5.14. Also, the ratio of LTHR to HTHR decreases almost linearly between fuels as compression ratio increases from 6 to 15. To investigate this further, figure 5.15 shows the linear relationship (R^2=0.84 for fuels with compression ratios between 6 and 15) between the ratio of LTHR to HTHR and compression ratio at the onset of stable HCCI operation. For almost all fuels requiring a compression ratio above 15 to achieve auto-ignition, no visible low temperature heat release is present. The exception is PRF88, which has almost the same ratio of LTHR to HTHR as PRF85.

Trends between auto-ignition and heat release are also investigated using the delay (or Gap) between LTHR and HTHR. The delay between LTHR and HTHR was calculated using by subtracting the crank angle degree where LTHR reached a maximum from the crank angle degree where HTHR reached a maximum, as shown in figure 5.16. Figure 5.17 shows the Gap increasing linearly

with CA50 for octane 70 fuels. The figure also shows the gasoline fuels grouped separately from the reference fuel blends (blends composed of n-heptane, isooctane, toluene, and/or ethanol).

Adding all the reference fuel blends, shown in figure 5.18, still shows the gasoline fuels separated from the reference fuels and shows n-heptane with the smallest Gap. Figure 5.19 shows the Gap for all the fuels with low temperature heat release and again groups the reference fuels and the gasoline fuels separately, keeping n-heptane alone with the smallest gap. These trends give insight on how LTHR affects gasoline and reference fuels differently, even though both fuels may have the same octane number.

5.3.3 Effects of Intake Temperature on Heat Release and Auto-ignition

Figure 5.20 shows the the heat release rate of PRF70 at intake temperatures of 69°C, 115°C, and 150°C with the same CA50 and equivalence ratio. The heat release rate was determined using the difference between the combustion heat release and the motoring heat release, removing heat transfer effects from the engine. As intake temperature increases, the amount of LTHR decreases while the amount of HTHR increases, agreeing with previous research [Dec, 2009; Yao *et al.*, 2009]. As explained in Chapter 2, the forward reaction of reaction (R11) is governed by pressure, while the reverse reaction is governed by temperature. Increasing the intake temperature, and at the same time lowering the compression ratio to maintain a constant CA50, favors the reverse reaction of reaction (R11). This results in the decrease in LTHR shown in figure 5.20. Decreasing the intake temperature, and increasing the compression ratio to maintain a constant CA50, favors the forward reaction of reaction (R11), resulting in an increase in LTHR.

Aside from decreasing LTHR, increasing the intake temperature also increases the Gap between HTHR and LTHR, advancing LTHR. One possible explanation is when the intake temperature decreases, and the compression ratio is increased to maintain the same CA50, the start of low temperature combustion is delayed due to the drop in temperature, as shown in figure 5.20. Also, the pressure during the transition from low temperature combustion to high temperature combustion is increased, increasing the chemical activity and resulting in a shorter duration between LTHR and HTHR. Later in this chapter, a model is used to explore this theory further.

Figure 5.21 shows the total amount of heat released at each intake temperature using PRF70 is almost the same, ≈410 J. The heat release increases slightly at lower intake temperatures because the density of air in the cylinder is increasing. As a result, the amount of fuel must also increase slightly to maintain the same equivalence ratio at the lower intake temperature. Similar trends between LTHR and HTHR were found when testing a gasoline based fuel at different intake temperatures (not shown).

5.3.4 Characterizing Fuel Stability

COV IMEP is often used to determine combustion stability of fuels in gasoline engines. In spark ignited engines, a COV IMEP greater than 10% indicates vehicle drivability problems [Heywood, 1988]. As revealed in figure 5.22, HCCI engines tend to have lower COV IMEP due to less cycle-to-cycle variation. For all fuels, COV IMEP is less than 3%. As CA50 increases, on average the COV IMEP increases, as expected with delayed ignition, which leads to engine instabilities. Gas and GasB2 generally had the highest COV IMEP. Figure 5.23 shows that fuels with a RON of 70 (most having an ON of 70) have some of the lowest COV IMEP, agreeing with previous research [Yao *et al.*, 2009].

Although COV IMEP is very low for all the fuels tested in the CFR, a distinct difference between fuels or fuel groups is not obvious from figure 5.22 and some of the fuels proved to be more unstable than others. For example, Gas and TRF70 show similar COV IMEP in figure 5.22; however, during operation, TRF70 was easier to auto-ignite and auto-ignited more consistently than Gas. The CFR shows that COV IMEP is not a suitable parameter for defining fuel stability, but operation of these fuels in a different HCCI engine may yield different results [Kalghatgi and Head, 2006].

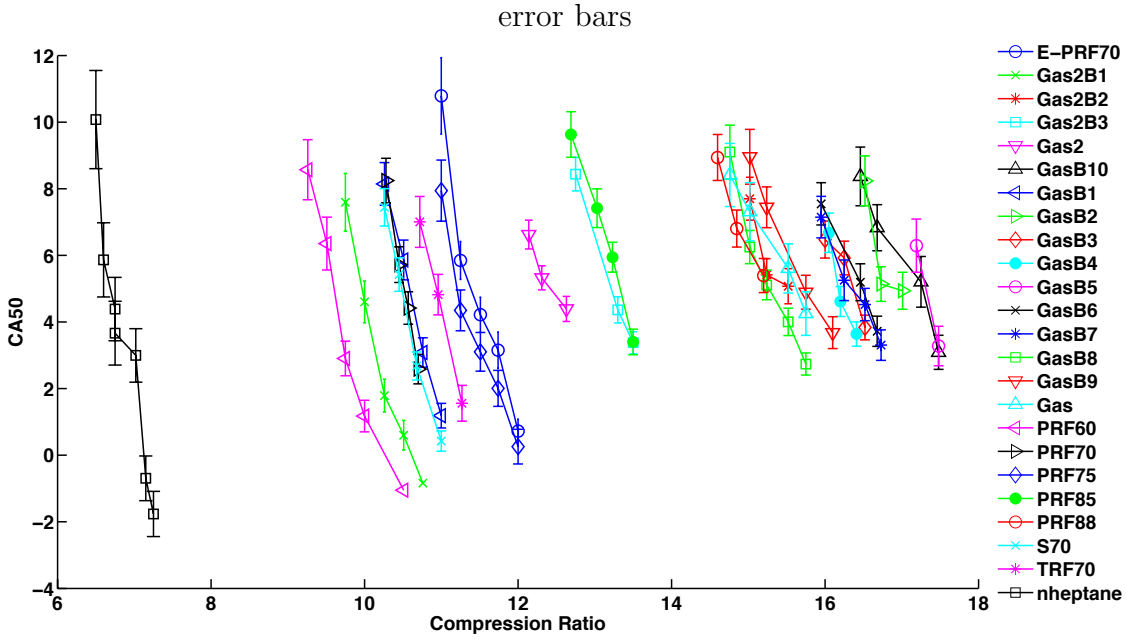

Figure 5.8: Auto-ignition trends with varying compression ratio for all fuels tested including error bars.

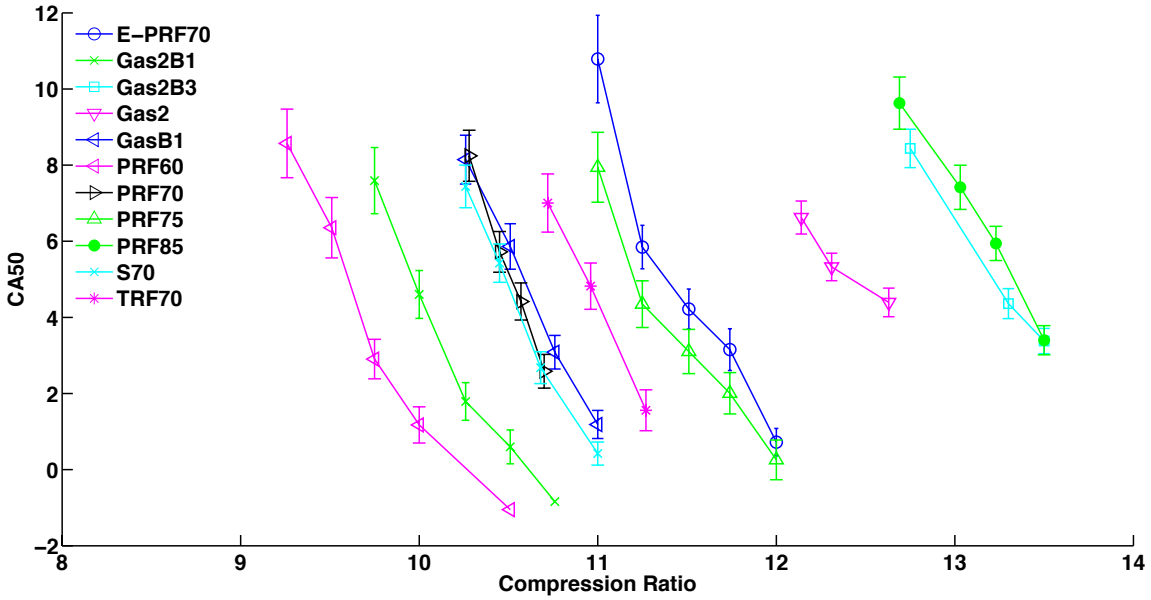

Figure 5.9: Autoignition trends of fuels with stable HCCI operation at compression ratios between 8 and 14.

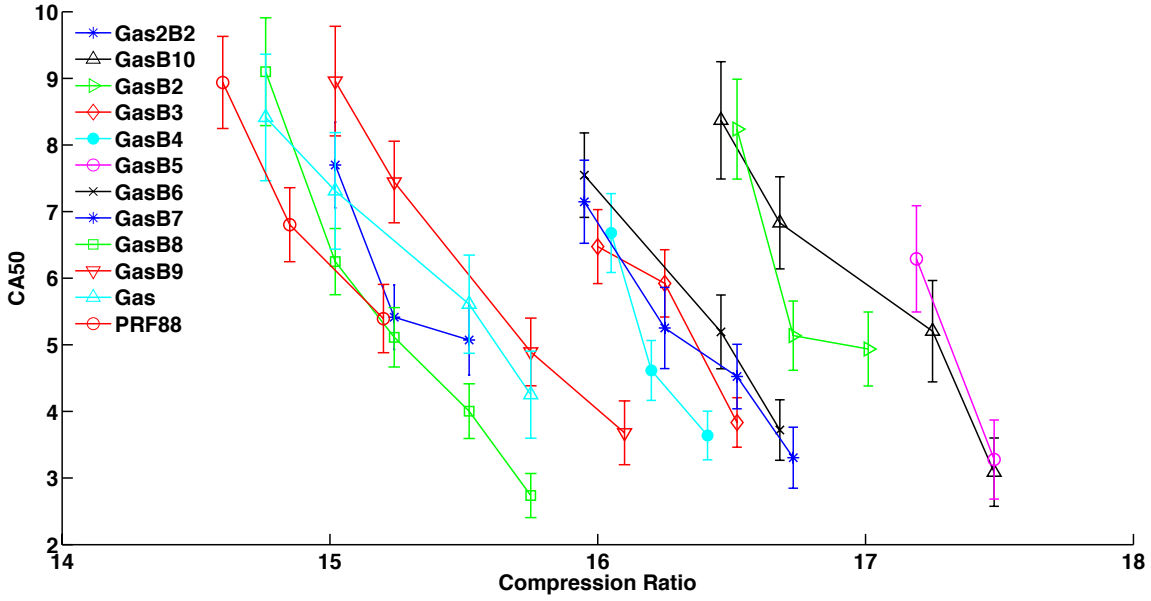

Figure 5.10: Autoignition trends of fuels with stable HCCI operation at compression ratios between 14 and 18.

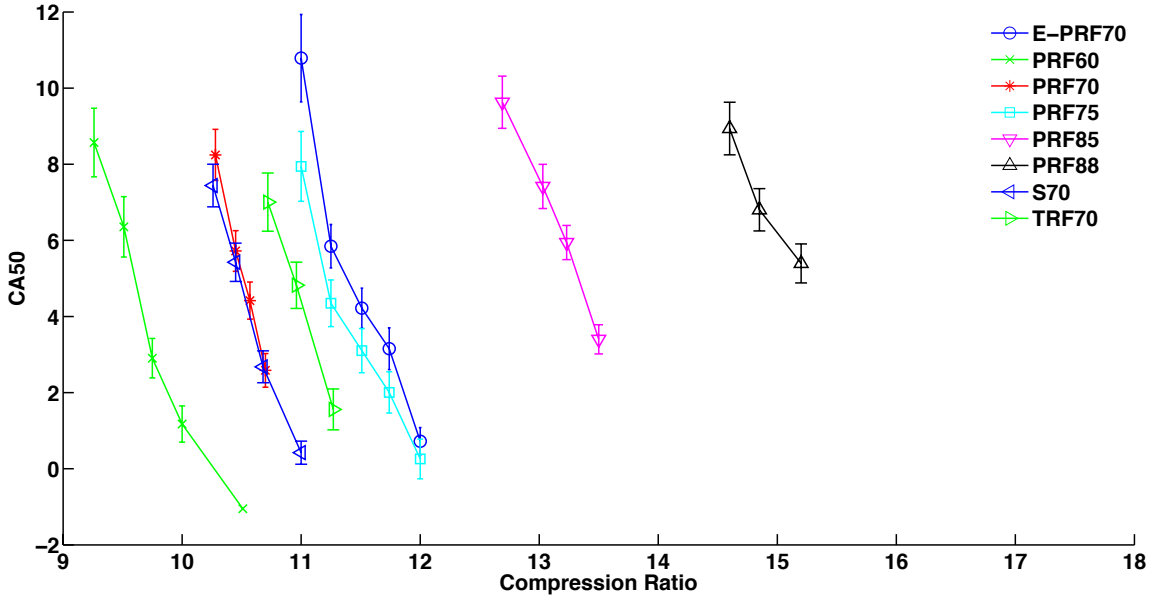

Figure 5.11: PRF70 and S70 auto-ignite at similar instances, but TRF70 and E-PRF70 auto-ignite later although all the fuels have a similar RON.

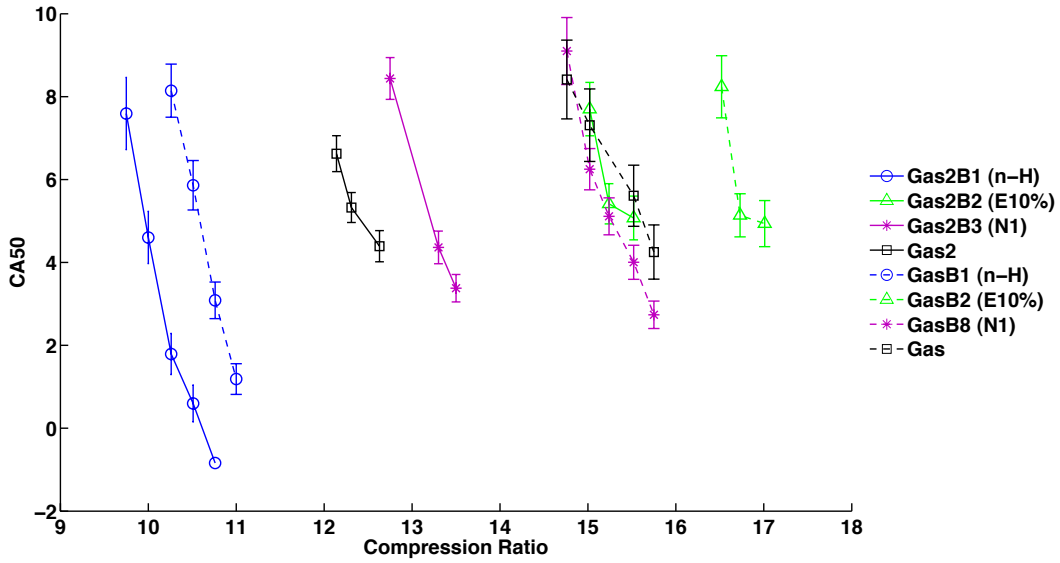

Figure 5.12: The same additive (fuels with matching colors and symbols) mixed with two different base fuels does not have the same affect on auto-ignition.

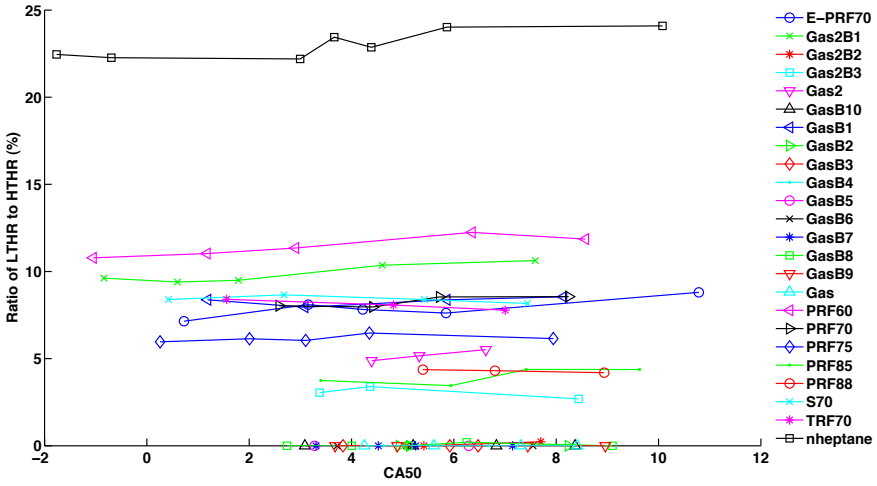

Figure 5.13: Almost all octane 70 fuels are grouped together and are bracketed by PRF60 and PRF75. Also, the ratio of low temperature heat release (LTHR) to high temperature heat release (HTHR) is constant with CA50.

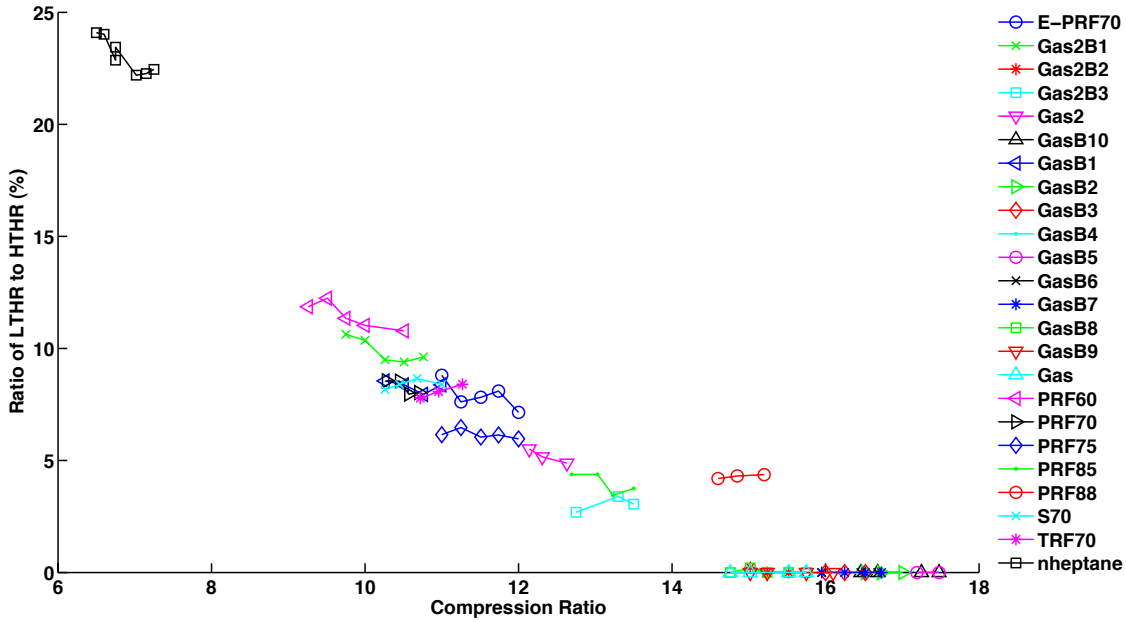

Figure 5.14: For each fuel, ratio of LTHR to HTHR does not vary with compression ratio. However, the ratio of LTHR to HTHR decreases linearly between fuels with increasing compression ratio.

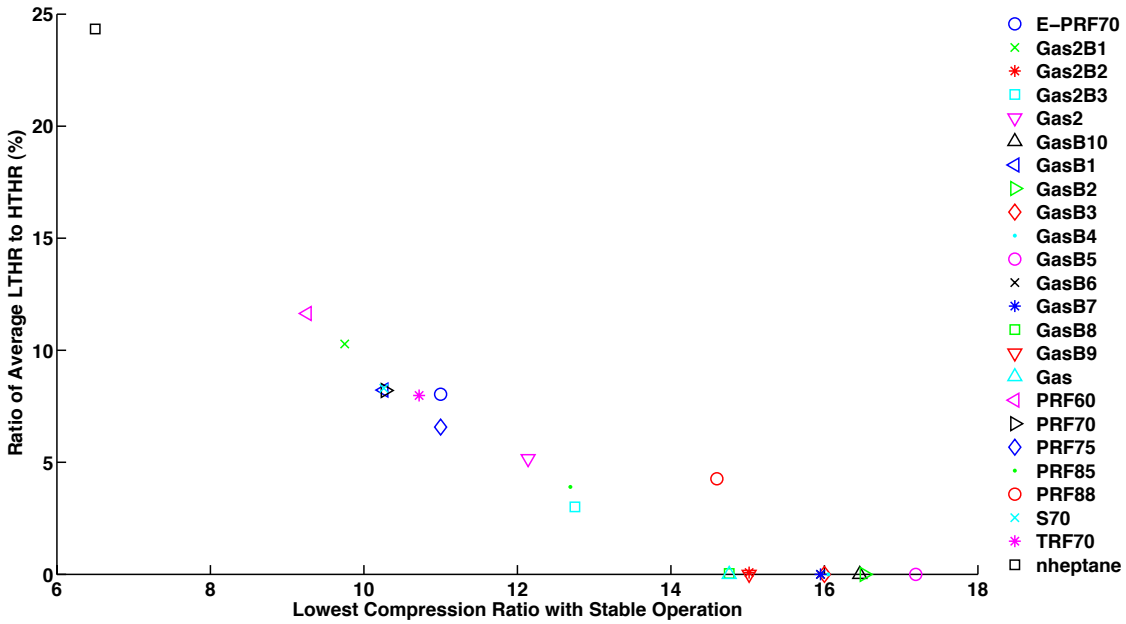

Figure 5.15: The ratio of LTHR to HTHR decreases linearly (R^2=0.84) with compression ratio for fuels with compression ratios for the onset of stable HCCI operation between 6 and 15.

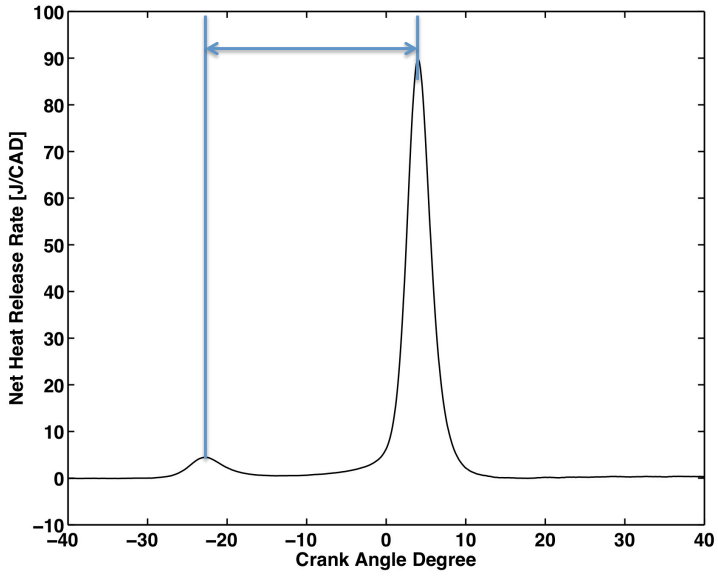

Figure 5.16: The delay (or Gap) between LTHR and HTHR is shown by the arrow.

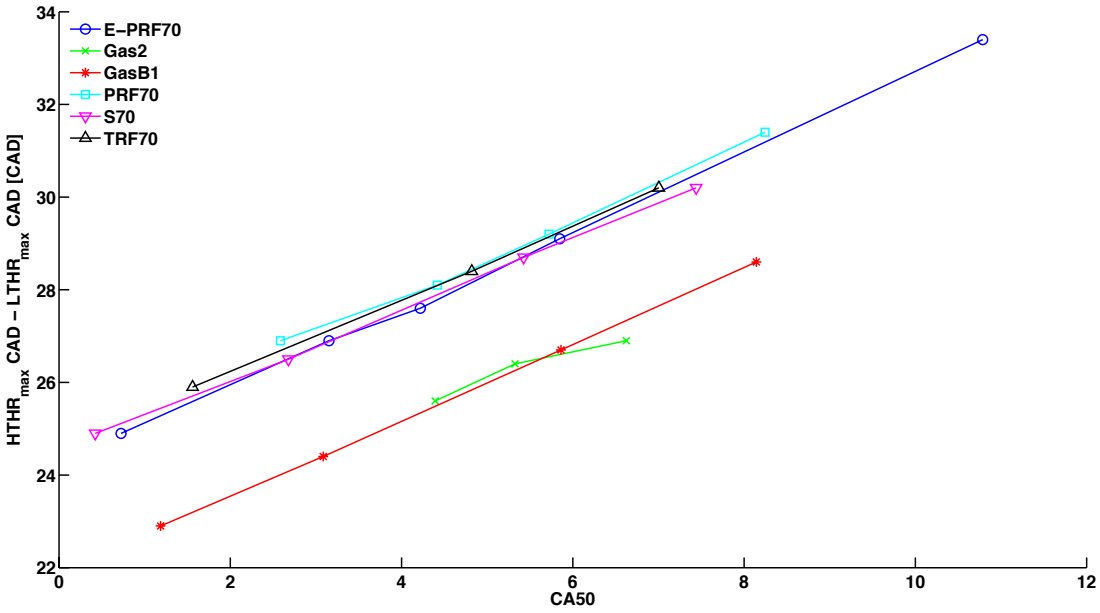

Figure 5.17: Octane 70 fuels are grouped by reference fuel blends and gasoline blends. Also, the delay between LTHR$_{max}$ and HTHR$_{max}$ increases linearly with CA50.

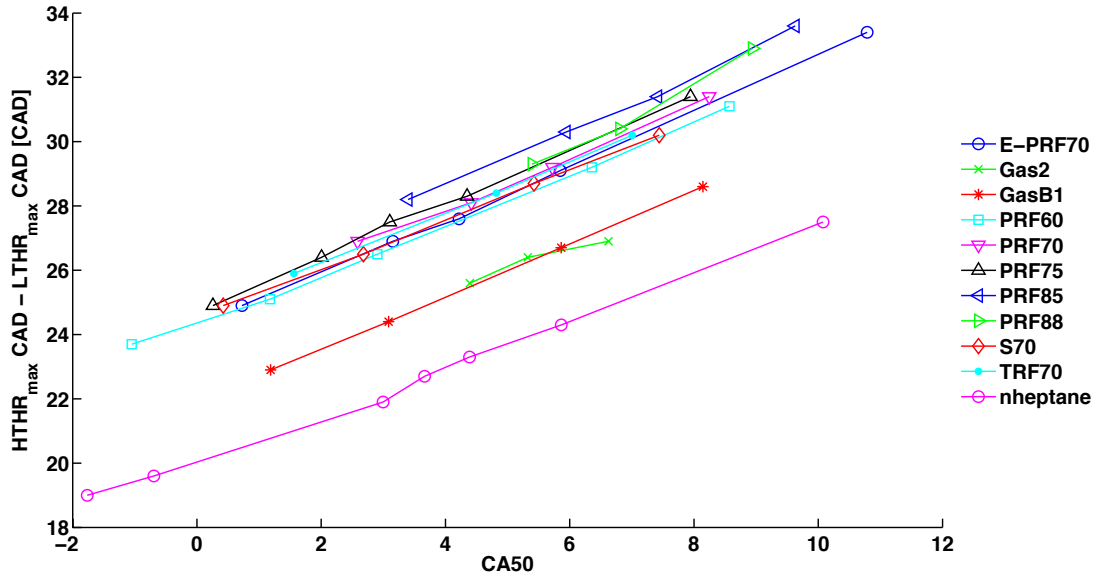

Figure 5.18: All reference fuels, except for pure n-heptane, are grouped together while the gasoline fuels are grouped separately. N-heptane has the smallest delay between LTHR$_{max}$ and HTHR$_{max}$

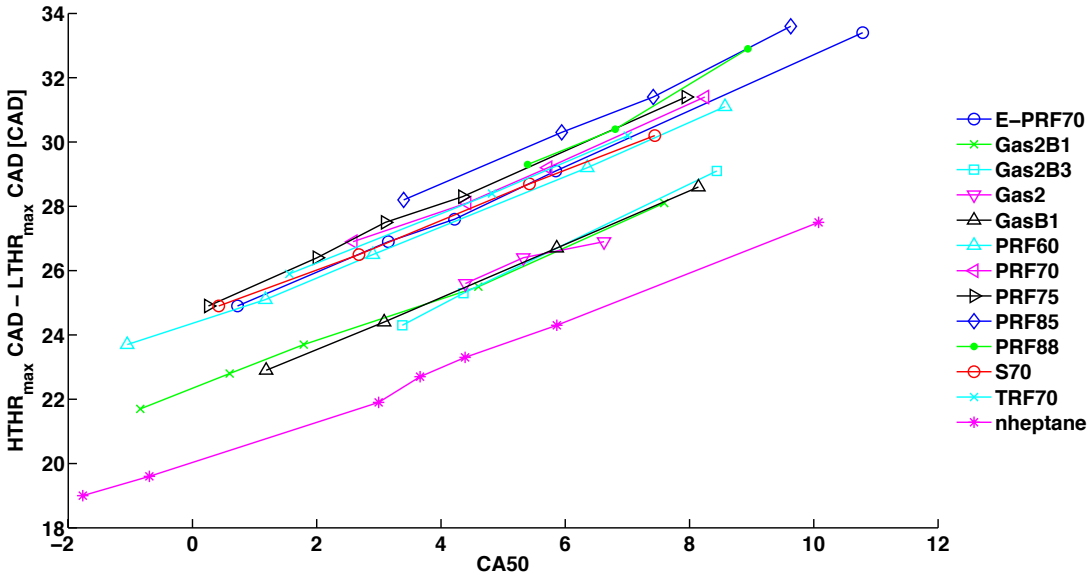

Figure 5.19: All the fuels with LTHR are grouped by gasoline and reference fuel, except for n-heptane which stands alone.

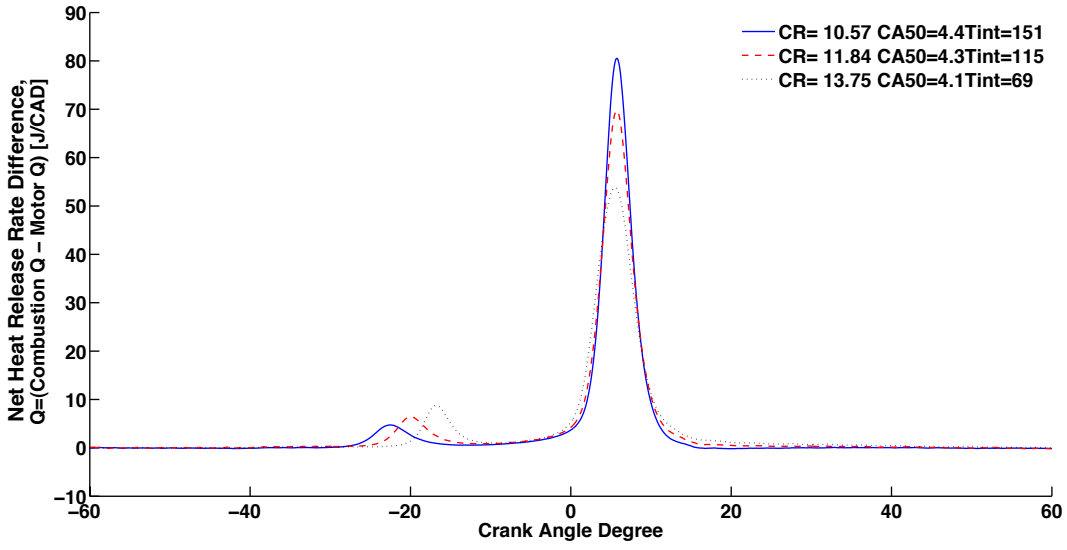

Figure 5.20: Changes in heat release rate of PRF70 at intake temperatures of 151°C, 115°C, and 69°C. As intake temperature increases, the amount of LTHR decreases and the crank angle difference between LTHR and HTHR increases, advancing LTHR for the same CA50.

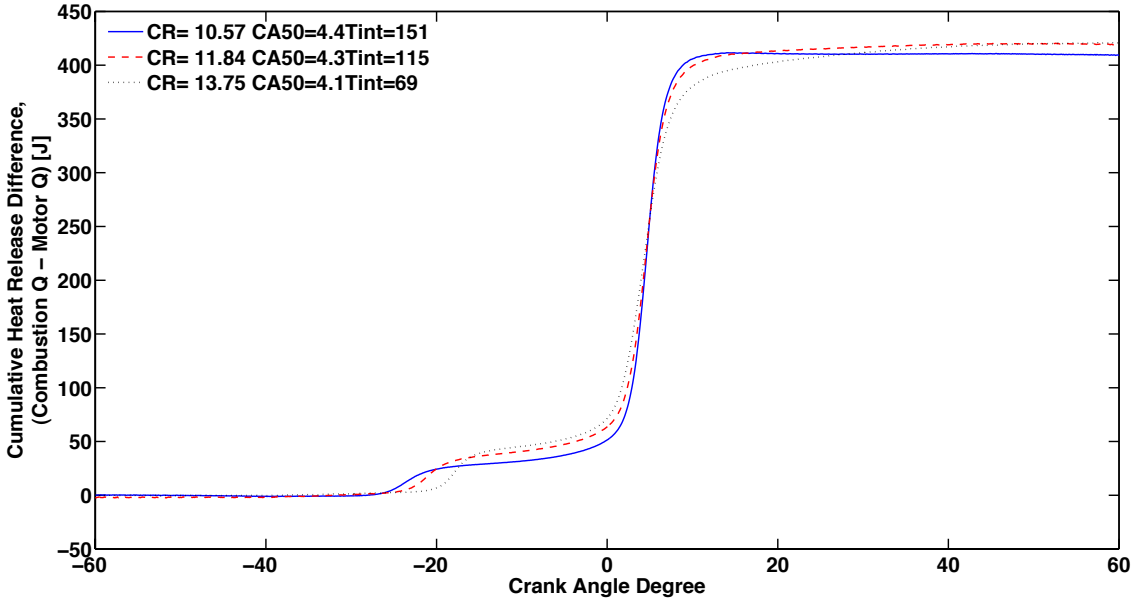

Figure 5.21: Changes in heat release rate of PRF70 at intake temperatures of 151°C, 115°C, and 69°C. The total heat release at each intake temperature remains constant.

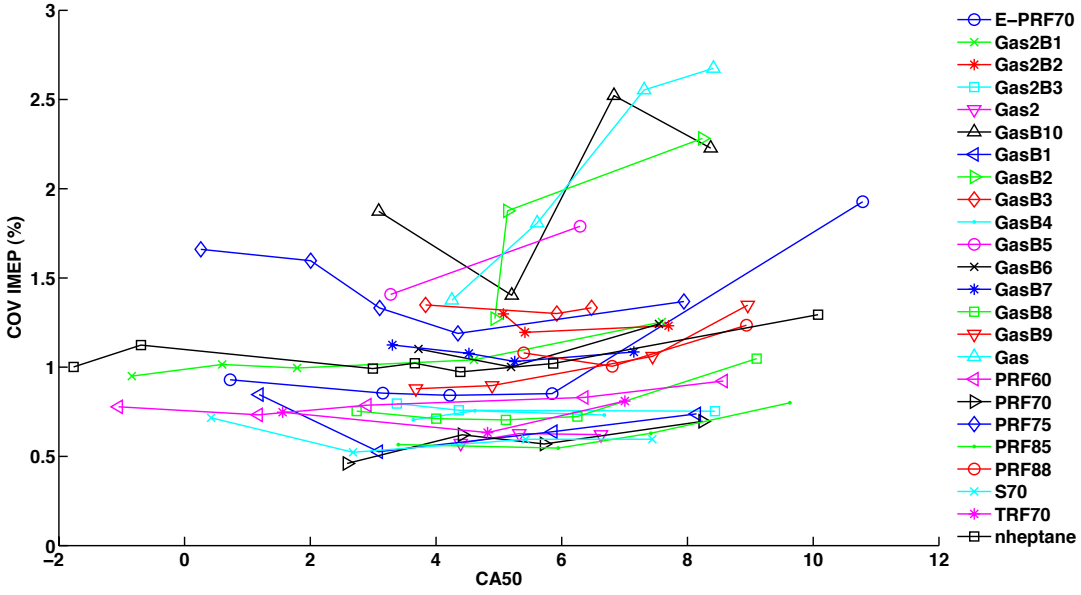

Figure 5.22: COV IMEP is less than 3% for all the fuels and Gas and GasB2 have the highest COV IMEP on average.

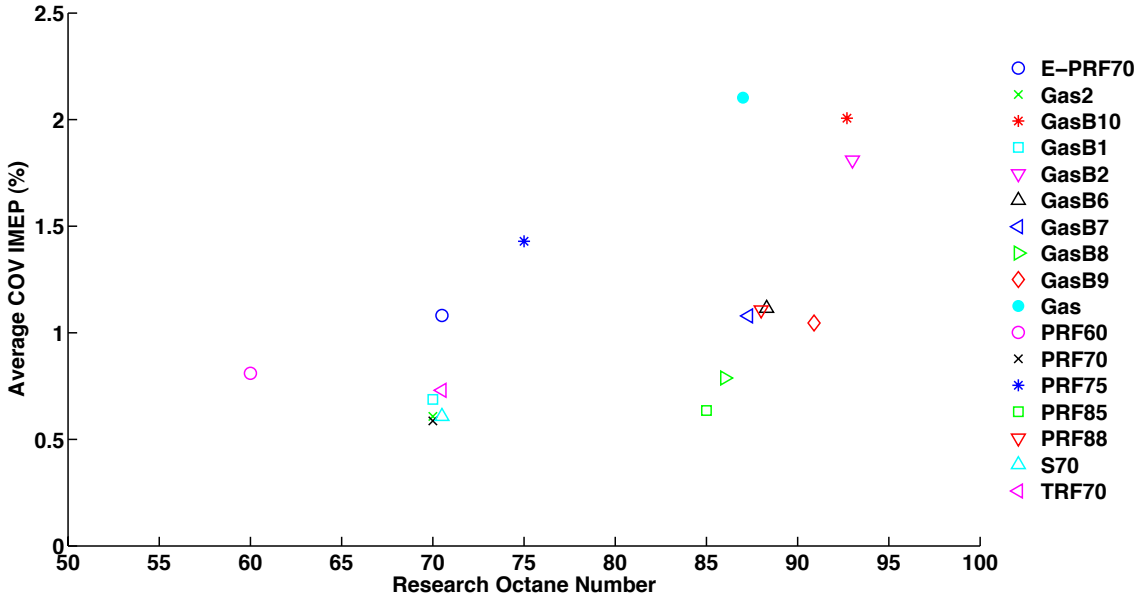

Figure 5.23: RON 70 fuels have some of the lowest average COV IMEP.

5.4 Single-Zone, Well-Mixed-Reactor Model for HCCI

A single-zone well-mixed-reactor (WMR) model is widely used for simulating HCCI because HCCI is primarily controlled by chemical kinetics and uses a homogenous mixture and remains relatively insensitive to turbulence and mixing effects [Chen *et al.*, 2003a; Aceves *et al.*, 2000]. The single-zone WMR models the combustion chamber and computes temperature, pressure, heat release, and other variables in this single zone. Because the model is zero dimensional and consists one zone, a grid is not needed, decreasing computational time, and detailed chemistry can be used. In the model, the intake and exhaust flows are integrated into the original single-zone WMR. This model offers fast results, provides reasonable estimates for start of combustion and saves computational time, but poorly predicts burn duration, peak temperature, and emissions [Chen, 2006; Aceves *et al.*, 2000].

The governing equations for the single-zone WMR model are as follows:

1. Mass balance equation:

$$\frac{dm}{dt} = \sum_{i=1}^{N} \dot{m}_i - \dot{m}_e, \tag{5.13}$$

where N is the number of intake flows (usually $N = 0$), the subscript i is for inlet conditions, and the subscript e is for exit conditions.

2. Species balance equation:

$$\frac{dY_k}{dt} = \frac{1}{m}\sum_{i=1}^{N}\dot{m}_i(Y_{k,i} - Y_k) - \frac{\dot{\omega_k}M_k}{\rho}, \tag{5.14}$$

where Y is the mass fraction of species, ω is the source term of the reaction, M is the molecular mass of the species, ρ is the mixture density, and the subscript k denotes the involved species.

3. Energy balance equation:

$$\frac{dT}{dt} = \frac{1}{C_p m}\sum_{i=1}^{S}\dot{m}_i\left(\sum^{k} k_{k=1}Y_k(h_{k,i} - h_k)\right) - \frac{\dot{Q_{loss}}}{C_p m} - \sum^{k} k_{k=1}\frac{\dot{\omega_k}h_k M_k}{C_p m} - \frac{1}{C_p m}\frac{dp}{dt}, \tag{5.15}$$

where C_p is the specific heat of the mixture at constant pressure, S is the number of streams, h is the enthalpy, kk indicates the number of species, and the overall heat loss, Q_{loss} is defined as,

$$\dot{Q_{loss}} = h_c(T - T_{wall})A_s, \tag{5.16}$$

where h_c is the overall heat transfer coefficient and A_s is the exposed surface area in the cylinder, which changes with piston location and T is the mixture temperature. The overall heat transfer coefficient (h_c) in equation 5.16 is determined using the modified Woschni's correlation [Chen, 2006],

$$h_c = 3.26A_s^{-0.2}p^{0.8}T^{-0.55}w^{0.8}, \tag{5.17}$$

where w is the average mixture velocity defined as [Heywood, 1988],

$$w = C_1 S_p + C_2(p - p_m)\frac{V_d T_r}{p_r V_r}, \tag{5.18}$$

where C_1 and C_2 are constants found in table 5.4, S_p is the mean piston speed, V_d is the displacement volume, p_m is the motored cylinder pressure, and the subscript r denotes the reference state [Heywood, 1988].

Table 5.4: Constants for average mixture velocity in equation 5.18

Event Description	C_1	C_2
Gas exchange	6.18	0
Compression Stroke	2.28	0
Combustion & expansion stroke	2.28	3.24×10^{-3}

More details regarding the governing equations for the single-zone WMR model can be found in Yi-Hann Chen's Dissertation [Chen, 2006].

5.5 Model Results and Discussion

Experimental results were compared with results from a single-zone WMR model with a genetic algorithm for HCCI [Chen *et al.*, 2003a]. Although a HCT model was developed previously for this CFR engine [Flowers *et al.*, 2000], the single-zone WMR model provides better accuracy when predicting the onset of auto-ignition. In this section, experimental results are compared to the single-zone WMR results for predicting changes in CA50 with compression ratio and changes in heat release with intake temperature.

5.5.1 CA50 and Compression Ratio

Three chemical mechanisms, containing reactions for toluene, n-heptane, and isooctane blends, are explored for modeling the CFR experimental data. The first chemical mechanism (MECH1) is a 5-component gas mechanism developed by Lawrence Livermore National Laboratory (LLNL) used in the research by Silke et al. [Silke *et al.*, 2008]. MECH1 was reduced to contain three fuel components: toluene, isooctane, and n-heptane. MECH1 provides a convergent solution for blends of two components, such as isooctane and n-heptane (PRF blends) or toluene and n-heptane (TRF blends). Using MECH1 for three blends caused the model to diverge.

Figure 5.24 shows a comparison between experimental data and the single-zone WMR model with MECH1 for PRF and TRF fuels. MECH1 predicts auto-ignition occurring at an higher compression ratio than the experimental data and the difference in the compression ratio for each fuel is inconsistent. Also, MECH1 suggests that addition of toluene advances ignition instead of delays ignition. Figure 5.24 shows TRF70 auto-igniting before PRF60 using MECH1, which does not agree with experimental results. Although MECH1 does not accurately predict the behavior of TRF70, it does predict the linear trend between CA50 and compression ratio with a similar slope and accurately predicts the order of auto-ignition of the PRF blends.

The second chemical mechanism (MECH2) was developed by Huang et al. [Huang *et al.*, 2010], which is capable of modeling blends containing two or three components containing toluene, isooctane, n-heptane, and/or ethanol. From figure 5.25 it can be seen that MECH2 predicts auto-ignition occurring at lower compression ratios than the experimental data. However, MECH2 does capture the effects of toluene. When a small amount of toluene is added to an n-heptane and iso-octane blend, like S70, (5% toluene), MECH2 predicts little deviation in auto-ignition from PRF70, agreeing with the experimental results. Also, MECH2 predicts TRF70 (54% toluene) auto-igniting after PRF70 and at a similar compression ratio as the data, but predicts a less steep slope and fails to predict auto-ignition later than CA50=2.

Aside from toluene, MECH2 has difficulty capturing the effects of ethanol. When substituting 5% ethanol for toluene in the S70 blend (now E-PRF70), MECH2 predicts ethanol having little to no effect on auto-ignition. However, the experimental data shows ethanol suppresses auto-ignition and requires higher compression ratios for auto-ignition, as expected. Differences in compression

ratio between the model and experimental data could be attributed to MECH2's low reactivity at low temperatures.

The third chemical mechanism (MECH3), developed by Andrae et al. [Andrae *et al.*, 2008], includes blends containing isooctane, n-heptane, and/or toluene. Figure 5.26 shows good agreement between MECH3 results and the CFR experimental data. Like the experimental data, MECH3 predicts a linear trend between CA50 with similar slopes and the trend in auto-ignition for the PRF blends and S70 matches the experimental data. Also, MECH3 predicts slightly earlier auto-ignition than the experimental data. The difference in ignition between the model and the data could be due to the model excluding effects of blow-by (escape of combustion gases past the pistons and piston rings into the crankcase during compression). At higher compression ratios, the difference between the data and MECH3 results are larger. Excluding blow-by could account for this difference because at higher compression ratios the amount of blow-by would increase. MECH3 also predicts TRF70 auto-igniting after PRF60, but before PRF70 and S70. TRF70 was expected to auto-ignite after S70, as shown by the experimental data, because TRF70 contains more toluene than S70 and toluene suppresses auto-ignition.

The single-zone WMR model using MECH3, developed by Andrae et al. [Andrae *et al.*, 2008], was modified to include blow-by (BB-WMR model). In BB-WMR model, blow-by was assumed to be a small leak, represented by a circular hole. The size of the hole in the BB-WMR model was determined by matching the peak model pressure with the peak motoring pressure from the experimental data. The area of the leak was found to be 0.008cm^2. Figure 5.27 shows good agreement between the experimental data and the BB-WMR model results for most PRF blends and S70. The difference between the BB-WMR model results and the data at higher compression ratios is smaller than the WMR model without blow-by; however, the difference between the data and the model for PRF88 is still large.

5.5.2 Modeling Auto-Ignition of Toluene Blends

Although MECH3 predicts PRF fuels well, MECH3 has trouble predicting auto-ignition of toluene blends. Figure 5.27 shows adding a little toluene, S70 (64% isooctane by volume, 31% n-heptane by volume, 5% toluene by volume), does not affect auto-ignition for both the model and the experimental data. However, a blend with more toluene, TRF70 (46% n-heptane by volume and 54% toluene by volume), is predicted to ignite before S70, which disagrees with the experimental data.

A sensitivity analysis of toluene and n-heptane blends was performed using the BB- WMR model with MECH3 [Andrae *et al.*, 2008]. The BB-WMR model was used to predict auto-ignition of toluene and n-heptane blends (TRF) at various compression ratios. The number prior to "TRF" indicates the amount of toluene, by volume, in the blend balanced by n-heptane. For example, 5 TRF indicates 5% toluene by volume blended with 95% n-heptane by volume. Table 5.5 lists the blends used in the sensitivity analysis and each blend's components by volume.

The BB-WMR model predicted delayed ignition as concentration of toluene increased, shown

Table 5.5: Toluene blends (TRF) composition by volume percent.

Fuel Name	% N-Heptane	% Toluene
1TRF	99	1
2TRF	98	2
3TRF	97	3
4TRF	96	4
5TRF	95	5
6TRF	94	6
7TRF	93	7
8TRF	92	8
9TRF	91	9
10TRF	90	10
20TRF	80	20
30TRF	70	30
50TRF	50	50
70TRF	30	70
80TRF	20	80
90TRF	5	90

in figure 5.28, as expected. However, the linear increase in toluene concentration did not results in a linear increase in auto-ignition delay time. Figure 5.28(a) shows the difference in compression ratio between 30TRF and 50TRF is less than the difference between 50TRF and 70TRF. Also, the difference in compression ratio between n-heptane and 1TRF is larger than 1TRF and 2TRF, as shown in figure 5.28(b).

Figure 5.29 shows how the BB-WMR model using MECH3 predicts changes in the ratio of CA50 to compression ratio (or the slope) with increasing amounts of toluene, by volume. The MECH3 did not predict a linear decrease in slope (CA50/compression ratio) as toluene concentration increased. For toluene fuel blends with less than 10% by volume of toluene, the model predicted increasing and decreasing slopes with the addition of toluene. The results suggests that MECH3 may not be sufficient at predicting ignition of toluene/n-heptane blends with small (less than 10%) concentrations of toluene. A linear decrease in slope is apparent in TRF blends containing 20% to 80% toluene. However, auto-ignition of TRF70, shown in the previous section, was not accurately predicted by MECH3.

5.5.3 Modeling Effects of Intake Temperature on Heat Release and Auto-ignition

The single-zone WMR model, without blow-by (WMR model), was used with the mechanism developed by Mehl et al. [Mehl *et al.*, 2011] to study the effects of intake temperature on LTHR and HTHR for PRF70. For a fixed intake temperature and compression ratio, the heat transfer rate in the WMR model was varied to match the experimental data CA50. In section 5.3.3, the experimental results show increasing intake temperature decreases the amount of LTHR and increases the Gap between HTHR and LTHR, advancing LTHR. Figure 5.30 shows the model predicting similar trends as the experimental data. The highest intake temperature produced the lowest amount of LTHR and had the largest delay between LTHR and HTHR. The lowest intake temperature produced the largest amount of LTHR and had the shortest delay between LTHR and LTHR. However, the WMR model predicts a higher peak in LTHR than the experimental data for the lowest intake temperature. The sharp peak in LTHR is due to using a single zone. A multi-zone model would give a smoother pressure rise. In the experimental data, the pressure data was filtered to reduce noise and could account for some of the differences.

Figure 5.31 shows that the onset of low temperature heat release for all three cases occurs around 780 K and ends around 850 K. Also, the highest amount of heat release occurs at an intake temperature of 69 °C, resulting in more chemical activity, advancing the onset of high temperature ignition. Figure 5.32, shows the change in in-cylinder temperature with crank angle degree for each case. The results show the highest intake temperature (151°C) advances the onset of LTHR. The lowest intake temperature (69°C) has the shortest delay between LTHR and HTHR. These results agree with theory because increasing the intake temperature promotes the reverse reaction of reaction (R11) and cuts off the low temperature combustion earlier. Both figures 5.31 and 5.32 capture the same trends seen in the experimental data.

The heat release rate was also compared to the in-cylinder pressure, shown in Figure 5.33. The model shows that the largest LTHR is largest corresponds to a slightly higher in-cylinder pressure and the lowest intake pressure. More LTHR was expected for the lowest intake temperature because higher pressure, from increasing the compression ratio, promotes the forward reaction of reaction (R11).

Auto-ignition and the Gap (delay time , in CAD, between LTHR and HTHR) at a constant intake pressure was also investigated at different intake temperatures for a compression ratio of 10.6 . Table 5.6 summarizes the differences in peak LTHR location and delay between LTHR and HTHR when intake temperature is varied at a constant intake pressure and compression ratio. The model shows that decreasing the intake temperature delays LTHR and has almost no effect on the delay between LTHR and HTHR. Increasing intake temperature shows LTHR advancing but the delay between LTHR and HTHR remaining almost the same. These results suggest that the delay between LTHR and HTHR may be independent of intake temperature.

This model was also used to study the effects of intake pressure on peak LTHR location and the

delay between LTHR and HTHR at a constant intake temperature and compression ratio. Table 5.7 shows that decreasing intake pressure increases the delay between LTHR and HTHR and delays LTHR. Increasing the intake pressure decreases the delay between LTHR and HTHR and advances LTHR. These results suggest that the delay between LTHR and HTHR is a function of intake pressure and the location at the onset of LTHR is a function of intake temperature and intake pressure.

Table 5.6: Effects of Intake Temperature on LTHR, and LTHR to HTHR delay at a compression ratio of 10.57 and an intake pressure of 1 bar. Experiments were conducted at 151°C intake temperature.

Intake Temperature (°C)	Peak LTHR Location (CAD ATDC)	HTHR to LTHR Delay (CAD)
131	-24.2	23.83
151 (Exp. Condition)	-28.1	23.4
161	-29.8	23.81

Table 5.7: Effects of Intake Temperature on LTHR, and LTHR to HTHR delay at a compression ratio of 10.57 and an intake temperature of 151°C. Experiments were conducted at 1 bar intake pressure.

Intake Pressure (bar)	Peak LTHR Location (CAD ATDC)	HTHR to LTHR Delay (CAD)
1.2	-29.2	20.98
1 (Exp. Condition)	-28.1	23.4
0.9	-27.2	25.74
0.8	-24.0	36.96

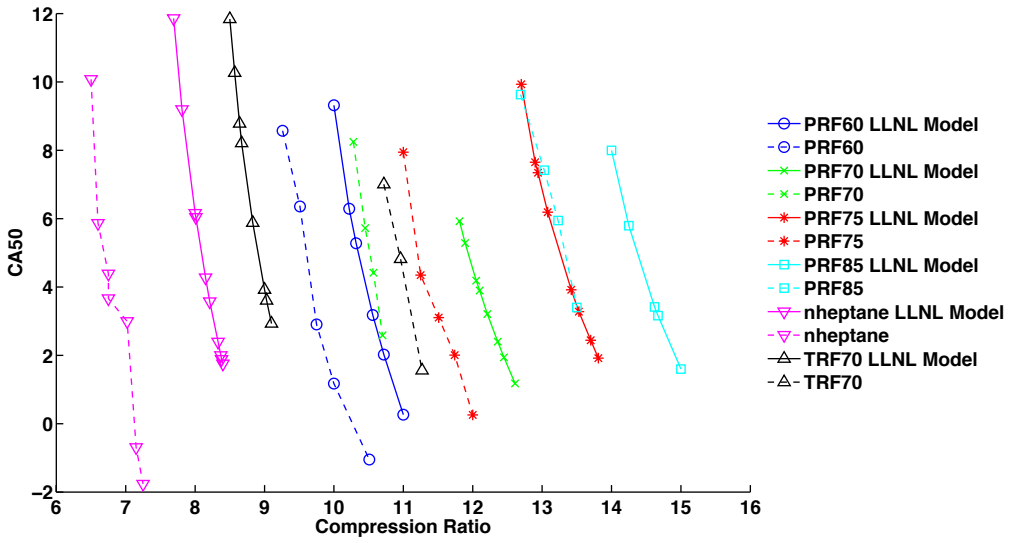

Figure 5.24: MECH1 [Silke *et al.*, 2008] (solid lines) predicts auto-ignition at higher compression ratios than the the data (dashed lines). Also, the mechanism does not accurately predict auto-ignition of toluene blended fuels as TRF70 is predicted to auto-ignite before PRF60, which is not shown by the experimental data.

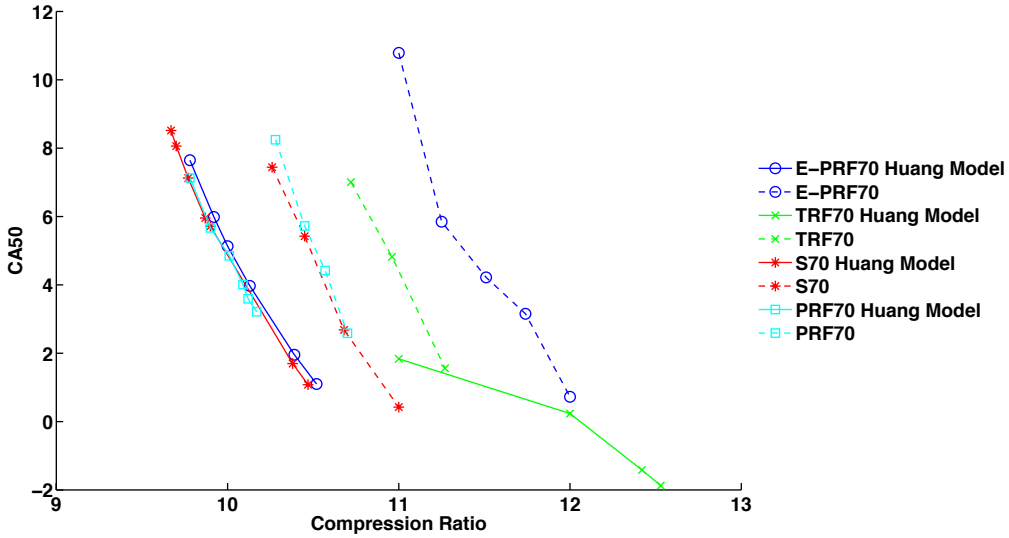

Figure 5.25: MECH2 [Huang *et al.*, 2010] predicts auto-ignition at lower compression ratios and predicts the correct effects of toluene. However, MECH2 does not predict auto-ignition of TRF70 later than CA50=2 and shows ethanol having almost no effect on suppressing auto-ignition.

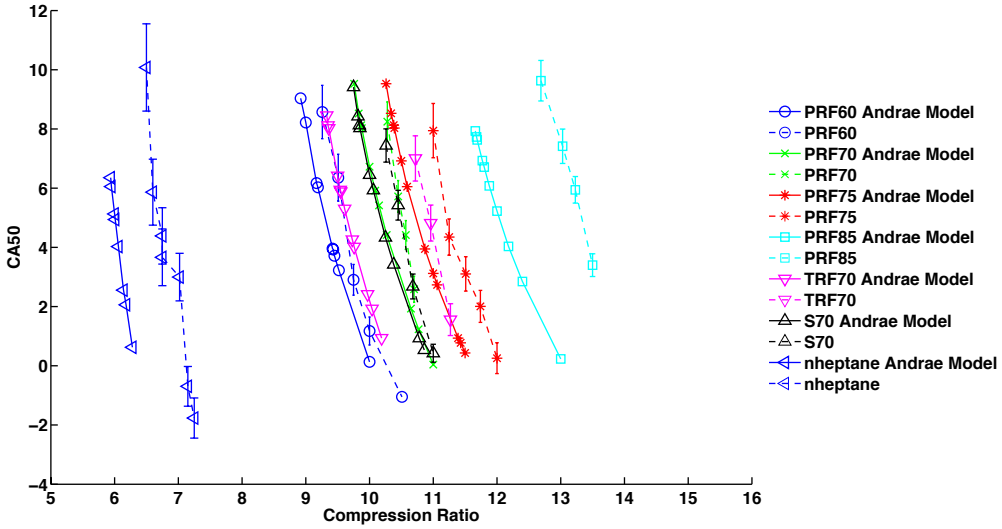

Figure 5.26: MECH3 [Andrae *et al.*, 2008] (solid lines) predicts an earlier ignition time than the data (dashed lines), possibly due to neglecting effects of blow-by in the model. MECH3 also has trouble predicting auto-ignition of TRF70.

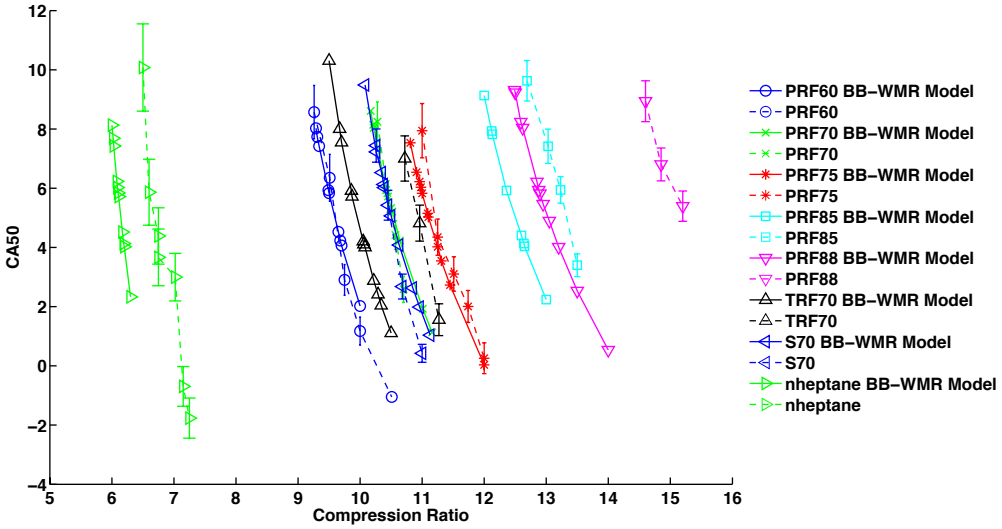

Figure 5.27: The WMR model with blow-by (BB-WMR) better matched the experimental data. However, at the higher and lower compression ratios, the difference between the BB-WMR model and the experimental data still exists.

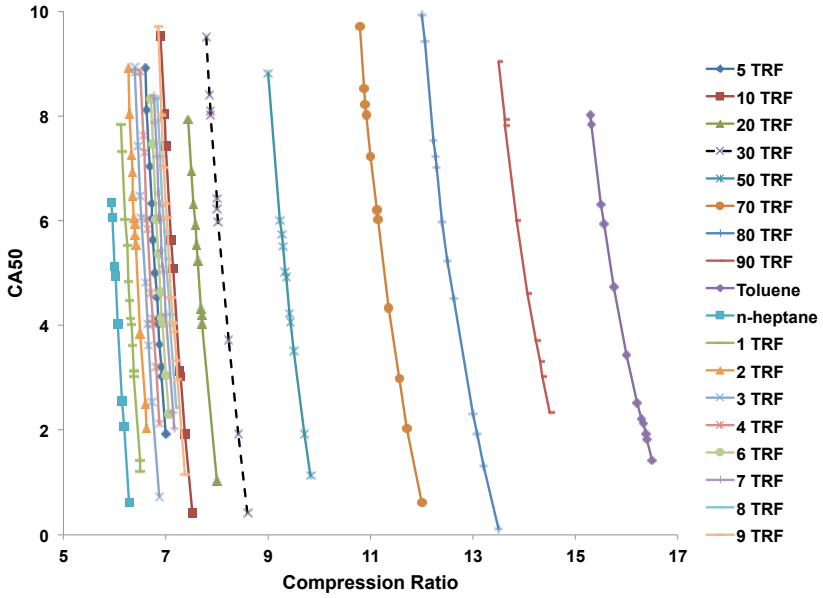

(a) TRF 0 (n-heptane) to TRF100 (toluene) blends.

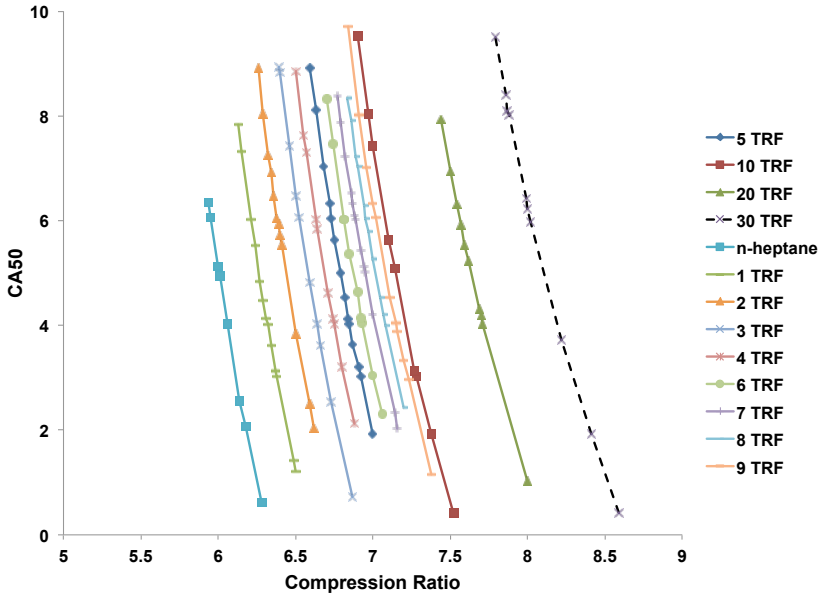

(b) TRF blends with less than 30% toluene.

Figure 5.28: The Single-Zone WMR model with blow-by (BB-WMR) predicted delayed auto-ignition as concentration of toluene increases in TRF (toluene/n-heptane) blends. Increasing the amount of toluene linearly by volume did not result in a linear increase in compression ratio.

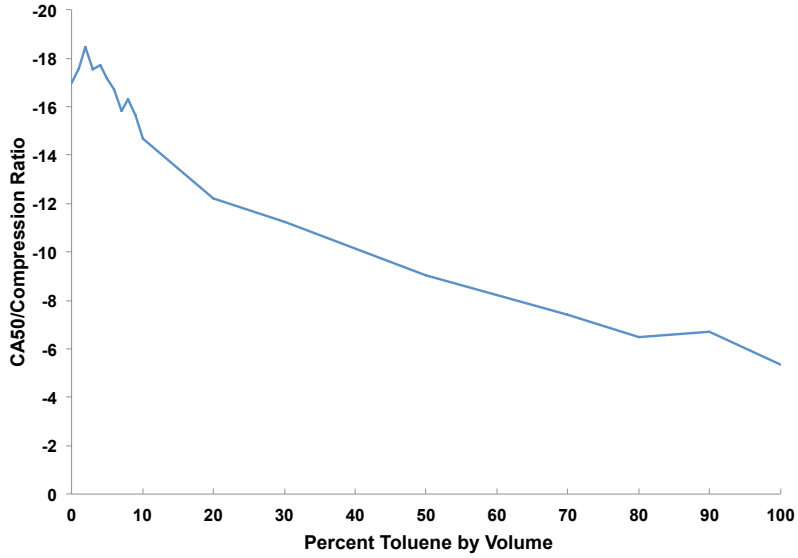

Figure 5.29: MECH3 predicted slopes (CA50/CR) for toluene/n-heptane blends shows inconsistencies for blends with less than 10% toluene by volume.

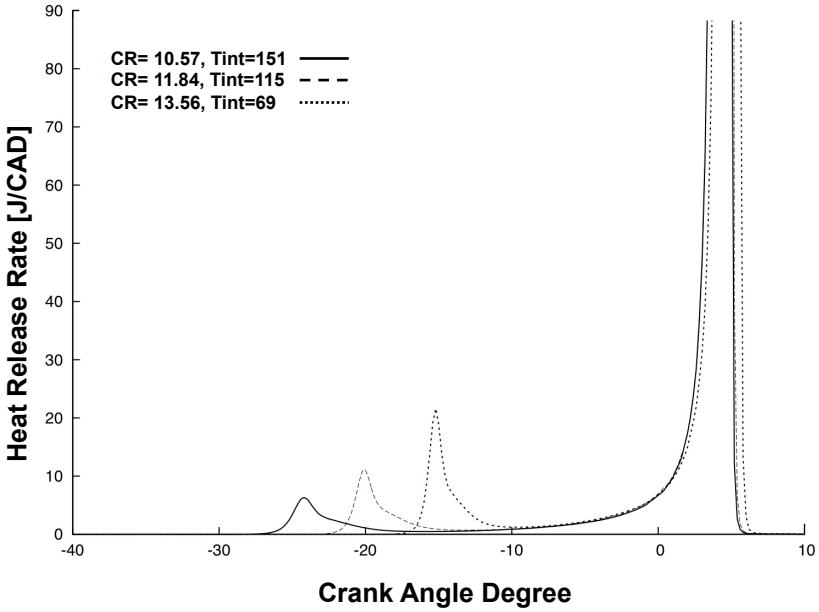

Figure 5.30: Single-zone WMR model shows increasing LTHR with decreasing intake temperature, matching the experimental data. The model data was shifted so CA50 was constant with varying intake temperature.

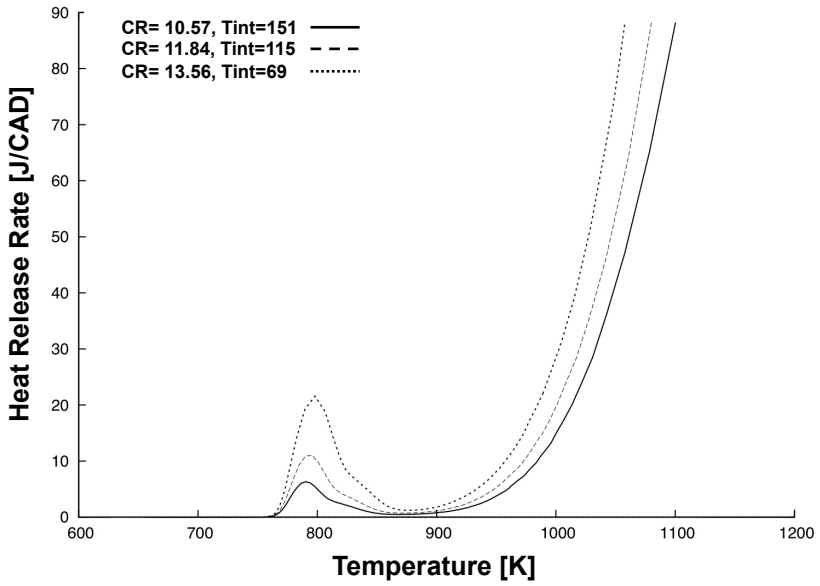

Figure 5.31: The onset of LTHR for each case occurs at ≈780 K. The lowest intake temperature leads to high temperature ignition fastest, suggesting more chemical activity.

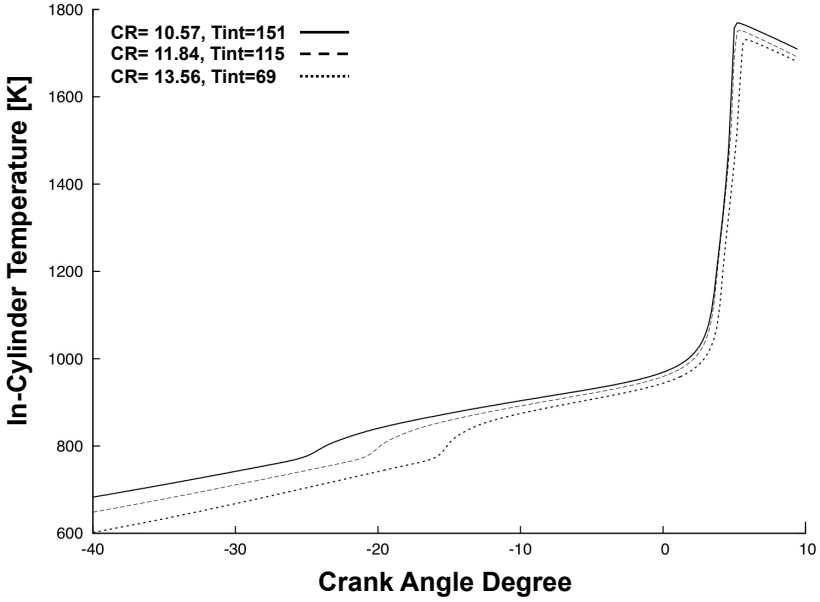

Figure 5.32: The highest intake temperature case reaches 780 K, the temperature at the onset of LTHR, fastest.

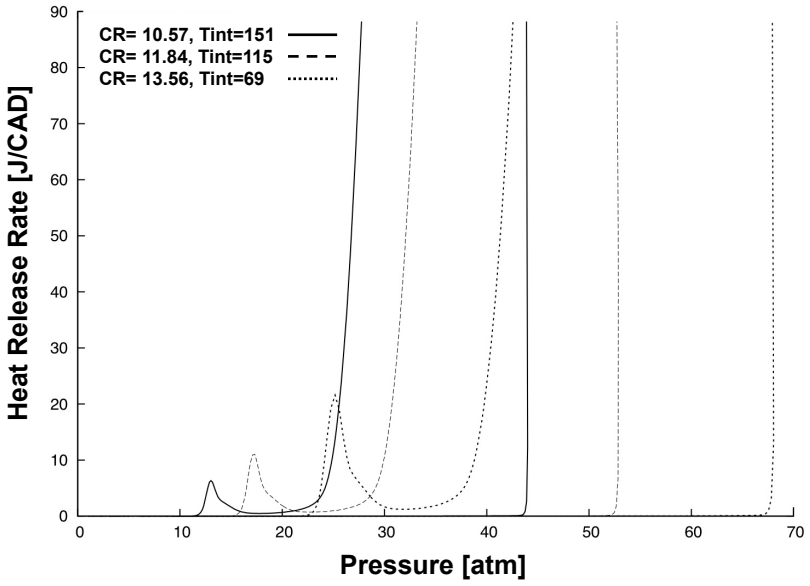

Figure 5.33: The highest intake temperature case reaches 780 K, the temperature at the onset of LTHR, fastest.

5.6 Summary

Correlations between auto-ignition and different variables were investigated by testing twenty-four different fuels in a CFR engine. For a fixed intake temperature, CA50 is found to vary linearly with compression ratio, partially resembling calibration curves used in octane tests. Fuels of similar octane rating did not auto-ignite corresponding to their respective octane number. Similar results were found using Cetane number. Therefore, octane number and cetane number are not sufficient for characterizing HCCI fuels. Primary reference fuels (PRF), blends of isooctane and n-heptane, did not bracket fuels of similar octane number and are not suitable reference fuels for a HCCI index.

The Octane Index, developed by Kalghatgi [Kalghatgi, 2005], shows almost a linear trend with the compression ratio at the onset of auto-ignition. It accurately predicted auto-ignition for blends containing two components of hydrocarbons, such as PRFs and TRFs, but did not accurately predict auto-ignition of fuels containing ethanol, small amounts of toluene, or gasoline blendstocks.

The HCCI Index developed by Shibata and Urushihara [Shibata and Urushihara, 2007; Shibata and Urushihara, 2009] gave similar results to the Octane Index, but had difficulty predicting auto-ignition of fuels containing ethanol and larger amounts of toluene. Specifically, TRF70 was predicted to auto-ignite at the same time as PRF70, but the experimental data showed TRF70 auto-igniting after PRF70. The HCCI Index also had difficulty accurately predicting auto-ignition of gasoline blends with different aromatic compounds, suggesting aromatic compounds do not be-

have similarly and should not be grouped together.

Previous methods for predicting auto-ignition show that a single variable may not be able to accurately predict auto-ignition in HCCI engines. Therefore, two or more variables may be required, similar to determining octane number. One trend identified for characterizing auto-ignition in HCCI engines, is CA50. As stated previously, CA50 varied linearly with compression ratio and providing an order for auto-ignition. Also, the ratio of CA50 to compression ratio, or the slope of the line, shows the sensitivity of auto-ignition to compression ratio for any given fuel.

Another trend for characterizing auto-ignition in HCCI engines is LTHR and HTHR. The ratio of LTHR to HTHR varied linearly with the compression ratio at the onset of auto-ignition (R^2=0.84), but no correlation was found with CA50. Comparing changes in the delay (Gap) between LTHR and HTHR with CA50 grouped fuels by major components. The reference fuels and gasoline based fuels were grouped separately while n-heptane stood alone.

Experimental results showed decreasing intake temperature, while keeping intake pressure and equivalence ratio constant, increased the amount of LTHR and decreased the delay between LTHR and HTHR. A single-zone WMR model was used to verify the trend and showed that varying intake temperature affects LTHR and CA50 while varying intake pressure affects LTHR and the delay between LTHR and HTHR. Therefore, decreasing the intake temperature, while simultaneously increasing the compression ratio to maintain the same CA50, delays the start of low temperature combustion (due to decreasing intake temperature) and decreases the delay between low temperature combustion and high temperature combustion (due to the increased pressure from the higher compression ratio).

COV IMEP showed no identifiable trend with CA50. However, all fuels had a COV IMEP less than 3% and the fuels with the lowest average COV IMEP had an octane number of 70. Also, COV IMEP increased as CA50 increased, as expected.

The single-zone WMR model was also used to verify linear trends between CA50 and compression ratio. Three different mechanisms were used to predict auto-ignition and trends shown by the experimental data. All three mechanisms accurately predicted the auto-ignition order of PRF fuels, but had difficulty predicting blends containing toluene and ethanol. The mechanism developed by Andrae et al. [Andrae *et al.*, 2008] provided the most accurate prediction of auto-ignition and trends shown by the experimental data, but did not accurately predict auto-ignition of blends containing toluene.

A sensitivity test was conducted using the single-zone WMR model for blends of toluene and n-heptane to identify potential problems with the mechanism. The model results showed the mechanism having difficulty predicting auto-ignition of blends with less than 10% toluene and showed increasing the amount of toluene linearly by volume did not result in a linear increase in compression ratio.

Overall, the results showed promising trends for creating a future, standardized HCCI number. More fuel blends containing toluene, ethanol, and various aromatics should be explored to help identify reference fuels for an HCCI number. The model accurately predicted trends of PRFs but the mechanisms for toluene blends and ethanol should be investigated and further developed to better predict experimental results.

Chapter 6

Uncertainty Analysis

An uncertainty analysis was performed on all measurements and calculations. The uncertainty for all measured values contained two parts: the random error and the systematic error (or bias). The random error (R_y) in a measured variable y was calculated using[Coleman and Steele, 2009],

$$R_y = 2 \times \sigma_{\overline{y}} = \frac{2\sigma_y}{\sqrt{N}}, \tag{6.1}$$

where $\sigma_{\overline{y}}$ is the standard error, y is the measured value, N is the number of cycles, σ_y is the standard deviation, defined as

$$\sigma_y = \left(\frac{1}{N-1} \sum_{i=1}^{n} (y_i - \overline{y})^2 \right)^{\frac{1}{2}}, \tag{6.2}$$

and $\overline{y}$ is the mean of the measured values. This method assumes 95% confidence intervals. The systematic error was provided by the manufacturer of the equipment. The uncertainty in measured values (U_y) was determined by combining the random error and the systematic error using,

$$U_y = \sqrt{R_y^2 + B_y^2}, \tag{6.3}$$

where B_y is the systematic error.

For uncertainties within calculations, the general formula for uncertainty in a function U_r depending on several variables was used [Taylor, 1997; Coleman and Steele, 2009]:

$$U_r = \sqrt{\left(\frac{\partial r}{\partial x_1} U_{x_1} \right)^2 + \left(\frac{\partial r}{\partial x_2} U_{x_2} \right)^2 + ... \left(\frac{\partial r}{\partial x_n} U_{x_n} \right)^2}, \tag{6.4}$$

where r is the function, x_n are independent variables, and U_{x_n} are measured or calculated uncertainties of each independent variable.

Using equations 6.3 and 6.4, uncertainty in the measured and calculated variables was determined for each experiment. The uncertainty for each variable is outlined in the following sections.

6.1 In-Cylinder Pressure

As mentioned in the Chapter 3, the in-cylinder pressure was measured using a 6052B Kistler piezoelectric pressure transducer in conjunction with a 5044A Kistler charge amplifier. The systematic error for the transducer, B_P, is listed as 0.2 bar. Random error in the pressure data were calculated for at least 300 thermodynamic cycles (720 CAD) using equation 6.1. The uncertainty of the pressure measurements was determined using equation 6.3, giving [Coleman and Steele, 2009; Taylor, 1997],

$$U_p = \sqrt{R_p^2 + B_p^2}. \tag{6.5}$$

6.2 Volume

The volume was determined using equation 2.11. Top Dead Center (TDC) of the motoring traces was calculated using the method outlined by Tunestal [Tunestal, 2009]. The uncertainty in crank angle degree, using Tunestal's method to find TDC, is 0.05 CAD. Using equation 6.4, the uncertainty in volume was determined by,

$$U_V = \left(\frac{dV}{d\theta} U_\theta \right), \tag{6.6}$$

where,

$$\frac{dV}{d\theta} = \frac{1}{4}\pi B^2 \left(a\sin(\theta) + \frac{a^2 \sin(\theta)\cos(\theta)}{\sqrt{l^2 - a^2\sin(\theta)^2}} \right). \tag{6.7}$$

In equation 6.7, the bore (B), connecting rod length (l), and the crank radius (a) can be found in Table 3.1.

6.3 Specific Heat Ratio

Uncertainty in the specific heat ratio was determined using equation 6.1.

6.4 Cumulative Net Heat Release

The uncertainty calculation for heat release (Q_i) at each crank angle degree i was performed by dividing equation 2.17 into two terms A,

$$A = \frac{1}{\gamma - 1}[p_i V_i - p_0 V_0], \tag{6.8}$$

and B,

$$B = \sum_{j=0}^{i} p_j (\Delta V)_j. \tag{6.9}$$

Equation 2.17 assumes the in-cylinder pressure is taken in crank angle degree increments. For the CFR, in-cylinder pressure data was taken every 0.1 CAD. Therefore the subscript 0 denotes the in-cylinder pressure taken at the initial CAD and the subscript i denotes the crank angle degree of interest.

The uncertainty in A can be found using equation 6.4, which yields,

$$\begin{aligned} U_A^2 &= \left(\frac{\partial A}{\partial \gamma} U_\gamma\right)^2 + \left(\frac{\partial A}{\partial p_i} U_{p_i}\right)^2 + \left(\frac{\partial A}{\partial V_i} U_{V_i}\right)^2 + \left(\frac{\partial A}{\partial p_0} U_{p_0}\right)^2 + \left(\frac{\partial A}{\partial V_0} U_{V_0}\right)^2 \\ &= \left(-\frac{p_i V_i - p_0 {V_0}^2}{\gamma - 1} U_\gamma\right)^2 + \left(\frac{V_i}{\gamma - 1} U_{p_i}\right)^2 + \left(\frac{p_i}{\gamma - 1} U_{V_i}\right)^2 \\ &\quad + \left(-\frac{V_0}{\gamma - 1} U_{p_0}\right)^2 + \left(-\frac{p_0}{\gamma - 1} U_{V_0}\right)^2 \end{aligned} \tag{6.10}$$

Similarly, the uncertainty in B is found to be,

$$\begin{aligned} U_B^2 &= \left(\frac{\partial b}{\partial p_1} U_{p_1}\right)^2 + \left(\frac{\partial B}{\partial \Delta V_1} U_{\Delta V_1}\right)^2 + \left(\frac{\partial B}{\partial p_2} U_{p_2}\right)^2 + \left(\frac{\partial B}{\partial \Delta V_2} U_{\Delta V_2}\right)^2 + \dots \\ &\quad + \left(\frac{\partial B}{\partial p_i} U_{p_i}\right)^2 + \left(\frac{\partial B}{\partial \Delta V_i} U_{\Delta V_i}\right)^2 \\ &= (\Delta V_1 U_{P_1})^2 + (p_1 U_{\Delta V_1})^2 + (\Delta V_2 U_{P_2})^2 + (p_2 U_{\Delta V_2})^2 + \dots \\ &\quad + (\Delta V_i U_{P_i})^2 + (p_i U_{\Delta V_i})^2 \end{aligned} \tag{6.11}$$

After computing the uncertainty in the first and second terms, the uncertainty in Q_i at crank angle degree i is found by [Taylor, 1997]

$$U_{Q_i} = \sqrt{U_A^2 + U_B^2} \tag{6.12}$$

6.5 CA50

Uncertainty in the CA50 was determined using [Taylor, 1997]

$$U_{CA50} = |\theta(Q_{50\%} + U_{Q_{50\%}}) - \theta_{Q_{50\%}}| \tag{6.13}$$

6.6 Indicated Work

Indicated work was approximated using the trapezoidal method of integration, as shown by equation 2.9. Using equation 6.4, the uncertainty in the work can be determined by differentiating the

indicated work by each dependent variable in equation 2.9, which yields,

$$\begin{aligned} U_W^2 &= \left(\frac{\partial W}{\partial \Delta V_1} U_{\Delta V_1}\right)^2 + \left(\frac{\partial W}{\partial P_1} U_{P_1}\right)^2 + \left(\frac{\partial W}{\partial P_2} U_{P_2}\right)^2 + \dots \\ &\quad + \left(\frac{\partial W}{\partial \Delta V_{N-1}} U_{\Delta V_{N-1}}\right)^2 + \left(\frac{\partial W}{\partial P_{N-1}} U_{P_{N-1}}\right)^2 + \left(\frac{\partial W}{\partial P_N} U_{P_N}\right)^2. \end{aligned} \tag{6.14}$$

Because the trapezoidal rule estimates the area as trapezoidal sections, the subscripts *1* and *2* represent the end-points of each trapezoidal section.

6.7 Indicated Power, *IMEP*, and Indicated Thermal Efficiency

Knowing the uncertainty in the work, the uncertainty in the indicated power, indicated mean effective pressure (*IMEP*) and the indicated thermal efficiency (η_{th}) can be determined using the equation for uncertainty in products and quotients:

$$\left(\frac{U_r}{|r|}\right)^2 = \left(\frac{U_{x_1}}{|x_1|}\right)^2 + \left(\frac{U_{x_2}}{|x_2|}\right)^2 + \dots + \left(\frac{U_{x_n}}{|x_n|}\right)^2 \tag{6.15}$$

where uncertainty is being measured in r and x_n are independent variables with measured uncertainties [Taylor, 1997].

Using equation 6.15, the uncertainty in indicated power (P_i), *IMEP*, and η_{th} can be determined by,

$$U_{P_i} = P_i \left(\frac{U_W}{W}\right), \tag{6.16}$$

$$U_{IMEP} = IMEP \left(\frac{U_W}{W}\right), \text{ and} \tag{6.17}$$

$$U_{\eta_{th}} = \eta_{th} \left(\frac{U_W}{W}\right). \tag{6.18}$$

Chapter 7

Conclusions and Future Research

7.1 Conclusions

Concerns with global warming, air quality, and depletion of oil continue to be a central focus for developing high efficiency, low polluting automobiles and driving current engine research. This dissertation specifically investigated two advanced engine, alternative fuel concepts: a hydrogen-oxygen-argon (H_2-O_2-Ar) internal combustion (IC) engine and a homogenous charge compression ignition (HCCI) engine.

7.1.1 Hydrogen-Oxygen-Argon

In chapter 4, high thermal efficiencies were obtained operating an H_2-O_2-Ar using single and dual spark ignition. However, the expected thermal efficiency of approximately 50% was not achieved due to persistent engine knock at compression ratios higher than 6. Knock also limited the progression of spark timing advance and as a result, limited the peak thermal efficiency. The maximum indicated thermal efficiencies achieved using a single and dual spark ignition were about 45% and 46% respectively, which is reasonable for operation at slow engine speeds. Adding a second spark plug greatly retarded the spark timing when compared to using a single spark plug.

The three-zone model showed that argon as a working fluid increases in-cylinder temperatures, unburned gas temperatures, and laminar flame speed. The results suggested that specific heat ratio affects end gas temperatures more than increasing flame speed. Therefore, using other noble gases, such as helium, will yield similar knocking limitations. This model accurately represented experimental data and can be used for predicting the onset of knock.

7.1.2 Characterizing HCCI Fuels

In chapter 5, previous methods for predicting auto-ignition in IC engines, such as octane number and cetane number, could not be used for accurately predicting auto-ignition in HCCI engines.

The Octane Index, developed by Kalghatgi [Kalghatgi, 2005], accurately predicted auto-ignition for blends containing two components of hydrocarbons, such as PRFs and TRFs, but did not accurately predict auto-ignition of fuels containing ethanol, small amounts of toluene, or gasoline blends. The HCCI Index developed by Shibata and Urushihara [Shibata and Urushihara, 2007; Shibata and Urushihara, 2009] gave similar results to the Octane Index, but had difficulty predicting auto-ignition of fuels containing ethanol and larger amounts of toluene. Experimental results also showed that aromatic additives do not behave similarly and should not be grouped together, as they are in the HCCI Index.

Correlations between auto-ignition and different variables were investigated by testing twenty-four different fuels in a CFR engine. For a fixed intake temperature, CA50 was found to vary linearly with compression ratio, partially resembling calibration curves used in octane tests. The ratio of CA50 to compression ratio, or the slope of the line, shows the sensitivity of auto-ignition to compression ratio for any given fuel. Trends between LTHR and HTHR were also identified. The ratio of LTHR to HTHR varied linearly with compression ratio and the delay between LTHR and HTHR grouped reference fuels and gasoline based fuels together when plotted against CA50. COV IMEP showed no identifiable trend with CA50.

Decreasing intake temperature, while keeping intake pressure and equivalence ratio constant, increased the amount of LTHR and decreased the delay between LTHR and HTHR. A single-zone WMR model verified the trend and showed that varying intake temperature affects LTHR and CA50 while varying intake pressure affects LTHR and the delay between LTHR and HTHR.

Results using a single-zone WMR model was compared with experimental results. Three different mechanisms were used to predict auto-ignition. The mechanisms had difficulty predicting blends containing toluene and ethanol. A sensitivity analysis, using toluene and n-heptane blends, was conducted. The mechanism had difficulty predicting auto-ignition of blends with less than 10% toluene and showed increasing the amount of toluene linearly by volume did not result in a linear increase in compression ratio.

7.2 Future Research

This dissertation explored two advanced engine, alternative fuel concepts for improving efficiency and reducing emissions in IC engines. Although several other engine concepts are available for improving efficiency and reducing emissions, the H_2-O_2-Ar engine and the HCCI engine offer minimal design changes to existing engine technology. Suggestions for further advancing this research are provided in the next sections.

7.2.1 Hydrogen-Oxygen-Argon

Possible solutions for extending the knock limitation are delaying second spark plug [Migita *et al.*, 2007], using advanced ignition systems, such as a plasma spark plug, to increase the combustion rate [Ikeda *et al.*, 2007a; Ikeda *et al.*, 2007b; Kaneko *et al.*, 2008], or cooling the top of the cylinder head to increase heat transfer between the unburned mixture and the cylinder walls. A Diesel H_2-O_2-Ar engine is also a promising route to achieve higher efficiencies if the gaseous fuel injectors can be created to accommodate high injector pressures.

Improvements can be made to the model by adding heat transfer rates near the boundary layer close to the wall. This could help further explain knock limitations in the H_2-O_2-Ar engine. When operating hydrogen-air, knock did not limit spark advance. One possible explanation is hydrogen-air was operated at a higher compression ratio, pushing a larger portion of the mixture near the wall and increasing the amount of heat transfer between the wall and the mixture [Smith, 1994].

7.2.2 Characterizing HCCI Fuels

More fuel blends containing linear amounts of toluene, ethanol, and various aromatics, by volume, should be explored to help identify reference fuels for a standard HCCI number. Also, different test conditions, such higher RPM and lower intake temperatures, should be explored further for the fuels used in this research. Trends established at different operating conditions could be used with trends found in this dissertation to establish a standard HCCI number.

All three mechanisms used in this dissertation accurately predicted trends of isooctane and n-heptane blends, but did not for toluene blends and ethanol blends. Therefore, he mechanism for predicting auto-ignition of toluene blends and ethanol blends should be should be investigated and further developed to better predict experimental results. Also, toluene blends with less than 10% toluene should be specifically investigated.

References

[Aceves *et al.*, 2000] S. M. Aceves, Daniel L. Flowers, C. K. Westbrook, J. R. Smith, W. J. Pitz, R. W. Dibble, M. Christensen, and B. Johansson. A multi-zone model for prediction of HCCI combustion and emissions. *SAE Technical Paper 2000-01-0327*, 2000.

[Al-Baghadadi, 2006] Maher A. R. Sadiq Al-Baghadadi. A simulation model for a single cylinder four-stroke spark ignition engine fueled with alternative fuels. *Turkish J. Eng. Env. Sci.*, 30:331–350, 2006.

[Anderson *et al.*, 2010] J. E. Anderson, U. Kramer, S. A. Mueller, and T. J. Wallington. Octane numbers of ethanol and methanol gasoline blends estimated from molar concentrations. *Energy and Fuels*, 24(12):6576–6585, 2010.

[Andrae *et al.*, 2008] J. Andrae, T. Brinck, and G. Kalghatgi. Hcci experiments with toluene reference fuels modeled by a semi-detailed chemical kinetic model. *Combustion and Flame*, 155(4):696–712, 2008.

[ASTM D2700-11, 2011] ASTM D2700-11. Standard test method for motor octane number of spark-ignition engine fuel. ASTM International West Conshohocken, PA, DOI:10.1520/D2700-11, www.astm.org, 2011.

[ASTM D6890-11, 2011] ASTM D6890-11. Standard test method for determination of ignition delay and derived cetane number (DCN) of diesel fuel oils by combustion in a constant volume chamber. ASTM International West Conshohocken, PA, DOI: 10.1520/D6890-11, www.astm.org, 2011.

[ASTM Standard D2699-11, 2011] ASTM Standard D2699-11. Standard test method for research octane number of spark-ignition engine fuel. ASTM International West Conshohocken, PA, DOI:10.1520/D2699-11 , www.astm.org, 2011.

[ASTM Standard D613-10a, 2010] ASTM Standard D613-10a. Standard test method for cetane number of diesel fuel oil. ASTM International West Conshohocken, PA, DOI: 10.1520/D0613-10A , www.astm.org, 2010.

[ASTM Standard D909-07, 2007] ASTM Standard D909-07. Standard test method supercharge rating of spark-ignition aviation gasoline. ASTM International West Conshohocken, PA, DOI:10.1520/D0909-07, www.astm.org, 2007.

[Au *et al.*, 2001] Michael Y. Au, James W. Girard, Robert W. Dibble, Daniel Flowers, Salvador M. Aceves, Joel Martinez-Frias, Ray Smith, Christian Seibel, and Ulrich Mass. 1.9-liter four cylinder HCCI engine operation with exhaust gas recirculation. *SAE Technical Paper 2001-01-1894*, 2001.

[Bogin, 2008] Gregory Eric Bogin. *Characterization of Ion Production Using Gasoline, Ethanol, and N-Heptane in a Homogeneous Charge Compression Ignition (HCCI) Engine.* PhD thesis, University of California, Berkeley, 2008.

[Chen *et al.*, 2003a] J.-Y. Chen, R. W. Dibble, J. Kolbu, and R. Homma. Optimization of homogeneous charge compression ignition with genetic algorithms. *Combustion Science and Technology*, 175:373–392, 2003.

[Chen *et al.*, 2003b] K. Chen, G.A. Karim, and H.C. Watson. Experimental and analytical examination of the development of inhomogeneities and autoignition during rapid compression of hydrogen-oxygen-argon mixtures. *ASME J. Eng. for Gas Turbines and Power*, 125:458–465, 2003.

[Chen, 2006] Yi-Hann Chen. *Integration, Improvement, and Validationof the ACID Model in KIVA3V CFD Simulation for Predicting SOC in HCCI Engines.* PhD thesis, University of California, Berkeley, 2006.

[Chin and Chen, 2011] Greg Chin and J.-Y. Chen. Modeling of emissions from hcci engines using a consistent 3-zone model with applications to validation of reduced chemistry. *Proceedings of the Combustion Institute*, 33(2):3073–3079, 2011.

[Christensen *et al.*, 1997] Magnus Christensen, Bengt Johansson, and PAtrick Einewall. Homogeneous charge compression ignition (HCCI) using isooctane, ethanol and natural gas - a comparison with spark-ignition operation. *SAE Technical Paper 972874*, 1997.

[Christensen *et al.*, 1999] M. Christensen, A. Hultqvist, and B. Johansson. Demonstrating the multi fuel capability of a homogeneous charge compression ignition engine with variable compression ratio. *SAE Technical Paper 1999-01-3679*, 1999.

[Coleman and Steele, 2009] Hugh W. Coleman and W. Glenn Steele. *Experimentation, Validation, and Uncertainty Analysis for Engineers.* A John Wiley and Sons, INC., third edition, 2009.

[Das, 1991] L.M. Das. Safety aspects of a hydrogen-fuelled engine system development. *Int. J. Hydrogen Energy*, 16(9):619–624, 1991.

[deBoer and Hulet, 1980] P.C.T. deBoer and J.F. Hulet. Performance of a hydrogen-oxygen-noble gas engine. *Int. J. Hydrogen Energy*, 5:439–452, 1980.

[Dec, 2009] John E. Dec. Advanced compression-ignition engines: Understanding the in-cylinder processes. *Proceedings of the Combustion Institute*, 32(2):2727–2742, 2009.

[EERE, 2001] EERE. *Module 3: Hydrogen use in internal combustion engines.* College of the Desert, December 2001.

[Eng *et al.*, 2003] J. Eng, W. Leppard, and T. Sloane. The effect of di-tertiary butyl peroxide (DTBP) addition to gasoline on HCCI combustion. *SAE Technical Paper 2003-01-3170*, 2003.

[Eng, 2002] J.A. Eng. Characterization of pressure waves in hcci combustion. *SAE Technical Paper 2002-01-2859*, 2002.

[Epping *et al.*, 2002] K. Epping, S. Aceves, R. Bechtold, and J. Dec. The potential of HCCI combustion for high efficiency and low emissions. *SAE Technical Paper 2002-01-1923*, 2002.

[Erlandsson, 2002] Olof Erlandsson. Early swedish hot-bulb engines - efficiency and performance compared to contemporary gasoline and diesel engines. *SAE Technical Paper 2002-01-0115*, 2002.

[Erren, 1939] Rudolf Arnold Erren. Internal combustion engine using hydrogen as fuel. United States Patent No. 2,183,674, December 1939.

[Flowers *et al.*, 2000] Daniel Flowers, Salvador Aceves, Ray Smith, John Torres, James Girard, and Robert Dibble. HCCI in a CFR engine: Experiments and detailed kinetic modeling. *SAE Technical Paper 2000-01-0328*, 2000.

[Flowers *et al.*, 2001a] D. Flowers, S. Aceves, C. K. Westbrook, J. R. Smith, and R. Dibble. Detailed chemical kinetic simulation of natural gas HCCI combustion: Gas composition effects and investigation of control strategies. *Journal of Engineering for Gas Turbines and Power-Transactions of the ASME*, 123:433–439, 2001.

[Flowers *et al.*, 2001b] D. Flowers, S. M. Aceves, J. Martinez-Frias, J. R. Smith, M. Y. Au, J. W. Girard, and R. W. Dibble. Operation of a four-cylinder 1.9L propane-fueled homogeneous charge compression ignition engine: Basic operating characteristics and cylinder-to-cylinder effects. *SAE Technical Paper 2001-01-1895*, 2001.

[García *et al.*, 2009] Miguel Torres García, Francisco José Jiménez-Espadafor Aguilar, Tomás Sánchez Lencero, and José Antonio Becerra Villanueva. A new heat release rate (hrr) law for homogeneous charge compression ignition (hcci) combustion mode. *Applied Thermal Engineering*, 20(17-18):3654–3662, 2009.

[Gray and Ryan, 1997] Allen W. (Bill) Gray and Thomas W. Ryan. Homogeneous charge compression ignition (HCCI) of diesel fuel. *SAE Technical Paper 971676*, 1997.

[Guarnieri, 2011] Massimo Guarnieri. When cars went electric, Part 1. *IEEE Industrial Electronics Magazine*, pages 61–62, 2011.

[Gupta, 2006] H. N. Gupta. *Fundamentals of Internal Combustion Engines*. Pretice-Hall of India Private Limited, New Delhi, 2006.

[Hable, 2009] Wolfgang Hable. Combustion performance of mixed alcohol fuels in a CFR engine. Master's thesis, Vienna University of Technology, Austria, 2009.

[Heywood, 1988] John B. Heywood. *Internal Combustion Engine Fundamentals*. McGraw-Hill, Inc., 1988.

[Hiltner *et al.*, 2000] J. Hiltner, R. Agama, F. Mauss, B. Johansson, and M. Christensen. HCCI operation with natural gas: Fuel composition implications. *Proceedings of the 2000 ASME International Combustion Engine Fall Technical Conference*, 35(2):11–19, 2000.

[Horiba, 1990] Horiba. *Instruction Manual for Flame Ionization and Magneto-Pneumatic Analyzer: FMA-220, FIA-220/MPA/220*. Horiba Instruments Inc., 17671 Armstrong, Irvine Industrial Complex, Irvine, CA 92714, Horiba Manual No. 091217 edition, October 1990.

[Horiba, 1991] Horiba. *Instruction Manual for AIA-210/220, Infrared Analyzer*. Horiba Instruments Inc., 17671 Armstrong, Irvine Industrial Complex, Irvine, CA 92714, Horiba Manual No. 091215 edition, December 1991.

[Horiba, 1995] Horiba. *Instruction Manual for CLA-220, Chemiluminescent Analyzer*. Horiba Instruments Inc., 17671 Armstrong, Irvine Industrial Complex, Irvine, CA 92714, Horiba Manual No. 091216 edition, 1995.

[Huang *et al.*, 2010] Chen Huang, Valeri Golovitchev, and Andrei Lipatnikov. Chemical model of gasoline-ethanol blends for internal combustion engine applications. *SAE Technical Paper 2010-01-0543*, 2010.

[Ikeda *et al.*, 2007a] Yuji Ikeda, Masashi Kaneko, Yoshihiro Wachi, and Atsushi Nishiyama. Research and development of microwave plasma combustion engine (First report: Concept and plasma combustion characteristics). *JSAE Technical Paper 20075968*, 2007.

[Ikeda *et al.*, 2007b] Yuji Ikeda, Atsushi Nishiyama, Hiroki Katano, Masashi Kaneko, and Haeyoung Jeong. Research and development of microwave plasma combustion engine (Second report: Engine performance of plasma combustion engine). *JSAE Technical Paper 20075969*, 2007.

[Ikegami *et al.*, 1982] M. Ikegami, K. Miwa, and M. Shioji. A study of hydrogen fuelled compression ignition engines. *Int. J. Hydrogen Energy*, 7(4):341–353, 1982.

[Jensen and Schramm, 2000] T. Jensen and J. Schramm. A three-zone heat release model for combustion analysis in a natural gas SI engine – effects of crevices and cyclic variation on UHC emissions. *SAE Technical Paper 200-01-2802*, 2000.

[Kalghatgi and Head, 2006] G. T. Kalghatgi and R. A. Head. Combustion limits and efficiency in a homogeneous charge compression ignition engin. *International Journal of Engine Research*, 7, 2006.

[Kalghatgi, 2005] G. T. Kalghatgi. Auto-ignition quality of practical fuels and implications for fuel requirements of future SI and HCCI engines. *SAE Technical Paper 2005-01-0239*, 2005.

[Kaneko *et al.*, 2008] Masashi Kaneko, Atsushi Nishiyama, Haeyoung Jeong, Hiroki Katano, and Yuji Ikeda. Combustion characteristics of microwave plasma combustion engine. *JSAE Technical Paper 20085367*, 2008.

[Killingsworth, 2007] Nicholas J. Killingsworth. *HCCI Engine Control and Optimization.* PhD thesis, University of California, San Diego, 2007.

[Knop *et al.*, 2008] Vincent Knop, Adlene Benkenida, Stephane Jay, and Olivier Colin. Modeling of combustion and nitrogen oxide formation in hydrogen-fuelled internal combustion engines within a 3D CFD code. *International Journal of Hydrogen Energy*, 33(19):5083–5097, 2008.

[Kondo *et al.*, 1997] Takashi Kondo, Shuuichi Iio, and Masura Hiruma. A study on the mechanism of backfire in external mixture formation hydrogen engines -about backfire occurred by cause of the spark plug. 971704, SAE Technical Paper, 1997.

[Kuroki *et al.*, 2010] Rentaro Kuroki, Akira Kato, Eiichi Kamiyama, and Daisaku Sawada. Study of high efficiency zero-emission argon circulated hydrogen engine. Technical Report 2010-01-0581, SAE Technical Paper, 2010.

[Lancaster *et al.*, 1975] David R. Lancaster, Roger B. Krieger, and John H. Lienesch. Measurement and analysis of engine pressure data. *SAE Technical Paper 750026*, 1975.

[Laumann *et al.*, 1978] Eugene A. Laumann, James C. Fletcher, and Rollin K. Reynolds. Hydrogen fueled engine. United States Patent No. 4,112,875, 1978.

[Leppard, 1990] W. R. Leppard. The chemical origin of fuel octane sensitivity. *SAE Technical Paper 902137*, 1990.

[Liu *et al.*, 2008] Haifeng Liu, Mingfa Yao, Bo Zhang, and Zunqing Zheng. Effects of inlet pressure and octane numbers on combustion and emissions of a homogeneous charge compression ignition (HCCI) engine. *Energy and Fuels*, 22:2207–2215, 2008.

[Liu *et al.*, 2009] Haifeng Liu, Mingfa Yao, Bo Zhang, and Zunqing Zheng. Influence of fuel and operating conditions on combustion characteristics of a homogeneous charge compression ignition engine. *Energy and Fuels*, 23:1422–1430, 2009.

[Mack, 2007] John Hunter Mack. *Investigation of Homogeneous Charge Compression Ignition (HCCI) engines fuelled with ethanol blends using experiments and numerical simulations.* PhD thesis, University of California, Berkeley, 2007.

[Mehl *et al.*, 2011] Marco Mehl, William J. Pitz, Charles K. Westbrook, and Henry J. Curran. Kinetic modeling of gasoline surrogate components and mixtures under engine conditions. *Proceedings of the Combustion Institute*, 33:193–200, 2011.

[Migita *et al.*, 2007] Hideo Migita, Tohru Amemiya, Kentaro Yokoo, and Yoshiaki Iizuka. The new 1.3-liter 2-plug engine for the 2002 Honda Fit. *JSAE Review*, (23):507–511, 2007.

[Mitani *et al.*, 2008] S. Mitani, D. Sawada, T. Kosuda, and O. Fujishiro. Study of rising thermal efficiency using an argon circulated hydrogen engine. *Transactions of Society of Automotive Engineers of Japan*, 39(2):195–199, 2008.

[Morgan *et al.*, 2010] Neal Morgan, Andrew Smallbone, Amit Bhave, Markus Kraft, Roger Cracknell, and Gautam Kalghatgi. Mapping surrogate gasoline compositions into ron/mon space. *Combustion and Flame*, 157(6):1122–1131, 2010.

[Najt and Foster, 1983] Paul M. Najt and David E. Foster. Compression-ignited homogeneous charge combustion. Technical Report 830264, SAE Technical Paper, 1983.

[Natkin *et al.*, 2002] Robert J. Natkin, Xiaoguo Tang, Kathleen M. Whipple, and Daniel F. Stockhausen. Ford hydrogen engine laboratory testing facility. Technical Report 2002-01-0241, SAE Technical Paper, 2002.

[Noguchi *et al.*, 1979] M. Noguchi, Y. Tanaka, T. Tanaka, and Y. Takeuchi. A study on gasoline engine combustion by observation of intermediate reactive products during combustion. Technical Report 790840, SAE Technical Paper, 1979.

[Oakley *et al.*, 2001] A. Oakley, H. Zhao, T. Ma, and N. Ladommatos. Dilution effects on the controlled auto-ignition (CAI) combustion of hydrocarbon and alcohol fuels. *SAE Technical Paper 2001-01-3606*, 2001.

[Olsson *et al.*, 2002] Jan-Ola Olsson, Per Tunestål, Bengt Johansson, Scott Fiveland, Rey Agama, Martin Willi, and Dennis Assanis. Compression ratio influence on maximum load of a natural gas fueled HCCI engine. *SAE Technical Paper 2002-01-0111*, 2002.

[Onishi *et al.*, 1979] Shigeru Onishi, Souk Hong Jo, Katsuji Shoda, Pan Do Jo, and Satoshi Kato. Active thermo-atmosphere combustion (ATAC) - a new combustion process for internal combustion engines. Technical Report 790501, SAE Technical Paper, 1979.

[Ryan and Callahan, 1996] Thomas W. Ryan and Timothy J. Callahan. Homogeneous charge compression ignition of diesel fuel. 961160, SAE Technical Paper, 1996.

[Shibata and Urushihara, 2007] Gen Shibata and Tomonori Urushihara. Auto-ignition characteristics of hydrocarbons and development of HCCI fuel index. *SAE Technical Paper 2007-01-0220*, 2007.

[Shibata and Urushihara, 2009] Gen Shibata and Tomonori Urushihara. Realization of duel phase high temperature heat release combustion of base gasoline blends from oil refineries and a study of HCCI combustion processes. *SAE Technical Paper 2009-01-0298*, 2009.

[Shibata *et al.*, 2005] Gen Shibata, K. Oyama, Tomonori Urushihara, and T. Nakano. Correlation of low temperature heat release with fuel composition and HCCI engine combustion. *SAE Technical Paper 2005-01-0138*, 2005.

[Shudo and Ono, 2002] T. Shudo and Y. Ono. HCCI combustion of hydrogen, carbon monoxide and dimethyl ether. *SAE Technical Paper 2002-01-0112*, 2002.

[Silke *et al.*, 2008] Emma J. Silke, William J. Pitz, Charles K. Westbrook, Magnus Sjöberg, and John E. Dec. Understanding the chemical effects of increased boost pressure under hcci conditions. *SAE Technical Paper 2008-01-0019*, 2008.

[Smith, 1994] J. R. Smith. Optimized hydrogen piston engines. In *Proceedings of the 1994 International Congress on Transportation Electronics, Convergence 1994*, pages 161–166. SAE, 1994.

[Souder, 2004] Jason S. Souder. *Closed-Loop Control of a Multi-Cylinder HCCI Engine.* PhD thesis, University of California, Berkeley, 2004.

[Spindt, 1965] R. S. Spindt. Air-fuel ratios from exhaust gas analysis. *SAE Technical Paper 650507*, 1965.

[Stanglmaier *et al.*, 2001] Rudolf H. Stanglmaier, Thomas W. Ryan, and Jason S. Souder. HCCI operation of a dual-fuel natural gas engine for improved fuel efficiency and ultra-low NOx emissions at low to moderate engine loads. *SAE Technical Paper 2001-01-1897*, 2001.

[Stone, 1999] Richard Stone. *Introduction to internal combustion engines.* Society of Automotive Engineers, Inc., Warrendale, PA, third edition, 1999.

[Tang *et al.*, 2002] Xiaoguo Tang, Daniel M. Kabat, Robert J. Natkin, and William F. Stockhausen. Ford P2000 hydrogen engine dynamometer development. Technical Report 2002-01-0242, SAE Technical Paper, 2002.

[Taylor, 1997] John R. Taylor. *An Introduction to Error Analysis: The Study of Uncertainties in Physical Measurements.* University Science Books Sausalito, California, second edition, 1997.

[Thring, 1989] R. H. Thring. Homogeneous-charge compression ignition (HCCI) engines. Technical Report 892068, SAE Technical Paper, 1989.

[Tschann, 2009] Phillipp Tschann. Emission and performance studies of alternative fuels. Master's thesis, Graz University of Technology, Austria, 2009.

[Tunestal, 2009] Per Tunestal. Model based tdc offest estimation from motored cylinder pressure data. In *2009 IFAC Workshop on Engine and Powertrain Control, Simulation 2009 IFAC Workshop on Engine and Powertrain Control, Simulation and Modeling*, 2009.

[Tury *et al.*, 1991] Edward L. Tury, Keith Kaste, Ross E. Johnson, and David O. Danielson. Non-dispersive infrared gas analyzer system. United States Patent No. 5,060,505, October 1991.

[Verhelst and Sierens, 2007] S. Verhelst and R. Sierens. Combustion studies for pfi hydrogen ic engines. Technical Report 2007-01-3610, SAE Technical Paper, 2007.

[Verhelst and Wallner, 2009] Sabastian Verhelst and Thomas Wallner. Hydrogen-fueled internal combustion engines. *Progress in Energy and Combustion Science*, 35(6):490–527, 2009.

[Verhelst *et al.*, 2007] Sabastian Verhelst, Stefaan Verstraeten, and Roger Sierens. A comprehensive overview of hydrogen engine design features. *Proceedings of the Institution of Mechanical Engineers, Part D: Journal of Automotive Engineering*, 221:911–920, 2007.

[Warnatz *et al.*, 2006] Jurgen Warnatz, Ulrich Mass, and Robert W. Dibble. *Combustion: Physical and Chemical Fundamentals, Modeling and Simulation, Experiments, Pollutant Formation.* Springer, 4th edition, 2006.

[Welch *et al.*, 2008] Alan Welch, David Mumford, Sandeep Munshi, James Holbery, Brad Boyer, Matthew Younkins, and Howard Jung. Challenges in developing hydrogen direct injection technology for internal combustion engines. Technical Report 2008-01-2379, SAE Technical Paper, 2008.

[Westbrook *et al.*, 1991] C. K. Westbrook, W. Pitz, and W. R. Leppard. The autoignition chemistry of paraffinic fuels and pro-knock and anti-knock additives: a detailed chemical kinetic study. *SAE Technical Paper 912314*, 1991.

[White *et al.*, 2006] C.M. White, R.R. Steeper, and A.E. Lutz. The hydrogen-fueled internal combustion engine: a technical review. *Int. J. Hydrogen Energy*, 31(10):1292–1305, 2006.

[White, 2003] White. Lambda calculation: The Brettschneider Equation, general principles and methods, and its use with alternate fuels. Rev. 021007A 9, Bridge Analyzers, inc., 1805-B Clement Ave, Bldg. 28 Alameda, CA 94501, USA, 2003.

[Woschni, 1967] G. Woschni. A universally applicable equation for instantaneous heat transfer in the internal combustion engine. Technical Report 670931, SAE Technical Paper, 1967.

[Yao *et al.*, 2009] Mingfa Yao, Shaolei Zheng, and Haifeng Liu. Progress and recent trends in homogenous charge compression ignition (HCCI) engines. *Progress in Energy and Combustion Science*, 35:398–437, 2009.

[Zhang *et al.*, 2009] Yan Zhang, Hui Xie, and Hua Zhao. Investigation of SI-HCCI hybrid combustion and control strategies for combustion mode switching in a four-stroke gasoline engine. *Combustion Science and Technology*, 181(5):782–299, 2009.

[Zhao *et al.*, 2003] Fuquan Zhao, Thomas N. Asmus, Dennis N. Assanis, John E. Dec, James A. Eng, and Paul M. Najt. *Homogeneous Charge Compression Ignition (HCCI) Engines Key: Research and Development Issues*. SAE International, 2003.

[Zhao, 2007] H. Zhao. *HCCI and CAI Engines for the Automotive Industry*. Woodhead Publishing Ltd, 2007.

[Zhu and Schock, 2010] Guoming Zhu and Harold Schock. Flex fuel optimized SI and HCCI engine. Presented at the ACE021: 2010 DOE Merit Review, June 2010.

Appendices

Appendix A

Nomenclature

A_f	Flame Surface Area
AFR	Air-Fuel Ratio
ATAC	Active Thermo-Atmosphere Combustion
ATDC	After Top Dead Center
B	Bore Diameter
BDC	Bottom Dead Center
BTDC	Before Top Dead Center
C_{factor}	Number of Carbon Atoms in each Hydrocarbon Molecule Being Measured
C_d	Discharge Coefficient
CA50	Crank Angle Degree when 50% of the Heat is Released
CAD	Crank Angle Degree
CFR	Cooperative Fuel Research
CIHC	Compression Ignition Homogenous Charge
CN	Cetane Number
CO	Carbon Monoxide
CO_2	Carbon Dioxide
COV	Coefficient of Variance
CR	Compression Ratio
DCN	Derived Cetane Number
DICI	Direct Injection Compression Ignition
ECU	Engine Control Unit
EGR	Exhaust Gas Recirculation
F_c	Mass Fraction of Carbon
F_h	Mass Fraction of Hydrogen
F_o	Mass Fraction of Oxygen
H_2O	Water
H_2-O_2-Ar	Hydrogen-Oxygen-Argon
H_CV	Atomic Ratio of Hydrogen to Carbon in a Fuel
HC	Unburned Hydrocarbon
HCCI	Homogenous Charge Compression Ignition
HCSI	Homogenous Charge Spark Ignition
HTHR	High Temperature Heat Release
IC	Internal Combustion
IMEP	Indicated Mean Effective Pressure
K	Kalghatgi Constant for Octane Index
L	Stroke
LHV	Lower Heating Value
LTHR	Low Temperature Heat Release
M_{air}	Molecular Mass of Air
M_f	Molecular Mass of Fuel
MON	Motor Octane Number
NO_x	Nitrogen Oxides
O_{CV}	Atomic Ratio of Oxygen to Carbon in a Fuel

OI	Kalghatgi's Octane Index
ON	Octane Number
P_i	Indicated Power
PRF	Primary Reference Fuel
Q	Heat Released
$Q_{50\%}$	50% of total Heat Released
RON	Research Octane Number
RPM	Revolutions per Minute
S_L	Laminar Flame Speed
S_T	Turbulent Flame Speed
SI	Spark Ignited
T	Temperature
TDC	Top Dead Center
THC	Unburned Hydrocarbon
TRF	Toluene Reference Fuel
TS	Toyota–Soken
U_r	Uncertainty in a Function, r
V	Volume
V_c	Clearance Volume (in^3 or cm^3)
V_d	Displaced Volume (in^3 or cm^3)
W_i	Indicated Work
WMR	Well Mixed Reactor
Y	Mass Fraction of a Species
a	Crank Radius
f	Turbulent Enhancement Factor
h_c	Heat Transfer Coefficient
l	Connecting Rod Length
m_{fuel}	Mass of Fuel
m_{ox}	Mass of Oxidizer
m_b	Mass of burned mixture
n_C	Number of Carbon Atoms
n_H	Number of Hydrogen Atoms
n_R	Number of Crank Revolutions for Each Power Stroke per Cylinder
p	Pressure
st	Stoichiometric
γ	Specific Heat Ratio (C_p/C_v)
η_{comb}	Combustion Efficiency
$\eta_{th,i}$	Indicated Thermal Efficiency
η_{th}	Thermal Efficiency
θ	Crank Angle (degrees)
λ	Normalized Air-Fuel Ratio
ϕ	Equivalence Ratio

ρ_u	Density of Unburned Mixture
ρ	Mixture Density
σ	Standard Deviation
ω	Source Term of a Reaction

Appendix B

Detailed Engine Specifications

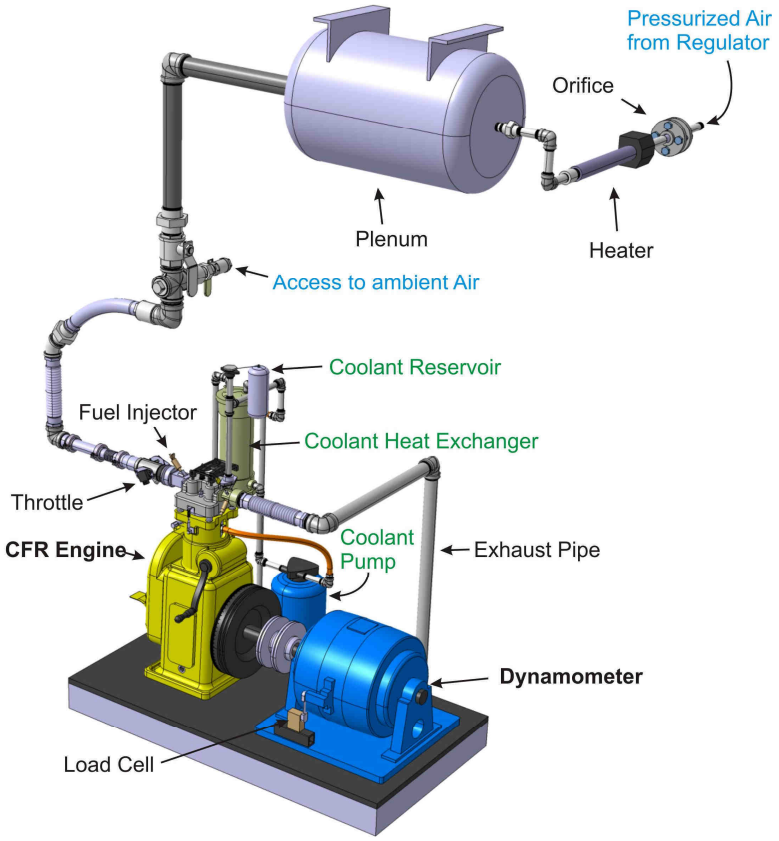

Figure B.1: Schematic of the CFR engine setup at UC Berkeley created by Wolfgang Hable [Hable, 2009].

The following information was taken from Wolfgang Hable's Masters thesis [Hable, 2009] and Philipp Tschann's Masters thesis [Tschann, 2009].

Intake Air System for HCCI operation

A schematic of the CFR's intake air system is shown in figure B.1 [Hable, 2009]. This intake air setup allows the engine to operate naturally aspirated or at set intake pressures using the house air compressor. For HCCI operation, the house air compressor supplied air to the engine to maintain a constant intake pressure. The house air is dehumidified and filtered. An electrical heater was used to control intake temperature (maximum air temperature 150°C) and a pressure regulator controlled intake pressure. A plenum was used to maintain a constant intake pressure and reduce pressure fluctuations. All experiments were conducted un-throttled.

Cooling System

A new cooling system was designed for the CFR engine to prevent overheating and piston seizures. The cooling system cools the engine using coolant, which is constantly pumped through the cylinder coolant jacket and the heat exchanger. The coolant temperature is cooled using cold building water supplied to the heat exchanger. A PID controller regulates an electronic valve to control the flow of cold building water to the heat exchanger. The coolant temperature is measured before and after it travels through the engine. If the coolant temperature exceeds a set temperature, the building water valve is opened, using the PID controller, to cool the coolant. Once the coolant temperature drops below the set temperature, the building water valve is closed. The maximum temperature rating of the coolant pump is 80°C. For safety, a manual ball valve can be opened to bypass the electronic valve. A visual paddle flow meter is used to ensure coolant is flowing through the engine.

Fuel System

A new liquid-fuel system was added to the CFR engine to allow for easy transition between testing multiple fuels and minimize contamination between fuels. The new liquid-fuel system consists of three, 1-gallon pressured fuel tanks. After fuel is added to each tank, the fuel tanks are pressurized to 40 psi using nitrogen supplied by a compressed nitrogen gas-cylinder. The pressure from the nitrogen drives fuel from the tank, through fuel filters, and to the injector. A three-way valve allows the user to select one of the three fuel tanks and easily change between fuel tanks during operation. A two-way valve, closer to the injector, allows the user to change between the new liquid-fuel system and the old liquid-fuel system. The new fuel system is separate from the gaseous fuel system on the CFR. A different injector is used to supply gaseous fuels and the regulator on the compressed gas cylinder controls the injector pressure.

Appendix C

Intake Air Orifice Specifications

71 Deer Park Ave.
"Babylon, NY 11702"
631.587.1000 FAX 631.587.1011
www.lambdasquare.com

3/4" ORIFICE
5300
5300 - 0.25 - 0.250

ORIFICE2 (Ver 1.52) FLOW ELEMENT CALCULATION

Tag.....: UC BERKLEY 0.003 CU MTR/SEC.
Spec No.:
Line No.:
Customer: UC BERKLEY
Project#:
Revision:
CalcType: Differential
Date.....: 07/22/10 12:05
Equipment No..:
Customer PO...:
Shop Order....:
Revised By....:
Fluid State...: Gas
Calculation Equ Ref: Flow Measurement Engr Handbook, 2nd Ed.

Fluid AIR

Element....,	Type	Orifice, Corner Taps	
,	Material	304 SS	
,	Beta Ratio @ 20.0 Deg C	0.3034	d/D
,	Bore @ 20.0 Deg C	0.2500	d, Inch — 0.250
Pipe.....,	Schedule STD and Size	0.7500	Inch
,	Material	Steel	
,	Inside Diameter @ 20.0 Deg C	0.8240	D, Inch
Base.....,	Pressure at Std Cond	14.6960	Pb, PSI Abs
,	Temperature at Std Cond	15.0000	Tb, Deg C
Local.....,	Atmospheric Pressure	14.6960	Pg, PSI Abs
Pressure...,	Flowing at Upstream Tap	0.0000	Pf, PSI Gauge
,	Differential Maximum	2.3556	Hm, PSI — D/P
,	Differential Normal	1.1542	Hn, PSI
,	Permanent Loss @ Max Flow	2.0608	Lm, PSI
,	Permanent Loss @ Norm Flow	1.0098	Ln, PSI
Temperature,	Flowing	25.0000	Tf, Deg C
Flow.....,	Maximum, Base Conditions	0.0030	Qm, M3/Sec — Flow
,	Normal, Base Conditions	0.0021	Qn, M3/Sec
,	Reynolds Nmbr @ Norm Flow	8,489.1546	RDn
,	Reynolds Nmbr @ Max Flow	12,127.3637	RDm
Fluid Prop.,	Molecular Weight	28.9510	Mol. Wt.
,	Density @ Base Cond. (Est)	1.2264	Rhob, Kg/CM
,	Density @ Flow Cond. (Est)	1.1852	Rhof, Kg/CM
,	Viscosity @ Flowing	0.0185	Centipoise
,	Ratio of Specific Heats	1.4021	Cp/Cv
,	Compress Calc Method	Redlich Kwong	
,	Critical Pressure	547.3724	Pc, Psi abs
,	Critical Temperature	-221.2780	Tc, Deg F
,	Compressibility @ Base	0.9994	Zb
,	Compressibility @ Flowing	0.9995	Zf
Factors....,	Flow Coefficient	0.6037	C
,	Sizing Coefficient	0.0000	Sm
,	Gas Expansion Factor	0.9769	Y1
,	Combined Thermal Expan Factor	1.0002	Fa

This calculation performed in accordance with equation 9.107 U.S. Units or equation 9.121, S.I. units.
Warnings..., Outside recommended pipe id of 2-36 inches (50-900 mm).
, Outside recommended Reynolds No range of 10,000 - 10,000,000.

Appendix D

Five-Gas Horiba Analyzer

A Horiba Gas Analyzer system was used to measure concentrations of unburned hydrocarbons (THC), oxygen (O_2), carbon monoxide (CO), carbon dioxide (CO_2), and oxides of nitrogen (NO_x). THC and O_2 were measured using a Horiba MPAWater vapor is condensed out of the exhaust gases, using an ice bath, before entering the Horiba Gas Analyzer. After condensing the water out of the system, the remaining exhaust gases are heated to 70 °C. The following sections describe how the Horiba Gas Analyzer measures THC, O_2, CO, CO_2, and NO_x.

Unburned Hydrocarbon Emissions Measurements

Unburned Hydrocarbon (THC) concentrations were measured using a Horiba FMA-220 unit with an FIA-220 flame ionization detector (FID). The FIA-220 introduces the exhaust gases to a chamber containing a hydrogen-air flame. When the exhaust gases enter the hydrogen flame, the THC in the sample gas break down into carbon fragments and acquire a positive charge. These charged carbon atoms are detected by two DC charged, electrodes fitted on opposite sides of the hydrogen flame. The number of ions produced is proportional to the number of carbon atoms from the hydrocarbon combusted in the hydrogen flame. The current current in the electrodes is converted to an electric voltage through a resistor to detect the hydrocarbons [Horiba, 1990].

Measurements of hydrocarbon concentration taken using a hydrogen FID is not affected by the presence of inorganic gases such as CO, CO_2, water, NO_x in the sample. However, changes in O_2 concentrations do have an effect. Details can be found in Mack's dissertation [Mack, 2007]. Measurements can also change with flow rate, fuel components, and proportion of fuel components.

The FIA-220 analyzer uses C_3H_8 (in air) as a reference for relative sensitivity to different hydrocarbons. This allows accurate measurements to be made by keeping responses with in ±5% (including ±2% for gas accuracy) for a range of hydrocarbons [Horiba, 1990].

Oxygen Emissions Measurements

Oxygen (O_2) concentrations were measured using a Horiba FMA-220 unit with an MPA-220 magneto-pneumatic oxygen detector, taking advantage of O_2 being a paramagnetic material. O_2 is several hundred times more magnetically susceptible than other gases. The MPA-220 analyzer operates by collecting a sample containing oxygen molecules in a test chamber. Inside the test chamber, the sample containing O_2 is introduced to a non-homogenous magnetic field, generated by an electromagnet. A reference gas, in this case nitrogen (N_2), is introduced into the test chamber through two inlets. One inlet mixes N_2 with the sample gas in the magnetic field. O_2 in the sample and reference gas mixture is attracted to the area of the test chamber with the greatest magnetic field strength. The difference in paramagnetism between O_2 and N_2 creates a differential pressure. The second inlet of N_2 gas is used to balance the differential pressure. The differential pressure is directly proportional to oxygen concentration and measured using a condenser microphone. The

following equation relates differential pressure to oxygen concentration:

$$\Delta P = \frac{1}{2}(H)^2(X)(C), \tag{D.1}$$

where ΔP is the difference in pressure between the paramagnetic gas and the non-magnetic gas, H is the strength of the magnetic field, X is the magnetic susceptibility of the paramagnetic gas (usually known), and C is the concentration of paramagnetic gas [Horiba, 1990].

The MPA-220 provides a precise O_2 measurements because it directly and accurately measures the magnetic susceptibility. However, the MPA-220 O_2 measurements are limited to measurements in percent O_2 and is not recommended for trace oxygen measurements. Although the the MPA-220 O_2 measurements are not influenced by thermal properties of other gases present in the sample, it is sensitive to vibrations.

Carbon Monoxide and Carbon Dioxide Emissions Measurements

The Horiba AIA-210 and AIA-220 infrared analyzers uses non-dispersive infrared analysis to continuously measure the concentrations of carbon monoxide (CO) and carbon dioxide (CO_2) in a sample gas. Inside the AIA-210 and AIA-220 analyzers, two equal-energy infrared beams are directed through two parallel optical cells, a sample cell and a reference cell. The reference cell contains a continuously flowing reference gas, N_2, while the sample cell contains the sample gas.

The infrared beam going into the sample cell is interrupted by a chopper operating at a frequency specific to CO or CO_2, depending on the analyzer. The infrared beam is also optically filtered to reduce background interference from other infrared-absorbing components. As the interrupted infrared beam passes through the sample gas, some of the infrared radiation is absorbed by CO or CO_2 present in the sample gas. The quantity of infrared radiation that is absorbed is proportional to the concentration of CO or CO_2. The detector compares the intensity of infrared beam through the sample cell and the reference cell to determine the concentration of CO or CO_2. The membrane inside the detector cell vibrates due to the difference in intensity of the two beams and generates an electric output, which is proportional to the concentration of the desired gas [Horiba, 1991; Tury *et al.*, 1991].

The intensity of the infrared beam passing through the sample gas can be determined using the Beer-Lambert Law:

$$\tau = \frac{I}{I_0} = e^{-\alpha l}, \tag{D.2}$$

where τ is transmissivity, I is the intensity of the transmitted light, I_0 is the intensity of the incident light (the source), α is the absorption coefficient of the substance, and l is the distance the light travels through the material (i.e. the path length).

If the sample gas contains components which absorb infrared wavelengths that partially overlap with those absorbed by the components to be measured, a solid state filter can be used to remove the overlapping wavelengths in advance so measurements are not affected [Horiba, 1991].

Oxides of Nitrogen Emissions Measurements

The Horiba CLA-220 is an atmospheric pressure type NO_x analyzer that uses silicon photodiodes near the reaction chamber for sensing the chemiluminescent reaction. The chemiluminescent method of detection of nitric oxide (NO) is based on the reaction of NO with ozone (O_3) to produce nitrogen dioxide (NO_2) and O_2. About 10% of the NO_2 molecules produced initially exist in an electronically excited state (NO_2^*). The excited NO_2^* quickly revert to the non-excited state, emitting photons during the process. The process of NO producing NO_2 is described by the following reactions:

$$\begin{aligned} NO + O_3 &\rightarrow NO_2^* + O_2 \text{ and} \\ NO_2^* &\rightarrow NO_2 + h\nu, \end{aligned}$$

where h is Planck's Constant and ν is the frequency of the photon in hertz. When NO and O_3 mix in the reaction chamber, the chemiluminescent reaction produces light emission that is directly proportional to the concentration of NO. Silicon photodiodes are used to detect and measure the light emitted. The ozone present in the first reaction is produced by high-voltage electric discharge in O_2 [Horiba, 1995].

The NO_x detection is identical to the NO detection except prior to entry into the reaction chamber, the sample is routed through a converter where NO_2 is dissociated to form NO. The following reaction shows the formation of NO from NO_2:

$$NO_2 + C \rightarrow NO + CO.$$

The amount of NO_x is determined by summing the NO originally present in the sample and the NO resulting from the dissociation of NO_2 [Horiba, 1995].

Appendix E

HCCI Emissions Data

Fuel	CR	phi	lambda	THC (ppm C)	O2 (%)	CO (ppm)	CO2 (%)	NOx (ppm)
n-heptane	6.50	0.33	3.02	2110	14.25	1897	4.44	1
	6.60	0.33	3.01	1890	14.28	1494	4.48	0
	6.75	0.34	2.97	1910	14.18	1349	4.54	1
	6.80	0.34	2.96	1780	14.18	1287	4.55	0
	7.02	0.34	2.94	1930	14.13	1245	4.59	1
	7.15	0.34	2.93	1690	14.08	1037	4.59	1
	7.25	0.34	2.93	1650	14.13	1014	4.61	1
PRF 60	9.26	0.32	3.13	2830	14.65	1447	4.34	1
	9.51	0.32	3.11	2920	14.63	1303	4.37	1
	9.75	0.32	3.10	2740	14.65	1166	4.40	1
	10	0.33	3.06	2640	14.58	1048	4.46	1
	10.51	0.33	3.03	2530	14.48	915	4.49	1
PRF 70	10.28	0.32	3.11	4400	14.25	1455	4.32	1
	10.45	0.33	3.04	4480	14.18	1265	4.45	1
	10.57	0.33	3.01	4250	14.13	1218	4.50	1
	10.7	0.34	2.96	3480	14.03	1080	4.57	2
PRF 75	11	0.34	2.97	3117	14.10	1244	4.51	1
	11.25	0.34	2.95	2955	14.10	1037	4.56	1
	11.51	0.34	2.92	2754	14.03	966	4.59	2
	11.74	0.34	2.93	2694	14.05	914	4.58	1
	12	0.34	2.96	2622	14.15	874	4.55	1
PRF 85	12.69	0.32	3.09	5020	14.30	1430	4.38	1
	13.03	0.32	3.12	5680	14.35	1278	4.34	1
	13.23	0.32	3.09	5320	14.30	1213	4.38	2
	13.5	0.33	3.03	4630	14.20	1056	4.48	2
PRF 88	14.6	0.33	3.01	5270	14.18	1267	4.51	2
	14.85	0.33	3.01	4950	14.18	1118	4.52	3
	15.2	0.33	3.03	4870	14.23	1096	4.48	3
S 70	10.26	0.34	2.97	4360	14.10	1240	4.58	1
	10.45	0.33	2.99	4550	14.15	1244	4.56	1
	10.68	0.34	2.90	3710	13.98	1059	4.70	2
	11	0.35	2.86	4130	13.85	927	4.78	3
TRF 70	10.72	0.33	3.06	4790	14.65	1410	4.56	1
	10.96	0.33	2.99	4260	14.53	1193	4.68	1
	11.27	0.33	3.00	4090	14.55	1166	4.65	1
E-PRF 70	11	0.31	3.24	3453	14.68	1788	4.13	0
	11.25	0.32	3.14	2988	14.58	1290	4.30	0
	11.51	0.32	3.12	2994	14.50	1190	4.31	0
	11.74	0.32	3.11	2853	14.55	1141	4.34	0
	12	0.33	3.00	2769	14.33	960	4.52	1

Table E.1: Emissions data for reference fuels.

Fuel	CR	phi	lambda	THC (ppm C)	O2 (%)	CO (ppm)	CO2 (%)	NOx (ppm)
Gas	14.76	0.33	3.06	3520	14.63	1334	4.48	1
	15.02	0.32	3.11	3670	14.88	1306	4.44	1
	15.52	0.33	3.03	3290	14.65	1042	4.55	1
	15.75	0.32	3.11	3150	15.15	1035	4.53	1
GasB1	10.26	0.33	3.06	3970	14.40	1504	4.48	1
	10.51	0.33	3.05	4140	14.38	1341	4.49	1
	10.76	0.33	2.99	3630	14.28	1114	4.58	1
	11	0.34	2.93	3480	14.10	1021	4.67	2
GasB2	16.52	0.32	3.11	4380	15.15	1207	4.53	1
	16.73	0.33	3.04	3890	15.00	1049	4.64	1
	17	0.33	3.03	4020	14.85	1051	4.60	1
GasB3	16	0.33	3.04	3890	15.30	1068	4.72	1
	16.25	0.33	3.04	3870	15.48	1027	4.78	2
	16.52	0.33	2.99	3580	15.15	915	4.79	3
GasB4	16.05	0.32	3.15	6230	14.45	1166	4.60	2
	16.2	0.32	3.08	5390	14.30	1020	4.72	3
	16.41	0.33	3.05	5140	14.23	1002	4.76	4
GasB5	17.19	0.32	3.08	4640	14.50	1180	4.38	1
	17.48	0.33	3.04	4170	14.40	1065	4.45	1
GasB6	15.95	0.31	3.27	4270	14.63	1285	4.41	1
	16.46	0.31	3.23	4130	14.58	1088	4.49	1
	16.68	0.31	3.20	3960	14.55	1053	4.53	2
GasB7	15.95	0.31	3.26	4120	14.63	1245	4.43	1
	16.25	0.31	3.25	3990	14.63	1153	4.46	1
	16.52	0.31	3.24	3900	14.58	1090	4.46	1
	16.73	0.31	3.22	3810	14.55	1039	4.50	2
GasB8	14.76	0.32	3.09	4850	14.60	1314	4.39	1
	15.02	0.33	3.05	4660	14.53	1166	4.47	1
	15.24	0.33	3.03	4490	14.53	1143	4.50	2
	15.52	0.33	3.02	4190	14.50	1052	4.53	3
	15.75	0.33	3.03	4300	14.53	995	4.50	3
GasB9	15.02	0.34	NA	NA	NA	NA	NA	NA
	15.24	0.34	NA	NA	NA	NA	NA	NA
	15.75	0.34	NA	NA	NA	NA	NA	NA
	16.1	0.34	NA	NA	NA	NA	NA	NA
GasB10	16.46	0.30	3.28	4720	14.83	1442	4.46	1
	16.68	0.31	3.26	4460	14.68	1301	4.45	1
	17.25	0.28	3.56	4210	15.18	1397	4.07	1
	17.48	0.31	3.26	4130	14.73	1106	4.46	1

Table E.2: Emissions data for Gas and Gas Blends.

Fuel	CR	phi	lambda	THC (ppm C)	O2 (%)	CO (ppm)	CO2 (%)	NOx (ppm)
Gas2	12.14	0.32	3.17	4330	14.30	1236	4.53	1
	12.31	0.32	3.14	3860	14.28	1172	4.57	1
	12.63	0.31	3.20	4680	14.38	1143	4.49	1
Gas2B1	9.75	0.32	3.11	2690	14.58	1596	4.35	1
	10.00	0.33	3.06	2450	14.50	1287	4.43	1
	10.26	0.33	3.01	2370	14.45	1092	4.53	1
	10.51	0.34	2.96	2390	14.35	1013	4.62	1
	10.76	0.33	3.01	2360	14.45	983	4.54	1
Gas2B2	15.02	0.33	3.07	NA	14.43	NA	4.39	NA
	15.24	0.33	3.07	NA	14.43	NA	4.39	NA
	15.52	0.33	3.05	NA	14.43	NA	4.44	NA
Gas2B3	12.75	0.32	3.09	3520	14.55	1336	4.39	1
	13.3	0.33	3.06	3580	14.50	1090	4.43	2
	13.5	0.33	3.07	3540	14.53	1027	4.42	2

Table E.3: Emissions data for Gas2 and Gas2 Blends.